UC Berkeley
UC Berkeley Electronic Theses and Dissertations

Title

The Formation and Aggregation of Iron Oxyhydroxide Nanoparticles in the Aqueous Environment

Permalink

https://escholarship.org/uc/item/6vt3n71r

Author

Legg, Benjamin Adam

Publication Date

2013

Peer reviewed|Thesis/dissertation

The Formation and Aggregation of Iron Oxyhydroxide Nanoparticles
in the Aqueous Environment

By

Benjamin Adam Legg

A dissertation submitted in partial satisfaction of the

requirements for the degree of

Doctor of Philosophy

in

Materials Science and Engineering

In the

Graduate Division

of the

University of California, Berkeley

Committee in charge:

Professor Jillian F. Banfield

Professor Ramamoorthy Ramesh

Professor Hans-Rudolf Wenk

Fall 2013

Abstract

The Formation and Aggregation of Iron Oxyhydroxide Nanoparticles
in the Aqueous Environment

By

Benjamin Adam Legg

Doctor of Philosophy in Materials Science and Engineering

University of California, Berkeley

Professor Jillian F. Banfield, Chair

Nucleation, growth, and aggregation are interconnected processes which control the formation nanoparticles within aqueous environments and the development of nanoparticle structures. These processes are of fundamental engineering importance for the development of new nanoparticle synthesis methodologies and the creation of hierarchical self-assembled structures. They are also fundamentally important concepts for describing how nanoparticles and minerals are formed and distributed throughout the natural environment. The development of more sophisticated models for nucleation, growth, and aggregation within the aqueous environment has become a pressing scientific need, because nanoparticle size, shape, and aggregate structure are known to impact particle reactivity, bioavailability, transport and fate within the environment. In recent years, it has become apparent that complex interactions may exist between the processes of nucleation, growth, and aggregation, and these interactions are especially important during the formation of nanometer scale particles. For example, aggregation has been shown to serve as a mechanism for the growth of nanocrystals, and as a potential driver for phase transformations. However, the details of these interactions are not fully understood.

In this work, a combination of advanced *in situ* characterization techniques, including cryogenic transmission electron microscopy (cryo-TEM) and small angle x-ray scattering (SAXS), have been combined to better understand the development of nanoscale structures in aqueous systems. These techniques are complementary. Cryo-TEM provides new capabilities for nanoscale imaging of particles *in aqua*. It is especially useful for imaging fragile aggregate structures, which cannot be dried without damage, and for obtaining snapshots of reactive solutions that are evolving over time. Furthermore, cryo-TEM can be used to produce three-dimensional tomographic reconstructions (cryo-ET), providing structural models for particles and nanoparticles. However, TEM methodologies are limited by sampling statistics and are not ideal for determining the kinetics of structural change. SAXS is a complementary method that allows suspension properties such as particle size and aggregate structure to be characterized in a time-resolved fashion. SAXS has the potential to provide more statistically robust measurements, and to provide detailed reaction kinetics. However, SAXS data interpretation requires some level of *a*

priori knowledge of the structure being characterized. Thus, by combining SAXS with cryo-TEM, a structurally accurate and statistically robust description of nanoparticle aggregate structure can be obtained.

This dissertation consists of four studies, which seek explain how iron oxyhydroxide nanoparticles nucleate and develop new structures via aggregation, within the aqueous environment.

The aim of the first study is to determine the structure of ferrihydrite nanoparticle aggregates *in aqua*. This is achieved using complimentary cryo-TEM and SAXS methodologies. Ferrihydrite nanoparticles are known to form complex aggregate structures. Interpretation of SAXS data is difficult due to suspension polydispersity. Cryo-ET is used to obtain three-dimensional images of the nanoparticle suspensions. A variety of aggregate structures are observed, with branched networks of linear chains of particles being prevalent in most suspensions. The tomographic structural models are processed to determine aggregate fractal dimensions, using an autocorrelation function based approach. These results are combined with SAXS data to obtain a more comprehensive understanding of the suspension complexity. The networks of linear chains are shown to possess low fractal dimensions, between 1.0 and 1.4; significantly lower than would be expected from traditional models for aggregation. This has important consequences for the aggregate's physical behavior, and allows very large aggregates to exist in stable colloidal suspension without flocculation.

The second study addresses how the ferrihydrite aggregate structure responds to changes in the ionic strength of the suspension, and how low-dimensional aggregate structures may influence nanoparticle transport through subsurface environments. Introducing ferrihydrite particle aggregates into solutions of 2 mM to 50 mM $NaNO_3$ is shown to induce aggregate collapse, with more salt leading to the formation of denser aggregate structures and eventual flocculation. Complementary experiments show that millimolar quantities of $NaNO_3$ induce a fundamental change in nanoparticle transport through a saturated quartz sand column. In deionized water, where low fractal dimension aggregates are stable, nanoparticles deposit evenly throughout the column, which soon saturates with particles so that subsequent injections are transported freely. When conditions favor aggregate collapse, dense localized accumulations occur and more nanoparticles can be deposited within the column. These deposits may be mechanically unstable, leading to irregular transport behavior.

In the third study, the relationship between aggregation and iron oxyhydroxide phase transformations is explored. Previous researchers have found that akaganeite (β-FeOOH) nanoparticles transform to create hematite (α-Fe$_2$O$_3$) nano-spindles in response to hydrothermal aging, but the mechanism of transformation is unknown. Some researchers have proposed a process based on the aggregation of hematite precursors, while others advocated for dissolution and re-precipitation mechanisms. In this study, the kinetics of the phase transformation from akaganeite to hematite is studied, and cryo-TEM is used to characterize the aggregate structures in the transforming suspension. The hematite spindles are shown to be nanoporous, while akaganeite nanoparticles display a tendency for oriented aggregation. Hematite spindles are frequently found in intimate contact with akaganeite nanoparticle aggregates during the process of phase transformation, suggesting a model for phase transformation in which the dehydration of akaganeite to form hematite is enhanced by aggregation.

In the final study, the nucleation and growth of akaganeite nanoparticles from acidic (pH 1.5-3) $FeCl_3$ solutions is tracked with *in situ* small angle x-ray scattering (SAXS). The hydrothermal precipitation process studied can generate highly monodisperse particles, whose size, shape, and nucleation rate can be tuned by varying solution saturation and temperature.

Classical nucleation modeling is applied to determine new values for the interfacial energy of ferric oxyhydroxide clusters. The interfacial energy (interfacial tension) of the nucleus is shown to be pH dependent and ranges from 0.06 to 0.12 J/m^2 within the range of experimental conditions. The interfacial tension decreases with decreasing pH. At the onset of nucleation, this corresponds to very small critical nuclei, containing just 4 to 30 iron atoms. The free energy of the early critical nuclei (40-70 kJ/mol) is found to be small relative to the effective activation energy for particle growth (140-200 kJ/mol). This suggests a situation where differences in growth kinetics may be as important for determining the first formed phase as differences in precipitate solubility or interfacial energy.

A thermodynamic construction for the free energy of an embryonic cluster is presented that can be extended to clusters of arbitrarily small size, including iron monomers. This construction can be used to define the interfacial tension of dissolved species, and determine this interfacial tension from readily available solubility data. The interfacial tension of the monomer is shown to closely track the experimentally determined interfacial tension of the critical nucleation clusters, suggesting a new method for estimating oxyhydroxide interfacial tensions when direct experimental measurements are unavailable.

In combination, these studies reveal the wide array of structures and behaviors that can occur in aqueous suspensions of ferric oxyhydroxide nanoparticles. *In aqua* methodologies with nanoscale resolution have allowed novel nanoparticle structures to be observed (*e.g.* linear particle chains and nanoporous hematite), and have been used to show the impact of nanoparticle aggregation on a variety of important physical processes (*e.g.* nanoparticle transport and phase transformation). These *in aqua* methods are also powerful tools for quantitative characterization of fundamental processes such as nanoparticle nucleation and growth; allowing important material properties (*i.e.* interfacial energy) that were previously unknown to be obtained. This type of information will allow for the refinement of existing iron oxyhydroxide synthesis approaches, to provide better control over particle size, shape, and phase, and will allow scientists to predict where nanoparticles may form within the environment.

Table of Contents

Acknowledgements

The work included in this dissertation would have been simply impossible without the efforts, assistance, and contributions of many collaborators, colleges, and mentors. I've sought to identify specific contributions at the end of each chapter. However, there are too many to list them all. Here, I would like to recognize some of the most important contributors.

I would like to start by recognizing the many mentors who have helped me through this program. Foremost among these is my research advisor, Jillian Banfield, whose faith in my work has been indispensable. She has trusted my abilities and seen the value in my work at times when I had doubts. Without that support, I would not have completed this dissertation. I must also recognize Benjamin Gilbert, who has been a valued second mentor. Ben has always been gracious with his time, whether I needed help troubleshooting an experiment, refining a paper, solving logistical problems, or just asking for advice. I also want to recognize Glenn Waychunas and Catherine Frandsen as important mentors and collaborators.

Special recognition needs to go to Luis Comolli and Roseaan Csencists, who were both instrumental in the acquisition of the transmission electron microscopy images that form the foundation of this dissertation. I will be forever grateful that they were willing to work with me on these projects. Luis helped obtain the most stunning early cryo-TEM datasets, and he trained me in the art of tomographic reconstructions so that raw images could be transformed into meaningful structural models and beautiful visualizations. Similarly, Roseann did more than provide technical support, she spent the time to patiently teach me the techniques of electron microscopy sample preparation and imaging so that that I could obtain my own images.

I am also grateful for my colleagues, Heng Zhang and Mengquing (Mike) Zhu. They've been there every day as collaborators, office-mates, and friends. I'll fondly remember the afternoons we spent analyzing XRD data or puzzling over thermodynamic models together. Mike has been an especially close collaborator with me on several different projects. We spent many long nights at the beamline together, collecting the SAXS data that underlies several chapters of this dissertation. His enthusiasm for research is infectious, and helped carry my through this work.

Chapter 1: Introduction

The research performed in this dissertation has sought to address two questions of broad technological and environmental importance: "how do nanoparticles form in the environment, and once formed, what is their eventual fate?" Although simple in nature, these questions are not easily resolved. Processes involving nanoparticles may be extremely complex, and may depend upon the composition, shape, size, and aggregate structure of the particles being considered. Nanoparticle formation, for example, cannot generally be described by a single physical process, but may involve complex interactions between processes such as particle nucleation, particle growth, and particle aggregation.

This work focuses the behavior of iron (ferric) oxyhydroxide and oxide nanoparticles within aqueous environments. These phases are of technological interest due to their applications as pigments, magnetic media and biological imaging.[1] Furthermore, they are environmentally prevalent and geochemically active. Environmentally occurring iron oxyhydroxides may serve as important electron acceptors for many microorganisms,[1] and iron oxyhydroxide can also play important roles in controlling the environmental distribution of containments such as arsenic, lead, copper, and radionuclides.[2,3]

Iron oxyhydroxide phases commonly occur as nanoparticles; this is favored due to the low solubility of ferric iron, among other factors. However, the final size and structure of an iron oxyhydroxide mineral is determined by the coupled processes of nucleation, growth, aggregation, and phase transformation. In order to understand the physical behavior of nanoparticles, it is important to characterize their nanostructures and understand how these structures arise. The reactivity of such particles depends on crystalline phase, particle morphology, and aggregation state.[4,5] All three levels of structure must be accounted for in able to fully describe the physical/environmental behavior of iron oxides and oxyhydroxides.

Iron oxyhydroxide systems display many interesting behaviors that are worthy of scientific investigation. For example, ferrihydrite nanoparticles have been shown to aggregate and form stable clusters in suspension.[6] Comprehensive descriptions of these aggregate structures and their physical properties are needed, in order to determine how these aggregate structures impact ferrihydrite reactivity, bioavailability, and environmental distribution. In related systems, the aggregation of iron oxyhydroxide nanoparticles has actually been shown to drive crystal growth, via a process of oriented attachment.[7,8,9] This pathway for crystal growth is conceptually rather new and is a matter of active exploration. Iron oxyhydroxide aggregates can provide a useful tool for exploring the behavior of oriented aggregation, and for considering how oriented aggregation may be coupled with related processes such as phase transformation.

Some of the most fundamentally important and outstanding questions about iron oxyhydroxides relate to the initial process of nanoparticle formation. Basic concepts in particle nucleation and growth are historically well established, and these theories are often assumed to govern the formation of iron oxyhydroxides and other minerals.[10,11,12] However, there have been numerous challenges in actually applying these theories to describe aqueous precipitation for real oxyhydroxide systems. Prior to this work, although extensive research on iron oxyhydroxide precipitation have been conducted, no known studies have been able to directly and quantitatively relate experimentally observed iron oxyhydroxide nucleation rates to fundamental

parameters such as solution supersaturation, interfacial energy, or reaction temperature. As will be shown, these quantitative relationships can be established if the correct experimental data is available. By performing such analysis, new insights into the process of nanoparticle and mineral precipitation are obtained.

In order to investigate the phenomena discussed above, cutting edge characterization techniques have been adapted and refined, so that nanoparticle nucleation, growth, and aggregation can be observed directly within the aqueous environment. Such characterization has been historically difficult. For example, many nanoparticle aggregates are fundamentally fragile objects, with a structure that can depend sensitively upon solution chemistry. Traditional methods for nanoscale imaging are likely to destroy important aggregate features. In order to describe such structures, it is necessary to use *in situ* techniques with nanoscale structural resolution. Cryogenic transmission electron microscopy (cryo-TEM) and small angle x-ray scattering (SAXS) have been combined in new ways to achieve this goal. Together, these techniques provide *in situ* imaging capability to determine nanoparticle structure, and the ability to describe evolving nanoparticle and aggregate structures in a quantitative, time-resolved fashion.

The subsequent chapters in this dissertation each focus on a unique iron oxyhydroxide aqueous system, in which different physical processes have been isolated and studied. Although their content is complimentary, each chapter has been prepared as self-contained manuscript.

Chapter 2 introduces the method of cryo-TEM for imaging nanoparticle aggregates in the aqueous environment, and introduces the use of cryo electron tomography (cryo-ET) to show the three dimensional aggregate structure. Direct imaging with cryo-TEM provides a powerful tool for obtaining a basic conceptual understanding of the aggregate structural motif. This is a significant improvement over historical methods, which required the structure to be inferred. Additionally, methods are developed for extracting fundamental physical parameters such as fractal dimension from tomographic structural models. This approach allows new cryo-ET results to be readily compared with more traditional SAXS based results, so that new tomographic structural models to be put into historical context. This work shows that ferrihydrite nanoparticle aggregates may form extended networks with low fractal dimensions that are not predicted by traditional models for colloidal aggregation.

Chapter 3 explores the physical properties of low-fractal dimension ferrihydrite aggregates in greater detail. The response of aggregate structure to changing aqueous chemistry (especially ionic strength) is explored. At the same time, complimentary studies address how ionic strength influences the environmental transport properties of nanoparticle aggregates. This work shows that increasing the ionic strength of a ferrihydrite nanoparticle suspension may induce aggregate collapse, converting low density aggregate structures into more densely packed structures. Changing the ionic strength also leads to significant changes in the environmental transport behavior, shifting from a steady deposition based process to more stochastic processes, where dense local deposits of nanoparticles can form.

In Chapter 4, the *in situ* imaging capabilities of cryo-TEM are applied to study a phase transformation from the iron oxyhydroxide phase akaganeite, to the iron oxide phase hematite. It has been suggested that the growth of hematite nanoparticles can be driven by an oriented aggregation process.[13,14] With cryo-TEM, it is possible to reveal the hematite particle morphology in detail, and to reveal the aggregation state of the suspensions as the transformation

proceeds. This chapter addresses the relationship between aggregation processes and phase transformations.

Finally, Chapter 5 focuses on the process by which akaganeite particles are initially formed from aqueous ferric chloride solutions. The aim of this study is to better characterize nanoparticle nucleation and growth processes. This has relevance to the production of engineered nanoparticles and the characterization of precipitation processes in general. The system studied is ideal, in that nucleation and growth rates can be systematically controlled by manipulating $FeCl_3$ concentration and temperature.[15] *In situ* SAXS techniques enable these processes to be directly characterized. Subsequent nucleation and growth modeling allows fundamental physical parameters such as the akaganeite-water interfacial tension to be determined, providing new insights into the energetics of oxyhydroxide-water interfaces. This approach allows iron oxyhydroxide nucleation rates to be described in quantitative way, which is a necessary step, so that future work can untangle the complex interactions between nucleation, growth, and aggregation processes.

Together, these chapters highlight the complex structures and behaviors that can arise in just simple aqueous suspensions of ferric iron nanoparticles. As materials scientists are well aware, microstructural and nanostructural features can have a profound impact on the physical properties and behavior of a material. Complex microstructures and nanostructures are ubiquitous in environmental systems, even if they have not yet been characterized. There is still much to be learned about the interplay between mineral nanostructures and their physical behavior, especially in aqueous systems. These studies demonstrates ways in which careful, *in situ* structural characterization can shed light on important physical processes such as aggregation, transport, nucleation, and phase transformation.

1.1 Works Cited

1. Cornell, R.M; Schwertmann, U. *The Iron Oxides: Structure, Properties, Reactions, Occurences and Uses, 2nd Edition*; Wiley-VCH: Weinheim, 2003.
1. Lloyd, J.R.; Lovley, D.R.; Macaskie, L.E. Biotechnological Application of Metal-reducing Microorganisms. *Adv. Appl. Microbiol.* **2003**, *53*, 85-128.
2. Novikov, A.P.; Kalmykov, S.N.; Utsunomiya, S.; Ewing, R.C.; Horreard, F.; Merkulov, A.; Clark,S.B.; Tkachev, V.V.; Myasoedov, B.F.; Colloid Transport of Plutonium in the Far-Field of the Mayak Production Association, Russia. *Science*. **2006**, 314, 638-641.
3. Hassellöv, M.; Kammer, F. Iron Oxides as Geochemical Nanovectors for Metal Transport in Soil-River Systems. *Elements* **2008**, *4*, 401-406.
4. Liu, J.; Aruguete, D.M.; Murayama, M.; Hochella, M.F. Influence of Size and Aggregation on the Reactivity of an Environmentally and Industrially Relevant Nanomaterial (PbS). *Environ. Sci. Technol.* **2009**, *43*, 8178-8183.
5. Gilbert, B.; Ono, K. R.; Chin, K.A.; Kim, C.S. The Effects of Nanoparticle Aggregation Processes on Aggregate Structure and Metal Uptake. *J. Colloid Interface Sci.* **2009**, *330*, 285-295.
6. Gilbert, B.; Lu, G. P.; Kim, C. S. Stable Cluster Formation in Aqueous Suspensions of Iron Oxyhydroxide Nanoparticles. *J. Colloid Interface Sci.* **2007,** *313*, 152-159.
7. Burleson, D. J.; Penn, R. L. Two-Step Growth of Goethite from Ferrihydrite. *Langmuir* **2006**, *22*, 402-409.
8. Yuwono, V.M.; Burrows, N.D.; Soltis, J.A.; Penn, R.L. Oriented Aggregation: Formation and Transformation of Mesocrystal Intermediates Revealed. *J. Am. Chem. Soc.* **2010**, *132*, 2163–2165.
9. Li, D; Nielsen, M.H.; Lee, J.R.; Frandsen, C.; Banfield, J.F.; De Yoreo, J. J. Direction-Specific Interactions Control Crystal Growth by Oriented Attachment. *Science* **2012**, *336*, 1014-1018.
10. Kelton, K.F.; Greer, A.L. *Nucleation in Condensed Matter: Applications in Materials and Biology;* Pergamon: Oxford, UK, 2010.
11. De Yoreo, J.J.; Vekilov, P.G. Principles of Crystal Nucleation and Growth. *Rev. Mineral. Geochem.* **2003**, *54,* 57-93.
12. Jolivet, J.P., *Metal Oxide Chemistry and Synthesis.* John Wiley & Sons: West Sussex, 2000; pp. 25-137; Translated by E. Bescher.
13. Ocaña, M.; Morales, M.P.; Serna, C.J. The Growth-Mechanism of Alpha-Fe2O3 Ellipsoidal Particles in Solution. *J. Colloid. Interface Sci.* **1995**, *171*, 85-91.
14. Almeida, T. P.; Fay, M.V.; Zhu, Y. Q.; Brown, P. D. A Valve-Assisted Snapshot Approach to Understand the Hydrothermal Synthesis of Alpha-Fe_2O_3 Nanorods. *CrystEngComm* **2010**, *12*, 1700-1704.
15. Atkinson, R.J.; Posner, A.M.; Quirk, J.P. Crystal Nucleation and Growth in Hydrolyzing Iron(III) Chloride Solutions. *Clays Clay Miner.* **1977**, *25,* 49-56.

Chapter 2: Determination of the Three-dimensional Structure of Ferrihydrite Nanoparticle Aggregates

Aggregation impacts the reactivity, colloidal stability, and transport behavior of nanomaterials, yet methods to characterize basic structural features of aggregates are limited. Here, cryo-transmission electron microscope (Cryo-TEM) based tomography is introduced as a method for directly imaging fragile aggregates of nanoparticles in aqueous suspension and present an approach for extracting quantitative fractal dimensions from the resulting three-dimensional structural models. The structural quantification approach is based upon the mass autocorrelation function, and is directly comparable with small angle X-ray scattering (SAXS) models. This approach can enable accurate characterization of aggregate structure, even in suspensions where the aggregate cluster size is highly polydisperse and traditional SAXS modeling is not reliable. This technique is applied to study real suspensions of ferrihydrite nanoparticles. By comparing tomographic measurements with SAXS based measurements, it can be inferred that certain suspensions contain polydisperse aggregate size distributions. In other suspensions, fractal-type structures are identified with low intrinsic fractal dimensions. The fractal dimensions are lower than would be predicted by simple models of particle aggregation. This allows very large, low density aggregates to exist in stable colloidal suspension.

2.1 Introduction

The ability to accurately characterize nanoparticle aggregates is a pressing scientific need. Aggregation of nanoparticles impacts their reactivity, colloidal stability, transport behavior, and biological interaction with particles.[1,2,3]

Traditional methods for aggregate characterization are limited in their ability to resolve nanoscale structures in aqueous solution. Direct imaging methods, such as transmission electron microscopy (TEM) are traditionally performed on dried samples, and are likely to destroy or alter fragile aggregate features. Recently, cryogenic transmission electron microscopy (cryo-TEM)[4] has been introduced as a method for direct *in aqua* imaging of nanoparticles[5] and nanoparticle aggregates[6]. This method utilizes rapid quenching to produce thin films of vitreous ice, preserving the nanoparticle aggregate intact for observation in the TEM. In this chapter, cryo-TEM methodologies are extended to obtain cryogenic electron tomography[7] (cryo-ET) images of nanoparticle aggregates *in aqua*. It is now possible to generate full, three-dimensional representations of an aggregate structure.

In the absence of direct structural images, scientists have historically relied on indirect methodologies such as small angle X-ray scattering (SAXS) to characterize nanoparticle aggregates. SAXS provides quantitative structural data, but interpretation requires an accurate *a priori* understanding of the relevant structural features. Often, the assumption is made that

colloidal aggregates possess a branched fractal structure,[8,9] but cryo-TEM allows the true structure to be determined unambiguously and directly.

Ferrihydrite is a common, naturally occurring ferric oxyhydroxide mineral that often occurs as nanoparticulate aggregates. Because of ferrihydrite's nanoparticulate size, its precise crystal structure is still a matter of debate.[10,11] The aggregate structure of ferrihydrite nanoparticles can be expected to have important impact on their environmental behavior. In aqueous systems, heavy metals can sorb to ferrihydrite surfaces.[3] Subsequent transport of ferrihydrite aggregates will influence contaminant distribution within the environment. Ferrihydrite also serves as an important electron acceptor for iron reducing microorganisms.[12] Aggregate structure may impact bioavailability and thus influence microbial communities, and ferrihydrite particles are known to form complex colloidal structures, including stable particle aggregates.[13] Historically, it has been difficult to accurately characterize these structures, due to the presence of diverse particle shapes and aggregate sizes. In this chapter, an integrated approach is presented to characterize complex aggregate suspensions. Cryo-TEM results are used to determine the structural parameters (such as fractal dimension and particle size) that should be incorporated into an appropriate SAXS model. Subsequently, SAXS data can be used to describe the suspension ensemble in a statistically robust way. Ferrihydrite nanoparticles are shown to form a wide diversity structures, including branched fractal networks with a remarkably linear structure, which are described quantitatively by a low intrinsic fractal dimension. This allows very large range of aggregate sizes to develop in suspension, from small clusters to very large (micron scale) aggregates. Such configurations may lead to misinterpretation of SAXS data unless properly accounted for.

2.2 Experiment

2.2.1 Particle Synthesis

35 mL suspensions of iron oxyhydroxide nanoparticles were formed via microwave flash precipitation from ferric nitrate, as described by Guyodo.[14] Final ionic strength was adjusted by dialysis against 18 MΩ water, to a final conductivity of < 200 µS/cm, and pH of approximately 4.5 (note that suspension was not buffered). X-ray diffraction confirms 6-line ferrihydrite phase. Precipitate mass fraction is ~3.5 mg/mL. When stored at 4 °C, these suspensions are stable against flocculation and aggregate reconstruction for several months.

Nanoparticles were prepared in multiple batches so as to generate sufficient material for all analyses. Batches Syn10 and Syn15 were used for SAXS and TEM analysis. Syn10 was stored at 4 °C for approximately one year prior to analysis whereas Syn15 was characterized soon after synthesis. To evaluate the impact of long-term storage on aggregate structure, Syn15 was analyzed with SAXS and Cryo-TEM after storage at 4 °C for 1 month and 8 months. Three subsamples of Syn15 were also taken immediately after synthesis, then aged for 10 days at 4 °C, 35 °C, and 55 °C, respectively, to assess the impact of temperature on aggregate reconstruction. Prior to analysis, all samples were diluted to appropriate concentrations for SAXS and TEM by adding150 µL into 18 MΩ water to reach a final volume of 1.5 mL. SAXS experiments at

different dilution factors shows that dilution with deionized water does not significantly impact the aggregate structure, and this method also enables complimentary experiments where solution chemistry is controlled (not included in this study).

2.2.2 Cryo-TEM

Cryo-TEM samples were prepared by applying a 2-3 µL drop of diluted ferrihydrite suspension onto a carbon-coated lacey Formvar TEM grid (Ted-Pella, P.N. 881F). Prior to application, grids were made hydrophilic by plasma discharge and rinsed with a 2 mM $NaNO_3$ solution to optimize sample-grid interactions. For tomographic datasets, 1 µL of 10nm citrate capped gold colloid (BBInternational) was pre-applied to the grid and allowed to dry before sample application; these particles serve as fiducial markers for image registration.

Excess suspension was removed by blotting with cellulose filter paper, to leave a thin film (~100-300 nm thick) of suspension on the lacey grid. The grid was plunged into liquid ethane at -180 °C, quenching rapidly enough to produce a vitreous (glassy) ice with the aggregate structure preserved intact. The vitreous ice is electron transparent, allowing the aggregate structure to be imaged directly in TEM using a cryo-chilled (-180 °C) stage.

Cryo-TEM is performed using 200 keV Phillips CM200, and an energy filtered 300 keV JEOL3100 at Lawrence Berkeley National Laboratory. In addition to traditional 2D images, five tomographic reconstructions were acquired using the JEOL 3100. These reconstructed volumes contained extended aggregates, frozen intact within a film of ice. Each tomographic dataset consists of 65-70 images, acquired at 2° intervals, with maximum tilt angle of ±70° (single tilt axis). Three datasets were obtained of Syn10, with 0.542 nm pixel (voxel) size, and two of Syn15, with 0.224 nm pixel (voxel) size. Image contrast was produced by a combination of incoherent scattering and phase contrast imaging, with optimal defocus between 500 nm and 2000 nm.

2.2.3 Tomographic Reconstruction

Tomographic tilt series were aligned by gold fiducial tracking in the IMOD software package,[15] and reconstruction of the 3D volume was performed using the SIRT backprojection algorithm in tomo3D.[16] The resulting tomogram has a size of 1024x1024x512 voxels or 2056x2056x512 voxels. The computed 3D volume is then segmented to distinguish particle from the ice background. The automated trainable segmentation algorithm in FIJI [17] was used; it provided superior results when compared with manual segmentation approaches such as intensity thresholding of a bilateral filtered volume. After segmentation, the binary image was cleaned using a 3D erosion and dilation filter sequence (an opening filter). This produces a three dimensional aggregate model from which physical properties can be computed. An example of the segmentation is provided in Figure 1. Upon careful examination, it can be seen that particle size is not completely preserved.
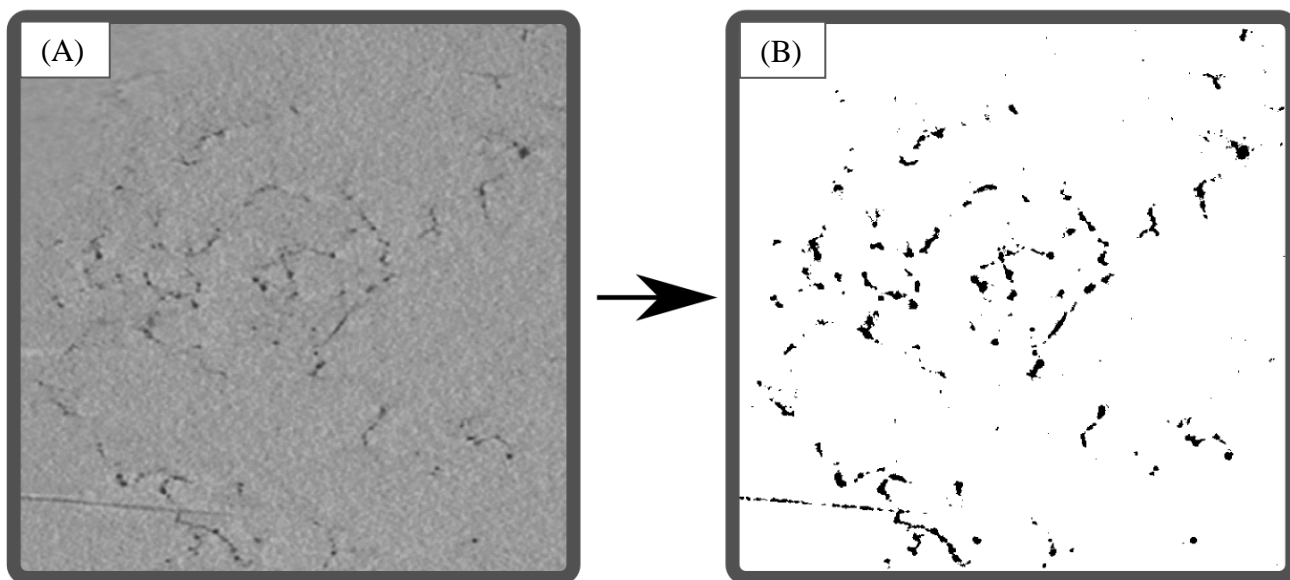
Figure 1: Example of two-dimension slice from a cryo-TEM tomogram. (A) Cross section from an original tomographic reconstruction. Dark regions inidcate ferrihydrite particles. (B) Corresponding segmented cross section. Three dimensional structural models are constructed by segmenting each tomogram slice.

2.2.4 Small Angle X-Ray Scattering

SAXS analysis of aqueous suspensions was performed at ALS beamline 7.3.3, Lawrence Berkeley National Laboratory, over a scattering q-range of 0.08 nm^{-1} to 4 nm^{-1}. The scattering vector is defined relative to the 2θ scattering angle and x-ray wavelength as $q = 4\pi \sin(\theta)/\lambda$. Scattering was performed in transmission mode, with sample thickness of 1 to 2 mm and X-Ray wavelength of 0.124 nm. Scattering patterns were acquired on a Pilatus 1M CCD. Scattering angle was calibrated with a silver behenate reference, and deionized water reference solutions were characterized for background subtraction.

SAXS data was processed into 1-D radial curves using the IRENA software package.[18] These 1-D curves were fit to analytical models using an iterative least-squares fitting approach. The models, described in greater detail in the Theory and Calculations section, considered the influence of primary particle radius, particle size distribution, aggregate fractal dimension, and aggregate cluster size.

2.3 Results

2.3.1 Cryo-TEM

Cryo-TEM analysis of ferrihydrite suspensions revealed branched aggregate structures, composed of roughly spheroidal primary particles (Figure 2). The number weighted size distribution of primary particles was evaluated by manually counting particles in high magnification TEM images ($\geq$150 kX). Syn10 possessed a mean radius, R_p= 1.25 nm, with a standard deviation in particle size ΔR_p= 0.31 nm (based on 320 particles), while for Syn15, R_p=

1.31 nm and ΔR_p = 0.55 nm (based on 385 particles). Some micrographs recorded for Syn15 indicate a bimodal primary particle size distribution.

Syn10, shown in Figure 2, was aged at room temperature for 1 year prior to analysis. Particles are arranged into a network of branched, linear chains. Approximately 10 % of the sample (by volume) consisted of lath-like particles. Previous studies using the same synthesis have identified similar rods as goethite[19], but the identity here is uncertain, as no diagnostic goethite peaks were detectable in X-ray diffraction patterns. The suspension was highly aggregated: most of the sample consisted of micron scale aggregates, but the aggregates show an open structure with fairly low density of particles and significant open space.

Syn15 cryo-TEM samples also contained fractal aggregates, but with a different structure from those in Syn10. None of the Syn15 samples contained lath-like particles, even after thermal aging. Samples prepared 12 days after synthesis showed very high polydispersity of aggregate sizes, ranging from just a few particles across to micron scale (see Figure 3 (A)). The linear motif seen in Syn10 is less obvious in Syn15; dense clusters of particles seem more prevalent. Sub-batches of Syn15 aged at different temperatures were indistinguishable from each other. Samples of Syn15 prepared after storage for 8 months were structurally similar to those prepared after 12 days, but the aggregate cluster size was larger (smaller clusters were uncommon) (Figure 3b). Rarely, large aggregates that have very high particle densities are found.
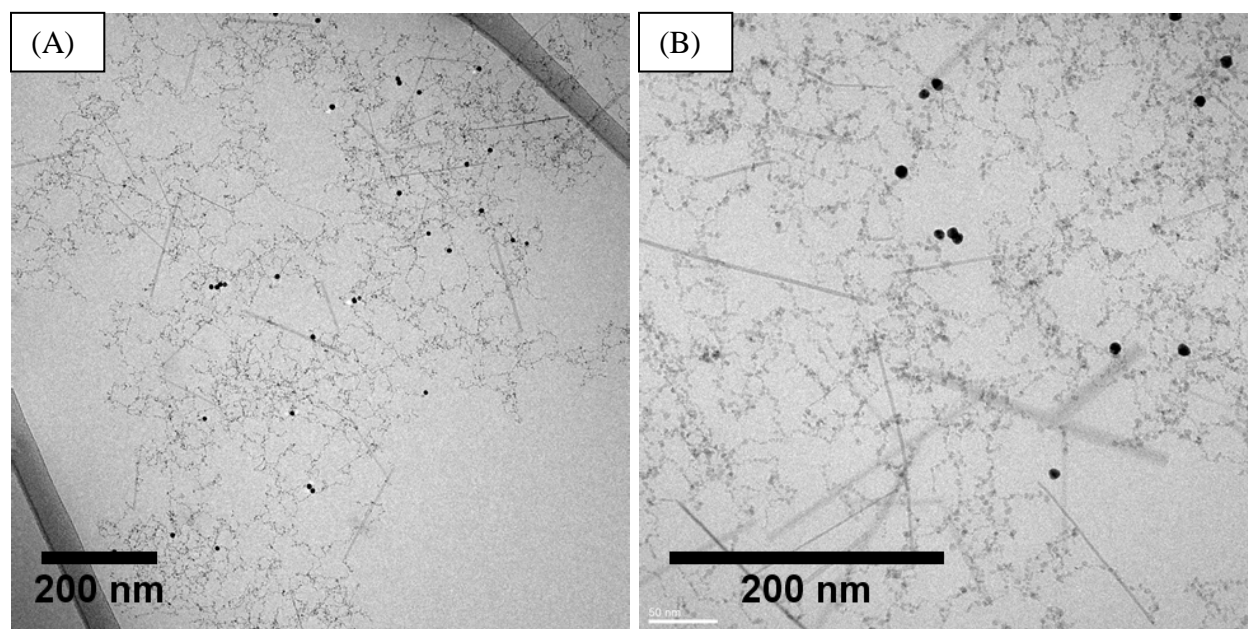
Figure 2. Representative cryo-TEM images of Syn10 in dionized water. (A) 50 kX, JEOL 3100 image. (B) 120 kX, JEOL3100 image. Both images show extended nanoparticle aggregates. The linear-branched particle chain structure is apparent, with a very limited amount of collapse into denser clumps. During aging, some fraction of particles have transformed into rods (~200 nm long). High contrast (dark) spherical particles are gold fiducial nanoparticles. The carbon coated formvar support is visible in (A) in the upper right and lower left corners. There is some degree of mottling visible on the ice surface, but general transparency and lack of strong diffraction contrast indicates that the bulk the ice in these samples is vitreous.

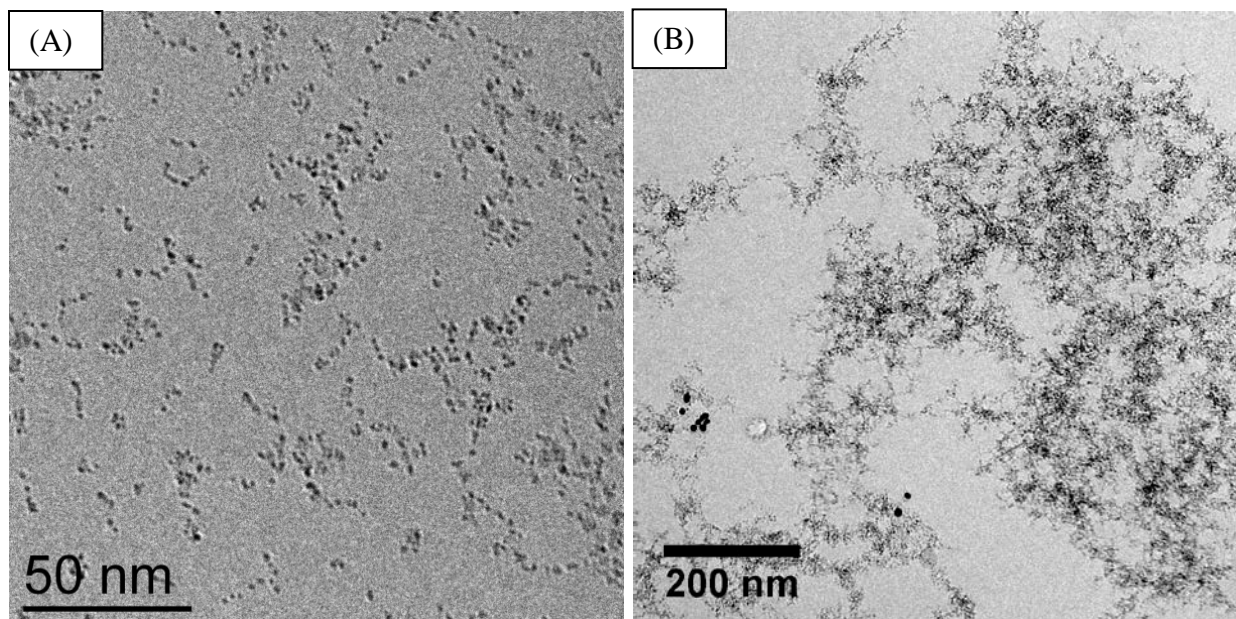**Figure 3. Cryo-TEM images from Syn15 in deionized water (A), image taken at 115 kX, CM200. Primary particles (3-5 nm diameter) are observed to cluster into small aggregates.The chain like nature of particle clusters can be observed. Most aggregates are of limited extent, and may range from just a few particles, to many thousands of particles. (B) Image taken at 60 kX, JEOL 3100. This shows a large Syn15 aggregate. The aggregates in Syn15 samples generally appear to be more densly packed than those seen in Syn10.**

2.3.2 Tomographic Reconstructions

Three cryo-ET volumes were characterized that correspond to Syn10, and two tomographic volumes were prepared that correspond to Syn15. Volumes of 370nm x 370nm x 90nm are extracted from two different tomograms, and shown in Figure 4. Distinct differences can be seen between the two samples in terms of primary particle shape and aggregate structure. The reconstruction of Syn10 shows linear particle chains, and displays lath-shaped particles that are not present in any Syn15 samples. Syn15 appears to be more coarsely aggregated, with particles localized in denser clusters.

In most tomographic volumes, the ice thickness is between 100 and 200 nm thick. However, in some of the Syn10 reconstructions (volume 2), ice is less than 100 nm thick, and the aggregate shows signs of reconstruction due to confinement. This is apparent, due to a high density of particles sitting at the surface of the ice. See supplemental information for additional perspectives of the tomographic volumes.
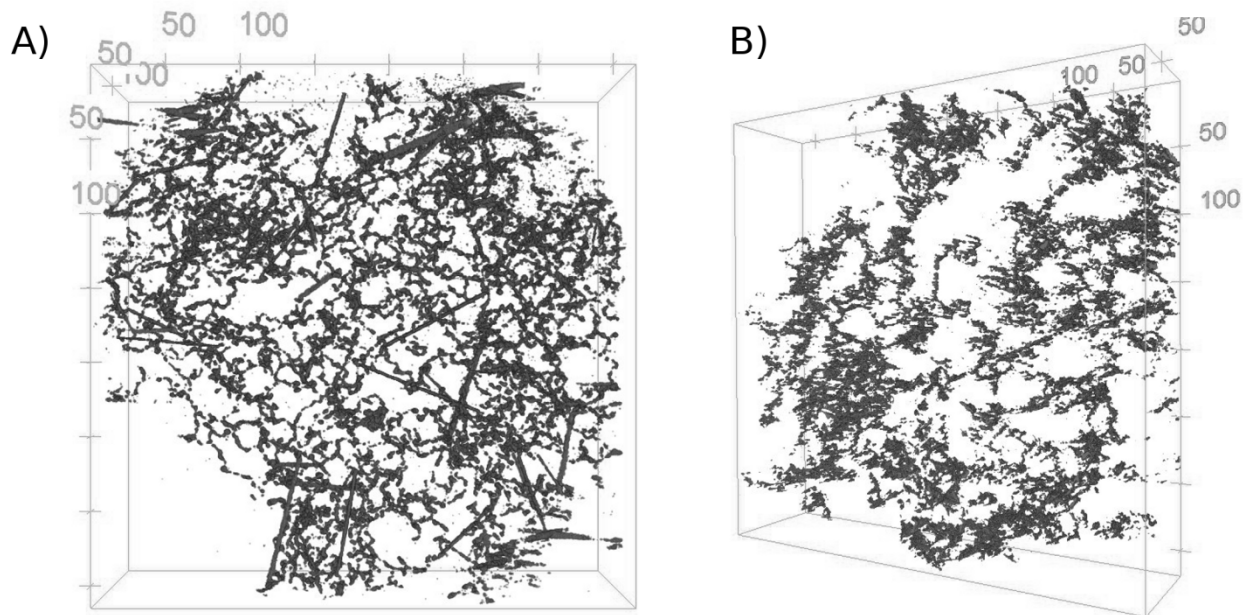
Figure 4. Two different tomographic reconstructions, both spanning volumes of 370nm x 370nm x 90nm. (A) Syn10, particle volume fraction is ~2.2% (B) Reconstruction of Syn15, particle volume fraction is ~1.3%. Although both samples display a fractal-type structure, Syn15 has a greater tendency toward particle clustering to form course structures, while the particles in Syn10 tend to form more linear chains that are more evenly distributed throughout the aggregate.

2.3.3 SAXS Results

In addition to the cryo-TEM analyses of samples described above, Syn10 and the suite of Syn15 samples were characterized by SAXS. Representative 1-D SAXS curves, $I(q)$, are shown in Figure 5. An apparent fractal power-law regime can be observed for values of $q < {\sim}0.6$ nm^{-1}. At higher q-values ($q > 2$ nm^{-1}), the Porod regime is observed, in which $I(q) \sim q^{-4}$ (however, uncertainties in the background subtraction have greatest impact at high q values, which may lead to deviations from Porod behavior). Where $1/q$ is much greater than the aggregate size, a low-q plateau should be observed. Unfortunately, this plateau is not visible within the experimentally accessible q-range, which means that SAXS-measurements alone cannot be expected to fully constrain the aggregate cluster size distribution. The low-q slope of Syn10 is markedly steeper than all Syn15 samples, suggesting an *apparently* higher fractal dimension. Thermal aging and long term storage have a very subtle influence on Syn15, only appearing to slightly smooth the low-q scattering signal. Data range for Syn15 at 8 months is truncated due a change in the SAXS beamline configuration.

These scattering curves were fit using a variation of the Teixeira fractal aggregate model.[20] This model describes $I(q)$ as a function of R_p (average primary particle radius), ΔR_p (primary particle size distribution breadth), d_f (mass fractal dimension), and ξ (cluster size parameter). The details of this fitting model will be discussed under Theory and Calculations.

SAXS fitting provides an estimate of primary particle size (R_p) that is in good agreement with TEM measurements. For Syn10, R_p is estimated at 1.24 nm from SAXS. The primary particle

size of Syn15, is estimated at 1.23 nm in freshly prepared samples, 1.65 nm after 1 month and 1.81 nm after 8 months. This could be due to Ostwald ripening, or it could simply reflect an increase in the average particle coordination number (number of particle-particle contacts) over time, since both have a similar impact on the SAXS pattern. Estimates of fractal dimension are not reliable, because the values of ξ and d_f are inversely correlated, and this dataset does not cover a wide enough q-range to determine both independently. As a first fitting attempt, ξ was fixed at 400 nm (based on the observation that most aggregates are of this size or larger). With this parameter fixed, d_f for Syn10 was estimated to have a value of 1.02; this value is indicative of highly linear structures. Attempts to fit Syn15 with this approach were unsuccessful; the apparent value of d_f for all Syn15 samples ranged from 0.4 to 0.6. These very low apparent fractal dimensions of less than 1 are physically unrealistic. The most probable explanation for this discrepancy is that Syn15 possesses a wide range of aggregate sizes, including a significant population of smaller clusters. Such polydispersity can systematically affect the observed SAXS scattering curve, leading to apparent fractal dimensions that are lower than the true structural fractal dimension. This will be discussed further in the Theory and Calculations section. The Syn15 structure is also found to be fairly constant over time. Even after 8 months of aging, the low-q slope remains essentially unaltered.
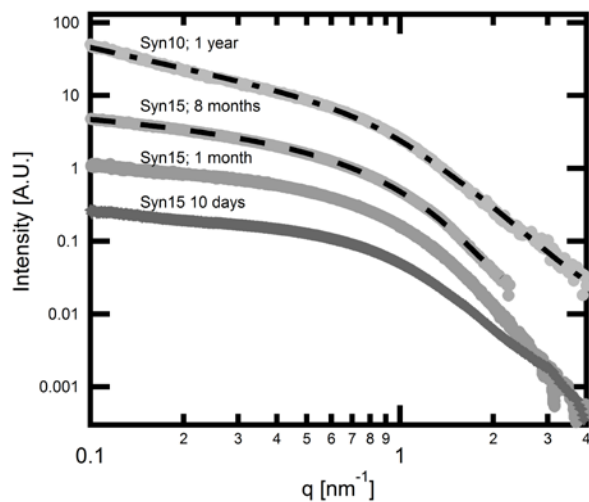

Figure 5. SAXS intensity profiles for Syn10, and Syn15 at different aging times. The fractal power law regime is observed for q-values of 0.6 nm^{-1} and less, and the Porod regime becomes evident for $q>2$ nm^{-1}. Dashed lines represent best fits with analytical models. The model fit for Syn10 assumes a monodisperse array of aggregates, with $\xi=400$ nm, and with $d_f = 1.02$. Syn15 curves can only be fit by assuming polydisperse aggregate distributions. Here, an adequate fit can be obtained when $d_f = 1.59$ and the polydispersity exponent has a value of $\tau = 2$.

2.4 Theory and Calculations

2.4.1 Mathematical Representation of Aggregate Structure

This section establishes the mathematical framework for integrating SAXS with cryo-TEM to obtain a more complete description of the structure. The ferrihydrite structure will be represented mathematically using a three dimensional density distribution function, $\rho(\boldsymbol{r})$. Experimental methods to describe $\rho(\boldsymbol{r})$ are limited. SAXS cannot provide $\rho(\boldsymbol{r})$ directly, but can only reveal

certain averaged properties. The segmented cryo-TEM tomogram can provide a direct measurement of $\rho(\boldsymbol{r})$, but only over some finite volume.

The finite volume that is imaged by cryo-EM can be represented mathematically using a window function, $V_{tomo}(\boldsymbol{r})$. This function has a value of 1 inside the tomographic volume and drops to zero outside the experimentally obtainable region. The tomographic image, $\rho_{tomo}(\boldsymbol{r})$, is then related to the full aggregate structure by Equation 1

.

Equation 1

$$\rho_{tomo}(\boldsymbol{r}) = V_{tomo}(\boldsymbol{r}) \cdot \rho(\boldsymbol{r})$$

Throughout this chapter, $\rho(\boldsymbol{r})$ is treated as a binary function with a value of $\Delta\rho$ when $\boldsymbol{r}$ lies within a particle and 0 if $\boldsymbol{r}$ lies in the solvent. For convenience in calculating SAXS patterns, $\Delta\rho$ is equated with the excess X-ray scattering length density of ferrihydrite relative to the solvent. When the density distribution function is treated as binary, this neglects smaller, molecular scale density fluctuations that exist within the solvent and precipitate. These fluctuations also contribute to the SAXS intensity (especially at high scattering angles), but rather than account for these fluctuations explicitly in the structural model, their contribution to the experimental scattering signal is removed by subtraction of appropriate reference scattering patterns (*i.e.* water blank standards).

2.4.2 Autocorrelation Function for Fractal Structures
The density autocorrelation function, defined as $\mathbb{P}(\boldsymbol{r}) = \rho(\boldsymbol{r}) * \rho(-\boldsymbol{r})$, is ideal for performing quantitative comparisons between SAXS and cryo-ET datasets, since it can be determined directly from both. Furthermore, there are close relationships between the behavior of a structure's autocorrelation function and its fractal dimension. $\mathbb{P}(\boldsymbol{r})$ can be directly related to the SAXS intensity profile by a simple Fourier transform, as shown in Equation 2. It follows from the definition of the autocorrelation function, that the SAXS intensity, $I(\boldsymbol{q})$ is fully determined by $\rho(\boldsymbol{r})$, although the converse is not true. As written in Equation 2, the SAXS intensity corresponds to the "differential scattering cross-section", a value that is independent of illuminated sample volume or photon flux.

Equation 2

$$I(\boldsymbol{q}) = \int \mathbb{P}(\boldsymbol{r}) \mathrm{e}^{-\mathrm{i}\boldsymbol{q}\cdot\boldsymbol{r}} \mathrm{d}\boldsymbol{r}$$

Most SAXS modeling approaches assume that the particles or aggregates possess some idealized geometry (*e.g.*, sphere, cylinder, or fractal) for which an analytical solution to Equation 2 can be obtained. Then, certain parameters (*e.g.,* particle radius, aspect ratio, or fractal dimension), are iterated until a best fit to the scattering intensity is obtained. Such SAXS analysis should be

interpreted with caution, because it is possible to obtain good fits to $I(\boldsymbol{q})$ or $\mathbb{P}(\boldsymbol{r})$ while using an incorrect physical model.

Early SAXS models for fractal aggregates were developed by Sinha[9] and Teixera[20]. These researchers proposed mass-autocorrelation functions to describe the structure of branched fractal aggregates, and then developed analytical expressions for the SAXS intensity profile that depend upon the aggregate fractal dimension (d_f), aggregate cluster size (ξ), and the shape of the primary particles. Cryo-TEM images confirm that Syn10 and Syn15 possess such branched, fractal-like structures (see Figure 2).

A major aim of this study is to obtain an estimate for the structural fractal dimension. This value has import ramifications for aggregate behavior (*e.g.,* sedimentation, mechanical strength, gelation)[23, 22] and provides insight into aggregation mechanism. Physically realistic values for d_f should be between 1 and 3. In traditional colloids, stochastic processes such as diffusion limited cluster aggregation (DLCA) have been shown to produce fractal dimensions of 1.6-1.9, while reaction limited cluster aggregation (RLCA) produces more densely packed aggregates with higher fractal dimension.[8,24]

There are several accepted methods for defining and estimating fractal dimension, and not all are strictly identical.[25,26] The fractal nature of aggregates was originally recognized through scaling laws in particle size and growth rates. Sinha[9] and Teixeira[20] both suggested on heuristic grounds that particle scaling laws will result in a power-law behavior in the mass autocorrelation function, which could be quantified using SAXS. Since that time, the mass autocorrelation function has become accepted by many researchers as a definitive property of fractal aggregates.[8,26] For an ideal fractal object embedded in three-dimensional space, $\mathbb{P}(\boldsymbol{r})$ displays a power law decay whose exponent depends upon d_f.[8]

Equation 3

$$\mathbb{P}(\boldsymbol{r}) \sim |\boldsymbol{r}|^{d_f - 3}$$

For real aggregates, relationship (3) can obviously only hold over some finite length scale. $|\boldsymbol{r}|$ must be larger than the primary particle diameter, $2R_p$, and smaller than a cutoff size, ξ. In the work of Teixeira, a simple model was developed for aggregate structure that accounted for this finite size and allowed the calculation of SAXS scattering patterns. In the following section, this model will be reviewed, in order to show how SAXS estimates of the fractal dimension are related to the autocorrelation function.

An important assumption in the Teixeira model is that aggregate suspensions are statistically isotropic and disordered on large scales. This has several benefits. Among these, $\mathbb{P}(\boldsymbol{r})$ and $I(\boldsymbol{q})$ can be replaced by their spherically averaged radial profiles, $\mathbb{P}(r)$ and $I(q)$, where $r = |\boldsymbol{r}|$ and $q = |\boldsymbol{q}|$. Rather than treat the full mass autocorrelation function, Teixeira's work focused on the dimensionless particle pair correlation function, which will be referred to as $P(r)$ in this chapter.

For suspensions of monodisperse spherical particles, $P(r)$ and $\mathbb{P}(r)$ contain essentially the same information, and are related to each other simply by convolution with a particle shape function. Teixeira developed an expression for $P(r)$ that is given in Equation 4 and then determined the corresponding SAXS structure factor, $S(q)$, that is given in Equation 5.

Equation 4

$$P(r) - 1 = \frac{D}{4\pi R_p{}^{d_f}} \cdot r^{d_f - 3} \cdot \exp\left(-\frac{r}{\xi}\right)$$

Equation 5

$$S(q) = 1 + \left(qR_p\right)^{-d_f} \frac{d_f \Gamma(d_f - 1)}{[1 + (q\xi)^{-2}]^{(d_f - 1)/2}} \sin\left[(d_f - 1)\operatorname{atan}(q\xi)\right]$$

Equation 4 possesses several important physical characteristics. At large distances, $P(r)$ converges to a constant value of 1. This is enforced by the exponential damping term, where ξ accounts for finite aggregate size by ensuring that significant correlations to not persist beyond the maximum aggregate size. The convergence of $P(r)$ to a constant value is a consequence of the isotropic nature of the suspension on large length scales. $P(r)$ has been normalized so that it converges to a constant value of one. The analogous behavior in $\mathbb{P}(r)$ is a convergence to $\Delta\rho^2\phi^2$, where ϕ represents the average volume fraction of the suspension. This behavior is in contradiction to the ideal fractal behavior of Equation 3, but must occur for real isotropic suspensions. The constant term does not contribute to observable SAXS intensity except at very small angles, thus is it is convenient to subtract the constant value when calculating the structure factor so that the integral in Equation 2 will not diverge. This subtraction is important to note, because it means that traditional SAXS models assume that the power-law behavior of $r^{d_f - 3}$ is manifest with respect to the function $P(r) - 1$, or if one is dealing with the mass autocorrelation function, with respect to $\mathbb{P}(r) - \Delta\rho^2\phi^2$. This must be accounted for when determining the fractal dimension from tomographic models, especially if results are to be compared with SAXS based measurements.

It should be noted that the structural model in Equation 4 is only approximate. For example, in a strictly correct model, a "pair correlation hole" should exist at small length scales to reflect the constraint that two particles cannot physically overlap. This is neglected here. Fortunately, these corrections are less important if the system has some degree of primary particle polydispersity. [27, 28] There is also considerable debate regarding the precise nature of the cutoff function for real aggregates; this will be addressed in greater detail in the next section.

In order to calculate the overall SAXS pattern, one must determine both the structure factor for the aggregate, and the primary particle form factor, $F(q)$. The total SAXS pattern is then given by

Equation 6. The term N_p/V is merely a normalization factor that accounts for the number of particles per unit volume.

Equation 6

$$I(q) = \frac{N_p}{V} \langle |F(q)|^2 \rangle S(q)$$

In this study, SAXS modeling is performed assuming that the primary particles can be modeled as a Gaussian distribution of spheres with an averaged radius R_p, and a distribution breadth, ΔR_p. The value of $\langle |F(q)|^2 \rangle$ can be readily determined for such a distribution. Iterative refinement is then used to fit the experimental SAXS data and obtain an estimate for d_f, R_p, ΔR_p and ξ. However, in complicated systems, such fits will be necessarily imperfect. In the following section, the limitations of this simple model are discussed, and cryo-ET is presented as a way to provide an independent check for the structural model.

2.4.3 Treating Polydisperse Aggregates

The Teixeira aggregate model (Equation 4) uses a simple, single exponential damping term to account for the finite size of aggregate clusters. However, real suspensions may contain a polydispersity mixture of aggregate sizes. Teixeira[20], Nicolai[21], and others have shown that aggregate size polydispersity can lead to apparent fractal dimensions that are lower than the true structural fractal dimension. This appears to be the case in Syn15, where cryo-TEM shows a wide range of aggregate cluster sizes, and SAXS fitting returned unphysically low apparent fractal dimensions of less than one.

For fractal aggregates, power-law size distributions are expected,[21,29] and the aggregate size distribution can typically be approximated as:

Equation 7

$$N(n) \sim n^{-\tau} \exp(-n/n_c)$$

Here, n represents the number of particles in a cluster, and n_c is an aggregate cutoff size. As aggregation proceeds, n_c will grow.[29] The term τ describes the shape of the aggregate size distribution, with larger values of τ resulting in a higher proportion of small clusters. Its value has been correlated with aggregation mechanism, with DLCA resulting in $\tau \approx 0$, RLCA resulting in $\tau \approx 1.5$, and as the system approaches the percolation threshold, $\tau \approx 2.2$. According to the work of Nicolai, the depression of apparent fractal dimension is greatest for systems where n_c is small and τ is large.[21] In this study, Nicolai's approach is used to numerically generate synthetic SAXS profiles for an ensemble of aggregates.

Equation 8

$$S_{ensemble}(q) = \frac{\sum N(n) S(q,n)}{\sum N(n)}$$

In Equation 8, the term $S(q)$ can be calculated directly from the Teixeira formula, when it is recognized that a scaling law exists relating the number of particles in a cluster to the cluster cutoff size, $\xi \cong R_p n^{-d_f}$. The ensemble scattering profile then becomes a function of R_p, ΔR_p, d_f, τ, and n_c, which can be easily calculated. However, the SAXS dataset is insufficient to constrain all five of these variables as fitting parameters. Certain parameters (such as d_f), must be constrained by alternative methods (cryo-TEM).

2.4.4 Estimating the Autocorrelation Function from Tomographic Volumes

Tomographic imaging provides an avenue for calculating d_f that is independent of assumptions about aggregate size distribution. However, cryo-ET is not generally capable of imaging these very large aggregates in their entirety; only a finite piece of the structure, $\rho(\boldsymbol{r})_{tomo}$, can be obtained. The effects of this truncation must be dealt with carefully. Previous authors have outlined how the truncation of an infinite ideal aggregate to finite cluster size will systematically impact that object's autocorrelation function.[30, 31] We have the analogous problem of trying to estimate $\mathbb{P}(r)$ for an idealized large aggregate when it is only possible to image to a small region of interest, $V_{tomo}(\boldsymbol{r})$. It is impossible to fully account for such sampling imperfections, but it is possible to remove their systematic effects to obtain a better estimate for the "intrinsic" structural fractal dimension

In this study, an approach for removing the systematic truncation effects is developed based on the work of Yanwei and Meriani.[31] Suppose first, that a homogenous, infinitely large structure has an autocorrelation function of $\rho(\boldsymbol{r}) * \rho(-\boldsymbol{r})$. If just a small piece of that is isolated with tomography, it can be shown that the autocorrelation function for that fragment is

Equation 9

$$\rho_{tomo}(\boldsymbol{r}) * \rho_{tomo}(-\boldsymbol{r}) \approx [V_{tomo}(\boldsymbol{r}) * V_{tomo}(-\boldsymbol{r})] \cdot [\rho(\boldsymbol{r}) * \rho(-\boldsymbol{r})]$$

Because $V_{tomo}(\boldsymbol{r})$ drops to zero beyond a certain regime, certain information is irretrievably lost during the application of Equation 9. However, if one wishes to obtain an unbiased approximation to $\mathbb{P}(\boldsymbol{r})$, it is necessary to apply the following correction:

Equation 10

$$\mathbb{P}(\boldsymbol{r}) = \rho(\boldsymbol{r}) * \rho(-\boldsymbol{r}) \approx \frac{[\rho_{tomo}(\boldsymbol{r}) * \rho_{tomo}(-\boldsymbol{r})]}{[V_{tomo}(\boldsymbol{r}) * V_{tomo}(-\boldsymbol{r})]}$$

Aggregate inhomogeneity can also produce major systematic influences, in a similar way. Although local inhomogeneity is inherent to fractal objects, when only a finite piece of a larger fractal is extracted, these local fluctuations can impede a direct assessment of the fractal dimension. Yanwei and Meriani identified this behavior in a mathematical analysis of finite aggregates, and similar behavior can be shown to occur in these tomographic samples. Their work projects that Equation 10 alone will often systematically overestimate $\rho(\boldsymbol{r}) * \rho(-\boldsymbol{r})$ at moderate distances (up to approximately one half the width of V_{tomo}), and underestimate

$\rho(\boldsymbol{r}) * \rho(-\boldsymbol{r})$ at higher distances. To correct for this, one must normalize $\rho_{tomo}(\boldsymbol{r}) * \rho_{tomo}(-\boldsymbol{r})$ by a factor that also accounts for particle density. The fully corrected autocorrelation function is estimated as follows:

Equation 11

$$\mathbb{P}(\boldsymbol{r}) = \rho(\boldsymbol{r}) * \rho(-\boldsymbol{r}) \approx \Delta\rho\phi \frac{(\rho_{tomo}(\boldsymbol{r}) * \rho_{tomo}(-\boldsymbol{r}))}{(\rho_{tomo}(\boldsymbol{r}) * V_{tomo}(-\boldsymbol{r}))}$$

Neither equation for estimating $\mathbb{P}(\boldsymbol{r})$ is entirely perfect. Based on analysis of real and synthetic aggregates, it's shown that Equation 10 provides poor results when applied to sample volumes that are not homogenously filled. In these cases, Equation 11 does a better job of producing correlation functions which decay monotonically to a constant value, and the resulting subtracted curves, $\mathbb{P}(r) - \Delta\rho^2\phi^2$ tend to display a more idealized power-law regime. However, it can be argued that Equation 11 is systematically ignoring certain long-range correlations that are inherent to the fractal structure, so for sample volumes that are large and isotropic, the correlation functions produced by Equation 10 may be more meaningful.

2.4.5 Analysis of Real and Simulated Tomographic Volumes.
The following computational pipeline has been used to obtain an estimate of $\mathbb{P}(\boldsymbol{r})$, and calculate the fractal dimension for each tomographic volume.

During initial data collection, a series of tomographic volumes were obtained using cryo-TEM. Individual, very large aggregates were selected for imaging, because the autocorrelation functions for these structures has the potential to display the ideal r^{d_f-3} fractal behavior over the largest length scales. After segmentation to produce a binary structure, each tomogram is resized (downsampled 4x) and broken into subvolumes of 128x128x128 voxels. The actual tomogram data may not completely fill each subvolume. In this case, V_{tomo} was defined as a region of interest within the subvolume. Only those subvolumes that were mostly spanned by the aggregate were used for further analysis.

The ideal autocorrelation function was estimated from subvolume, using both Equation 10 and Equation 11 (for comparison). The autocorrelations and cross correlations were computed numerically, using zero-padded 3D FFT based algorithms in SciPy.[32] The resulting three dimensional correlation functions are then spherically averaged and normalized to obtain $\mathbb{P}(r)$.

For aggregates that mostly span their tomographic volume, $\mathbb{P}(r)$ estimated in this way converges toward a constant value of approximately $\Delta\rho^2\phi^2$ at large correlation lengths. This constant term is subtracted, and the power law slope of $\mathbb{P}(r) - \Delta\rho^2\phi^2$ is measured. These steps are shown graphically in Figure 6, for the computation of a single subvolume (from Syn 10, volume 1). Curve (a) shows $\mathbb{P}(r)/\mathbb{P}(0)$, which has been obtained by application of Equation 11. As expected, this converges toward a constant value of $\Delta\rho^2\phi^2/\Delta\rho\phi^2$ at large distances (within the limits of statistical noise). However, if neither Equation 10 nor Equation 11 is applied, the finite

18

subvolume effects will cause long range correlations to drop toward zero. Curve (b) shows the final, subtracted curves from which fractal dimension can be estimated. The fractal slope is only measured over a finite length scale, where r is greater than the primary particle diameter, but less than some value where noise begins to dominate the signal. For most subvolumes, reasonable correlations were obtained between 5 nm and 55 nm. To guide the eye, a line with slope of -2 (corresponding to a fractal dimension of 1) is shown in Figure 6. The fractal dimension for a tomographic volume is estimated by averaging the fractal dimension determined for each subvolume. It is important to note, that the processing steps outlined above are only appropriate for extracting the fractal dimension of objects which have short-range fractal order, and converge to a random isotropic behavior at longer correlation lengths (within the length-scale of the sample volume). A different approach must be used for objects that don't show this behavior.
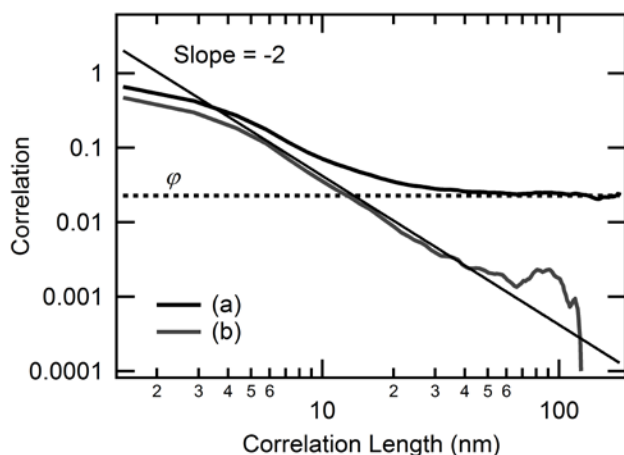

Figure 6. Curve (a) shows the estimated autocorrelation function, $\mathbb{P}(r)$, for a subvolume for Syn10 volume 1, as estimated by numerical computation and application of Equation 11, and normalized by $\mathbb{P}(0)$. As expected, this curve now converges toward a constant value ϕ at large r. In curve (b), the constant ϕ term has been subtracted to reveal the power law decay. This particular volume has a slope of roughly -2, which corresponds to a fractal dimension of 1.

In some cases, the primary particle shape effects may reduce the size of the power law regime and slightly impede acquisition of the fractal dimension. For comparison, the calculations have also been performed on a "skeletonized" version of the aggregate structure. The skeleton was calculated in Fiji, using 3D erosion and skeletonization routines. Recalling that $P(r)$ is related to $\mathbb{P}(r)$ by a three dimensional convolution, the autocorrelation function obtained from a skeletonized structure should provide a closer approximation to $P(r)$.
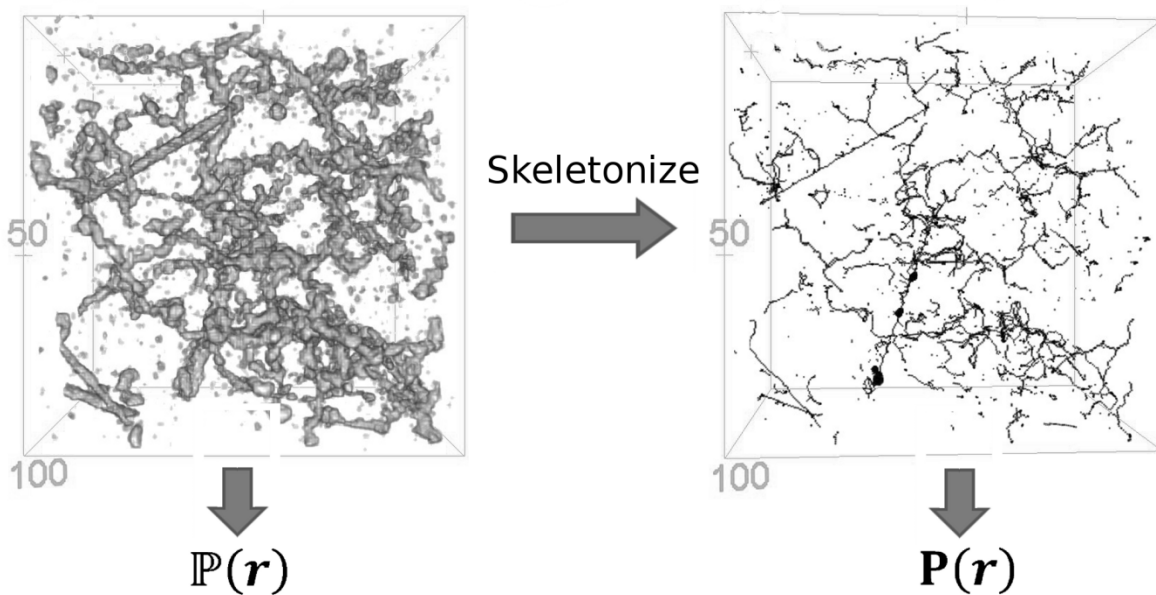
Figure 7. A 100x100x100 nm tomographic volume, used for the estimation of $\mathbb{P}(r)$, and the corresponding aggregate skeleton, which can be used to obtain an estimate for the power law dependence in P(r), with less influence from particle shape.

Estimates for d_f obtained by various methods are given in Table 1. The full tomographic structures typically show a slightly higher fractal dimension than their skeletonized counterparts. The difference is generally small though, suggesting that the measurement is fairly insensitive to particle shape, as hoped. For calibration, the method has been applied to the characterization of computationally generated DLA (distinct from DLCA) aggregates, which are expected to have fractal dimensions on the order of 2.5.[8] In each of these cases, the use of Equation 10 shows better agreement with expected values than Equation 11.

Dividing each sample into subvolumes prior to analysis allows the computation to be performed more rapidly (using ~16 GB of memory); because samples possess various types of structural heterogeneity, it also allows for a discussion of how specific physical characteristics relate to a fractal parameter.

In a comparison of processing methods, Equation 10 is found to provide higher estimates of the fractal dimension than Equation 11 when most of the aggregate's mass is located near the center of the tomographic subvolume. Conversely, if most of the aggregate mass is located near the edges of the tomographic subvolume, Equation 11 provides higher estimates of the fractal dimension than Equation 10.

In certain tomograms, especially Syn10 vol 2 and parts of Syn10 vol 3, it was found that confinement of the aggregates within a thin ice layer has caused a layer of particles to collect at the ice-vacuum interface (originally the water-air interface). When this type of aggregate restructuring occurs within a tomogram subvolume, the apparent fractal dimension trended

towards larger values, approaching a value of two or more. This reflects the planer geometry of the particle accumulation. During the analysis of three tomographic volumes, the bulk of Syn10 appears to possess a very low intrinsic fractal dimension, somewhere between 1 and 1.4 (depending on measurement technique), but any given tomographic subvolume may possess an apparently larger fractal dimension if particles happened to accumulate at the surface. In particular, Syn10 volume 2 had significant surface reconstruction, and the fractal dimensions calculated from that tomogram should not be considered representative of the structure in bulk solution.

Table 1 (error designates estimated standard deviation of the mean):

Sample	d_f (Eq. 10)	d_f (Eq. 10) skeletonized	d_f (Eq. 11)	d_f (Eq. 11) skeletonized	Length scale probed
Syn15 vol 1	1.6 ± 0.1	1.5 ± 0.2	1.6 ± 0.1	1.5 ± 0.1	5 nm - 55 nm
Syn15 vol 2	1.9 ± 0.2	1.7 ± 0.2	1.7 ± 0.1	1.5 ± 0.3	5 nm - 50 nm
Syn10 vol 1	1.3 ± 0.1	1.2 ± 0.2	1.0 ± 0.2	1.0 ± 0.2	5 nm – 55 nm
Syn10 vol 2 *	1.8 ± 0.2	1.8 ± 0.2	1.7 ± 0.2	1.7 ± 0.1	5 nm – 55 nm
Syn10 vol 3	1.4 ± 0.1	1.4 ± 0.1	1.3 ± 0.2	1.3 ± 0.2	5 nm – 55 nm
Synthetic DLA	2.2 ± 0.05	2.2 ± 0.05	2.0 ± 0.05	2.0 ± 0.05	2 rad – 20 rad

*These relatively high fractal dimension reflect aggregate reconstruction due to confinement within a thin-film by ice surfaces.

Compared with Syn10, Syn15 displays much higher fractal dimensions. This was somewhat surprising, since Syn15 had an apparently lower fractal dimension when measured with SAXS. However, in complex suspensions, a single fractal dimension is incapable of fully describing the aggregation state. Cryo-TEM methods show that on the local scale, Syn15 clusters can be quite densely packed. However, they also reveal a suspension that is a mixture of very large aggregates and many very small particle clusters. In this case, suspension polydispersity can explain the apparent discrepancies between SAXS based and tomographic based measurements of the fractal dimension. It is possible to fit the SAXS scattering profiles, using a fractal dimension of 1.5 or greater, if one supposes a polydisperse aggregate suspension where the cluster polydispersity exponent, τ, is between 2.0 and 2.2. One such fit has been shown in Figure 5.

2.5 Discussion

Cryo-tomography clearly shows that ferrihydrite particle suspensions may aggregate to form branched aggregate structures. These appear to be fractal-like with low intrinsic fractal dimensions. The application of fractal concepts to aggregates is common, but it can be difficult to obtain reliable quantitative measurements. For example, the aggregate structure of Syn15 would not have been apparent from SAXS analysis alone, since cluster polydispersity interferes with a dependable assessment of fractal dimension.

This study highlights the difficulty of performing SAXS modeling of polydisperse aggregate systems. In the process of this work, another difficulty in performing SAXS experiments was encountered. Very rarely, a Syn15 SAXS dataset possessed anomalously large scattering in the

low-q regime. This was initially regarded as an experimental error, as the signal typically disappeared upon repetition. However, based on the analysis that Syn15 consists of highly polydisperse aggregates, another explanation is possible. The power law cluster distributions described by Equation 8 are 'long tail distributions' in which a few very large clusters have the potential to dominate scattering. If such expressions truly hold for Syn15, then large statistical fluctuations in the amount of scattering from large aggregates are expected. The occasional inclusion of just one very large aggregate in the scattering volume could lead to the anomalous low-q scattering that was observed. It is in complex systems like this, where cryo-TEM provides a critical, localized viewpoint for describing the structures.

Complexities arise because the nanoparticle aggregates, while fractal like, are not truly scale invariant structures. They consist of finite size particles, and possess many other characteristic length scales as well. Extracting the fractal dimensions from such complex systems with cryo-tomography is not trivial. As discussed, finite volume effects must be carefully accounted for, and multiple sample volumes should be considered for statistical reliability. With this system, the fractal power law behavior was only quantifiable over a limited range (approximately 5 nm to 50 nm).

The level of structural diversity within a given sample and between samples is notable, but the physical cause for the difference between Syn10 and Syn15 is unknown. One possibility is aging time: Syn10 was prepared first, and it is possible that Syn15 would, upon aging, resemble Syn10. However, the time series data for Syn15 does not support this hypothesis. After aging for up to 8 months, the basic aggregate structure of Syn15 seems to remain stable, only average aggregate size appears to increase. Thermal treatment of Syn15 also caused very little quantifiable change in aggregate structure. Instead, it seems that Syn10 and Syn15 were set on different aggregation trajectories very early in the aggregation process, perhaps due to a subtle variation in solution chemistry, or due to features inherited from synthesis such as detailed particle morphology. The precise difference between these syntheses is unknown, and additional experiments using this synthesis have shown an even greater range of aggregate structures than reported here (discussed in Chapter 3).

The structures of both Syn10 and Syn15 differ significantly those predicted by traditional models of aggregation. The commonly assumed DLCA mechanism, in which fractal structures arise to due stochastic collisions between clusters and hard spheres, is expected to produce aggregate fractal dimensions between 1.6 and 1.9.[28] Of course, DLCA is expected to be rapid, and is unlikely to control the development of aggregates which grow slowly over the course of months, as was observed for Syn15. In these cases, an RLCA mechanism is more likely to apply. Simple models for RLCA generally predict the formation of more densely packed aggregates, with fractal dimension of greater than 2. The low dimension of the branched fractal aggregates seen in this study are not fully explained by either the DLCA or the RLCA based mechanism.

The aggregate structures may be influenced by "long" distance interparticle forces, such those predicted by DLVO theory for electrostatic repulsion in a dilute electrolyte solution. These forces typically extend for tens of nanometers. Over the length scales probed, these may limit the trajectories for particle attachment and/or stabilize the aggregates against collapse. Alternatively, short-range crystallographically direction-specific interactions could favor the formation of nanoparticles chains. Such oriented aggregation effects have been known to lead to crystal growth under some conditions.[19] The formation of single crystal laths in Syn10 (which also has very linear chains) seems to support this later hypothesis. In any case, if the low fractal dimension is controlled by relatively local interactions, very large aggregates are likely to possess more traditional aggregate morphologies when observed on macroscopic length scales.

The low observed fractal dimensions have directly observable physical consequences. Historically, local aggregate structure was not directly observable, and fractal geometries have provided a useful tool for modeling the local structure, so that physical properties can be estimated. Fractal structure has been correlated with aggregate mechanical strength, hydrodynamic behavior, transport, and persistence in the environment.[22] For example, aggregates with low fractal dimension are less susceptible to gravitational settling.[23] This can be directly used, to explain how ferrihydrite suspensions can be extensively aggregated, and yet remain stable against sedimentation. It can also be shown that the lower fractal dimensions leads to suspensions that are more optically transparent. Of course, these correlations of physical behavior with fractal dimension often reflect an underlying assumption that fractal dimension provides a measure of aggregate density and branching. In the future, direct measurement of aggregate structures may provide a method for direct computation of these properties.

2.6 Conclusions

The tomographic methods described in this dissertation have been used for the first time to directly determine the three-dimensional structure of fragile, nanoparticle aggregates *in aqua*. This has allowed a direct estimation of the fractal dimension of these aggregates. On length scales up 100 nm, the aggregates are dominated by linear structures, characterized by low fractal dimension. These structures are not predicted by traditional models of stochastic colloidal aggregation. This finding should have important ramifications for nanoparticle behavior, since fractal dimension can impact aggregate stability, flocculation rates, and transport behavior.

The introduction of cryo-tomography, especially using approaches that can be quantitatively integrated with SAXS, should prove invaluable for exploring complex and highly polydisperse aggregate suspensions whose characterization has previously been intractable.

2.7 Supplemental

2.7.1 Data

Figure 8 is an example of the power law fits, which are used to extract fractal dimension, showing all of the autocorrelation functions obtained from a single tomogram, with each curve representing a distinct subvolume.
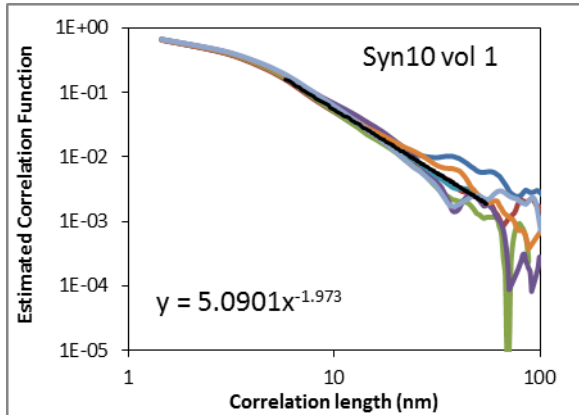

Figure 8: Autocorrelation functions esimtated from Syn10 vol 1, using Equation 11. Each curve corresponds to a separate subvolume. The best average fit to the fractal region, shown by the black line, has a power law exponent of -1.973, which corresponds to a fractal dimension of 1.03.

Figure 9 and Figure 10 show two different tomograms obtained for Syn10, and demonstrate how the tomograms are divided into subvolumes for the purposes of processing. These examples demonstrate that not all subvolumes are evenly filled, thus a subvolume such as S15 (from Figure 9 (A) was not used for analysis, but the other volumes were.
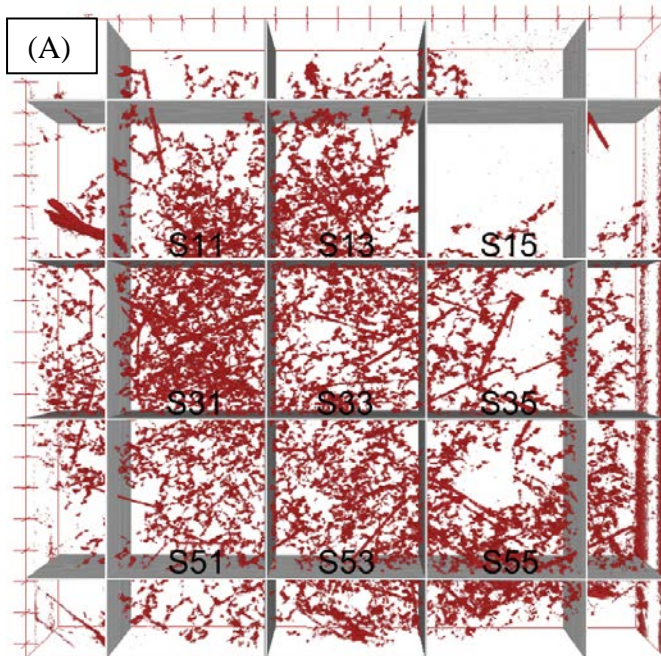
Figure 9: Syn10 vol 2 segmented tomogram, with subvolumes S11 through S55 designated and labeled. During data acquisition, initial pixel size is 0.5423 nm. Each subvolume is a cube, 278 nm edge length. After downsampling for autocorrelation function analysis, each subvolume is a 128x128x128 voxel cube. This sample contained extremely thin ice, and does not completely fill the subvolume in the directions into and out of the page.
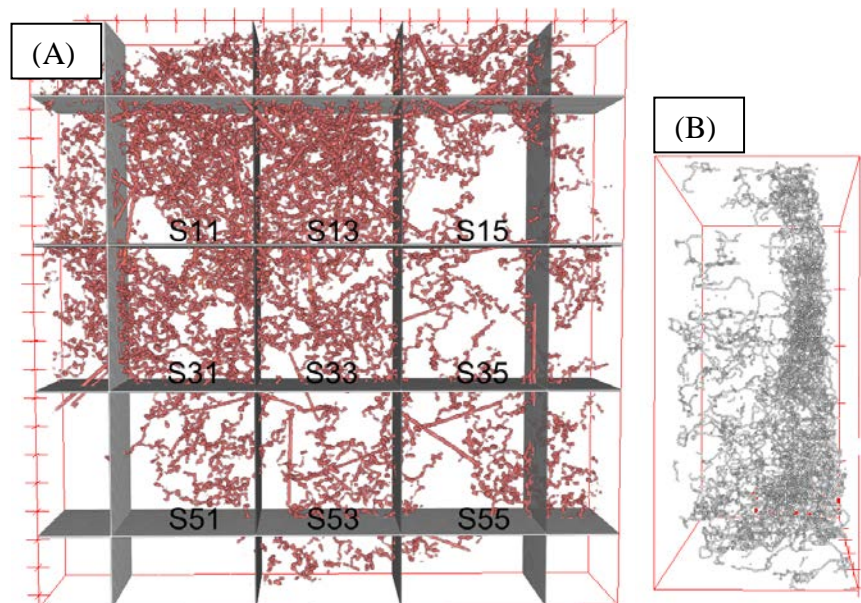

Figure 10: (A) Tomographic reconstruction of Syn10 vol3, showing the subsections that were used for tomographic analysis. (B) Side view of section S11, skeletonized for visual clarity. Note that the ice here is thin, and a thick surface layer of nanoparticles has formed on one of the ice surfaces (right hand size of the image).

Figure 10 , in particular, shows a wide range of structures and particle densities. Sections S11, S13, and S31 all show higher than average particle densities and significant surface reconstruction. These volumes had fractal dimensions (estimated using Equation 11) of 1.9, 1.4, and 1.7, respectively. These values are higher than average for Syn10. However, particle packing density is not the only factor determine fractal dimension, for example, S13 has a higher particle density than S31, but a lower fractal dimension. Close analysis reveals that the distribution of particles within the volume is critical. Examination of volume S11 shows that over half of the particles have accumulated in a dense interfacial layer, as shown in Figure 10 (B). This explains the apparently high (2-dimensional) fractal dimension estimated for that volume, because the dense interfacial layer is, in essence, a two-dimensional object.

Structures with lower particle density do have a tendency toward lower fractal dimension. In fact, S35 and S53 show low fractal dimensions of 1.25 and 0.83, respectively. Close inspection of these volumes shows very similar structures. The very low estimated value for S53 should be regarded as a statistical fluctuation in the local correlation function due to finite sampling size.
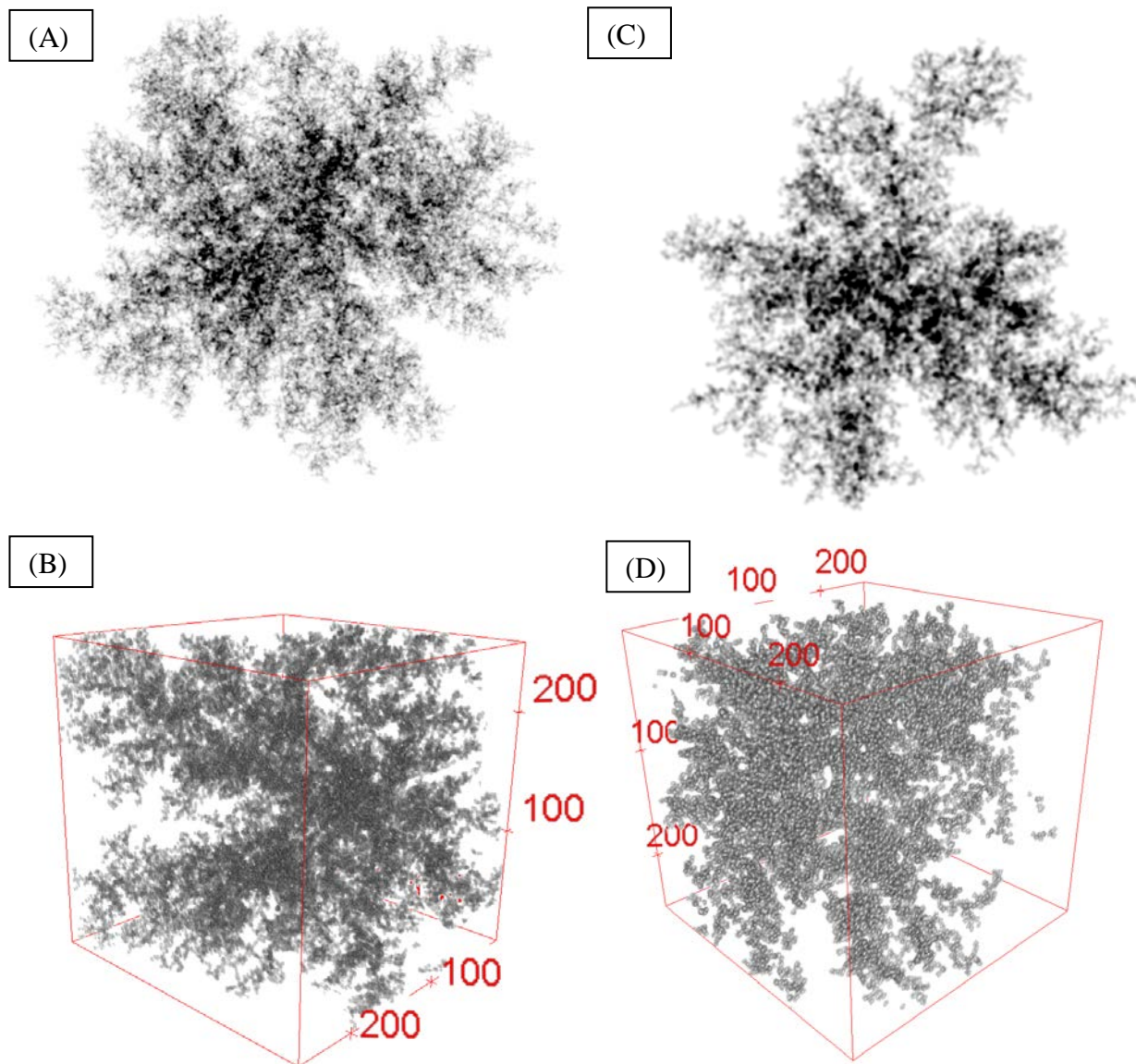
Figure 11: (A) Projection view of a computationally generated DLA based aggregated containing 100,000 particles. **(B)** 3D volume extracted from the center of this aggregate, for use in calibrating the fractal dimension analysis. Volume is 256x256x256 voxels. **(C)** Projection view of a computationally generated DLA based aggregated containing just 20,000 particles, the image is scaled by maximum particle extent, so individual particles appear larger. **(D)** 3D volume extracted from the center of this aggregate.

In order to "calibrate" the autocorrelation function based approach, computationally generated aggregates were also analyzed. Ten aggregates were generated using the DLA-nd computer program. Five aggregates contained 20,000 particles, five aggregates contained 100,000 particles. The central portion of the aggregate was extracted into a three-dimensional volume for processing. Samples are provided in Figure 11.

2.8 Acknowledgements

2.9 Works Cited

1. Liu, J.; Aruguete, D. M.; Murayama, M.; Hochella, M. F. Influence of Size and Aggregation on the Reactivity of an Environmentally and Industrially Relevant Nanomaterial (PbS). *Environ. Sci. Technol.* **2009**, *43*, 8178–8183.
2. Dunphy Guzman, K. A.; Finnegan, M. P.; Banfield, J. F. Influence of Surface Potential on Aggregation and Transport of Titania Nanoparticles. *Environ. Sci. Technol.* **2006**, *40*, 7688–7693.
3. Gilbert, B.; Ono, R. K.; Ching, K. A.; Kim, C. S. The Effects of Nanoparticle Aggregation Processes on Aggregate Structure and Metal Uptake. *J. Colloid Interface Sci.* **2009**, *339*, 285–295.
4. Adrian, M.; Dubochet, J.; Lepault, J.; McDowall, A. W. Cryo-electron Microscopy of Viruses. *Nature* **1984**, *308*, 32–36.
5. Pouget, E. M.; Bomans, P. H. H.; Goos, J. A. C. M.; Frederik, P. M.; de With, G.; Sommerdijk, N. A. J. M. The Initial Stages of Template-Controlled $CaCO_3$ Formation Revealed by Cryo-TEM. *Science* **2009**, *323*, 1455–1458.
6. Yuwono, V. M.; Burrows, N. D.; Soltis, J. A.; Penn, R. L. Oriented Aggregation: Formation and Transformation of Mesocrystal Intermediates Revealed. *J. Am. Chem. Soc.* **2010**, *132*, 2163–2165.
7. Midgley, P. A.; Dunin-Borkowski, R. E. Electron Tomography and Holography in Materials Science. *Nat. Mater.* **2009**, *8*, 271–280.
8. Meakin, P. Aggregation Kinetics. *Phys. Scr.* **1992**, *46*, 295-331.
9. Sinha, S. K. Scattering from Fractal Structures. *Physica D* **1989**, *38*, 310–314.
10. Manceau, A. Critical Evaluation of the Revised Akdalaite Model for Ferrihydrite. *Am. Mineral.* **2011**, *96*, 521-533.
11. Gilbert, B.; Erbs, J.J.; Penn, R.L.; Petkov, V.; Spagnoli, D.; Waychunas, G.A. A Disordered Nanoparticle Model for 6-Line Ferrihydrite. *Am. Mineral.* **2013**, *98,* 1465-1476.
12. Lovley, D. R.; Holmes, D. E.; Nevin, K. P. Dissimilatory Fe(III) and Mn(IV) Reduction. In *Advances in Microbial Physiology*; Academic Press: New York, 2004; Vol. Volume 49, pp. 219–286.
13. Gilbert, B.; Lu, G.; Kim, C. S. Stable Cluster Formation in Aqueous Suspensions of Iron Oxyhydroxide Nanoparticles. *J. Colloid Interface Sci.* **2007**, *313*, 152–159.
14. Guyodo, Y.; Mostrom, A.; Lee Penn, R.; Banerjee, S. K. From Nanodots to Nanorods: Oriented Aggregation and Magnetic Evolution of Nanocrystalline Goethite. *Geophys. Res. Lett.* **2003**, *30*, 1512 1-4.
15. Kremer, J. R.; Mastronarde, D. N.; McIntosh, J. R. Computer Visualization of Three-Dimensional Image Data Using IMOD. *J. Struct. Biol.* **1996**, *116*, 71–76.
16. Agulleiro, J. I.; Fernandez, J. J. Fast Tomographic Reconstruction on Multicore Computers. *Bioinformatics* **2011**, *27*, 582–583.

17. Kaynig, V.; Fuchs, T.; Buhmann, J. M. Neuron Geometry Extraction by Perceptual Grouping in ssTEM Images. In *2010 IEEE Conference on Computer Vision and Pattern Recognition (CVPR)*; **2010**; pp. 2902–2909.

18. Ilavsky, J.; Jemian, P. R. *Irena* : Tool Suite for Modeling and Analysis of Small-Angle Scattering. *J. Appl. Crystallogr.* **2009**, *42*, 347–353.

19. Burleson, D. J.; Penn, R. L. Two-Step Growth of Goethite from Ferrihydrite. *Langmuir* **2006**, *22*, 402–409.

20. Teixeira, J. Small-Angle Scattering by Fractal Systems. *J. Appl. Crystallogr.* **1988**, *21*, 781–785.

21. Nicolai, T.; Durand, D.; Gimel, J.-C. Static Structure Factor of Dilute Solutions of Polydisperse Fractal Aggregates. *Phys. Rev. B* **1994**, *50*, 16357–16363.

22. Manley, S.; Cipelletti, L.; Trappe, V.; Bailey, A. E.; Christianson, R. J.; Gasser, U.; Prasad, V.; Segre, P. N.; Doherty, M. P.; Sankaran, S.; Jankovsky, A. L.; Shiley, B.; Bowen, J.; Eggers, J.; Kurta, C.; Lorik, T.; Weitz, D. A. Limits to Gelation in Colloidal Aggregation. *Phys. Rev. Lett.* **2004**, *93*, 108302.

23. Gmachowski, L. Aggregate Structure and Hydrodynamics of Aggregated Systems. *Colloids Surf., A* **2005**, *255*, 105–110.

24. Sposito, G. *The Surface Chemistry of Natural Particles*. Oxford University Press: Oxford, 2004.

25. Gmachowski, L. Calculation of the Fractal Dimension of Aggregates. *Colloids Surf., A* **2002**, *211*, 197–203.

26. Bushell, G. C.; Yan, Y. D.; Woodfield, D.; Raper, J.; Amal, R. On Techniques for the Measurement of the Mass Fractal Dimension of Aggregates. *Adv. Colloid Interface Sci.* **2002**, *95*, 1–50.

27. Dimon, P.; Sinha, S. K.; Weitz, D. A.; Safinya, C. R.; Smith, G. S.; Varady, W. A.; Lindsay, H. M. Structure of Aggregated Gold Colloids. *Phys. Rev. Lett.* **1986**, *57*, 595-598.

28. Porod, G. In *Small Angle X-Ray Scattering*; Glatter, O., Kratky, O., Eds.; Academic Press: London, 1982; pp. 18-59.

29. Sposito, G. Scaling Invariance of the von Smoluchowski Rate Law. *Colloids Surf., A* **1997**, *120*, 101–110.

30. Lin, M. .; Klein, R.; Lindsay, H. .; Weitz, D. .; Ball, R. .; Meakin, P. The Structure of Fractal Colloidal Aggregates of Finite Extent. *Colloids Surf. A* **1990**, *137*, 263–280.

31. Yanwei, Z.; Meriani, S. Scaling Functions for the Finite-size Effect in Fractal Aggregates. *J. Appl. Crystallogr.* **1994**, *27*, 782–790.

32. Oliphant, T. E. Python for Scientific Computing. *Comput. Sci. Eng.* **2007**, *9*, 10-20.

Chapter 3: Impacts of Ionic Strength on the Three-dimensional Nanoparticle Aggregate Structure and Consequences for Environmental Transport and Deposition.

The transport of nanoparticles through aqueous systems is a complex process with important environmental policy ramifications. Ferrihydrite nanoparticles commonly exist in an aggregated state, with structures that may depend on solution chemistry. The impact of aggregation state on transport and deposition is not fully understood. In this study, small angle x-ray scattering (SAXS) and cryogenic transmission electron microscopy (cryo-TEM) were used to directly observe the aggregate structure of ferrihydrite nanoparticles and show how the aggregate structure responds to changing ionic strength. These results are correlated with complimentary studies on ferrihydrite transport through saturated quartz sand columns. With deionized water eluent, nanoparticles form stable, low-density fractal aggregate structures. These structures appear to be resistant to collapse and the particles show limited deposition on sand grain surfaces. In the presence of sodium nitrate aqueous solutions, the aggregates collapse into dense clusters. This is accompanied by greatly increased nanoparticle deposition, forming thick, localized, and mechanically unstable deposits. The formation of such deposits limits nanoparticle transport, and may impact strategies for monitoring and controlling nanoparticle fate within the environment.

3.1 Introduction

The transport of nanoparticles through aqueous systems is a complex, yet environmentally important process. Nanoparticles are recognized as class of emerging contaminants with the potential for high mobility in environmental systems via colloidal transport.[1] This study considers the relationship between nanoparticle aggregate structure and their transport through saturated media, focusing on the behavior of ferrihydrite (ferric oxyhydroxide) nanoparticle aggregates.

Ferric oxides and oxyhydroxides occur naturally as nanoparticles in the environment, where they may be geochemically reactive and biologically available. A variety of iron reducing bacteria utilize ferrihydrite nanoparticles as electron acceptors in their metabolism and also have the capability to metabolize environmental contaminants such as uranium.[2,3] This makes iron oxyhydroxide particles a potential tool for manipulating microbial communities in bioremediation strategies. Furthermore, iron oxyhydroxides have been identified as important vectors for the transport of heavy metals such as arsenic and lead[4,5], as well as radionuclides such as plutonium and arsenic.[6] These containments may be incorporated into the nanoparticle structure or adsorbed on their surfaces.

Recent work has shown that stable aqueous suspensions of ferrihydrite nanoparticles may consist of complex, highly aggregated structures. These aggregate structures are diverse, and may

include rods, fractal aggregates, and clusters.[7,8] By combining *in situ* small angle x-ray scattering (SAXS) and cryogenic transmission electron microscopy (cryo-TEM), it has been shown that aggregates may be large (microns in extent) but that they possess very low fractal dimensions (see Chapter 2). The result is a low density aggregate that can remain in suspension without displaying the behaviors that are typically associated with aggregation such as flocculation, light scattering, and sedimentation (see Chapter 2).

The presence of stable aggregates may have profound impact on the transport, fate, and reactivity of nanoparticles.[9,10,11] Models for colloidal transport are now quite sophisticated, and several comprehensive review articles are available.[12,13,14,15] However, most traditional models for colloidal transport are based upon the interaction between free particles and substrate surfaces. Transport is assumed to be limited by particle deposition, and the causes of deposition are broadly classified as pore straining, sedimentation, and collision with substrate surfaces. These processes have been modeled quantitatively for single particles, with emphasis placed on the ways that electrostatic interactions between particles and substrate surfaces modulate the attachment probability. Many researchers have also considered the importance of aggregate structure, since this has obvious ramifications for colloid straining and settling. However, quantitative models for aggregate deposition are not well developed, and it is likely that low density fractal aggregates will behave vary differently from single particles or compact aggregates when they interact with substrate surfaces.

The behavior of ferrihydrite nanoparticle aggregates with low fractal dimension is of special interest here. Although traditional models for colloidal aggregation predict the formation of fractal structures,[17] they do not explain the formation of aggregates with very low fractal dimension and the precise physics which stabilize these aggregate structures are unknown (see Chapter 2). Since fractal dimension is known to correlate with aggregate density and hydrodynamics,[18,19] unique transport behavior may exist in these nanoparticle systems. Furthermore, the physical processes which stabilize low fractal dimension aggregates are unknown. It has been suggested that electrostatic interactions may stabilize such aggregates against collapse, and it is likely that the levels of electrolytes encountered in environmental settings may be sufficient to screen these electrostatic forces and trigger aggregate reconstruction. Previous studies have been performed on ferrihydrite transport and have shown transport behavior that depends on ionic strength,[4,16] but ferrihydrite particles come in diverse sizes and shapes, and the influence of aggregate structure on transport/deposition is currently unknown.

In this study, the influence of ionic strength on aggregate structure is addressed, with a focus on the behavior of aggregates with an initially low fractal dimension. Sodium nitrate solutions serve as an indifferent electrolyte that can influence electrostatic interactions via charge screening, but nitrate it is not expected to undergo significant specific adsorption on the iron oxyhydroxide surface. The response to changes in ionic strength is characterized by a combination of *in situ* SAXS and cryo-TEM based experiments. A series of complimentary experiments is performed

to determine how ferrihydrite nanoparticles deposit in a saturated packed sand column, using a pulsed injection of nanoparticles into columns where the background eluent is held at various constant ionic strengths. Correlations between the aggregate structure and the deposition behavior are discussed.

3.2 Experiment

Four 35 mL suspensions of iron oxyhydroxide nanoparticles were formed via microwave flash precipitation from ferric nitrate, as described by Guyodo.[8] After precipitation, the suspension ionic strength was adjusted by dialysis against 18 MΩ water, to a final conductivity of <200 µS/cm, and pH of approximately 4.5, and no greater than 5 (note that suspension was not buffered). X-ray diffraction confirms 6-line ferrihydrite phase for the particles. The resulting nanoparticles are 3-4 nm in diameter, and the nanoparticle mass fraction is approximately 3.5 mg/mL. When stored at 4 °C, these suspensions are stable against flocculation and aggregate structural reconstruction for several months.

The aggregate structure and transport behavior of four different samples were analyzed: Syn10, Syn12, Syn15, and Syn16. Syn10 was analyzed with TEM, SAXS, and transport experiments. Syn12 was analyzed more comprehensively with SAXS and transport experiments, but with more limited TEM characterization. Syn15 and Syn16 were analyzed comprehensively with SAXS and TEM, without transport experiments. Detailed tomographic structural analysis for Syn10 and Syn15 has been previously discussed in Chapter 2. Each of these samples were prepared by identical experimental protocols and all possess low dimensional fractal aggregate structures, however, there are subtle differences between these samples with respect to primary particle size, aggregation state, pH, and conductivity. Syn15 and Syn16 were prepared on the same day, and are essentially identical to each other, while Syn12 and Syn10 were prepared on an earlier date, and are slightly different. The initial extent of aggregation in Syn15 and Syn16 is less than that of Syn10 and Syn12. Syn12 is more sensitive to changes in electrolyte concentration than Syn10. The reason for these slight initial differences in aggregate structure between synthesis is unknown. More precise control of particle aggregate structure likely requires better control of pH, but this is difficult to achieve, since the use of pH buffers will contribute electrolytes to the solution.

3.2.1 Characterizing Aggregate Structure

Prior to structural characterization, the ionic strength of the ferrihydrite suspension is adjusted by adding 150 µL of the dialyzed suspension into a diluting solution of $NaNO_3$ to obtain a final volume of 1.5 mL. The $NaNO_3$ concentration of the diluting solutions ranged from 0 to 50 mM.

Cryo-TEM samples were prepared by applying a 2-3 µL drop of the diluted ferrihydrite suspension onto a carbon-coated lacey Formvar TEM grid (Ted-Pella, P.N. 881F). Prior to application, grids were made hydrophilic by plasma discharge and rinsed with a $NaNO_3$ solution with concentration matching that of the sample to optimize sample-grid interactions. For selected datasets, 1 µL of 10 nm citrate capped gold colloid (BBInternational) was pre-applied to the grid

and allowed to dry before sample application; these particles serve as fiducial markers for image registration during tomographic image processing (see tomographic datasets in Chapter 2).

Excess suspension was removed by blotting with cellulose filter paper, to leave a thin film (~100-300 nm thick) of suspension on the lacey grid. The grid was plunged into liquid ethane at −180 °C, quenching rapidly enough to produce a vitreous (glassy) ice, with the aggregate structure preserved intact. This allows the aggregate structure to be imaged directly in TEM using a cryo-chilled (-180 °C) stage. Cryo-TEM is performed using either a 200 keV Phillips CM200, or an energy filtered 300 keV JEOL3100.

SAXS studies were performed at Lawrence Berkeley National Labs, Advanced Light Source, beamline 7.3.3. SAXS was obtained with a 10 keV beam in transmission mode, with a Pilatus 1M detector. Sample cuvettes are approximately 1-2 mm thick. Scattering path lengths was calibrated with a silver behenate standard. Usable scattering ranges of $q = 0.008$ Å^{-1} to 0.21 Å^{-1} were obtained.

At the beginning of experiments, the environmental factors that controlled aggregate reconstruction were unknown. A sample matrix of over 250 SAXS samples were prepared, to test the influence of sample storage at room temperature vs. storage at elevated temperature (35 °C to 55 °C, for up to one week), the influence of sodium nitrate concentration, and the time period of exposure to salt solution (from 1 hour to 1 month). The suspensions were saved for one year after the experiment, in order to evaluate the long term aggregate stability vs. flocculation.

3.2.2 Characterizing Transport

Nanoparticle transport through porous saturated media is analyzed using a packed column of Ottawa quartz sand. Sand is wet-packed into the column and agitated until settled. Additional sand is added as necessary to minimize head-space. The column was characterized using micro-tomography beamline 8.3.2 at the Advanced Light Source (ALS). The resulting tomogram, shown in Figure 4, is used to characterize sand packing within the column. Column length is 10 cm and column inner diameter is 1 cm. Maximum sand grain size is less than 1 mm. Based upon tomographic analysis, column porosity is 33% and specific surface area is 210 cm^{-1}.
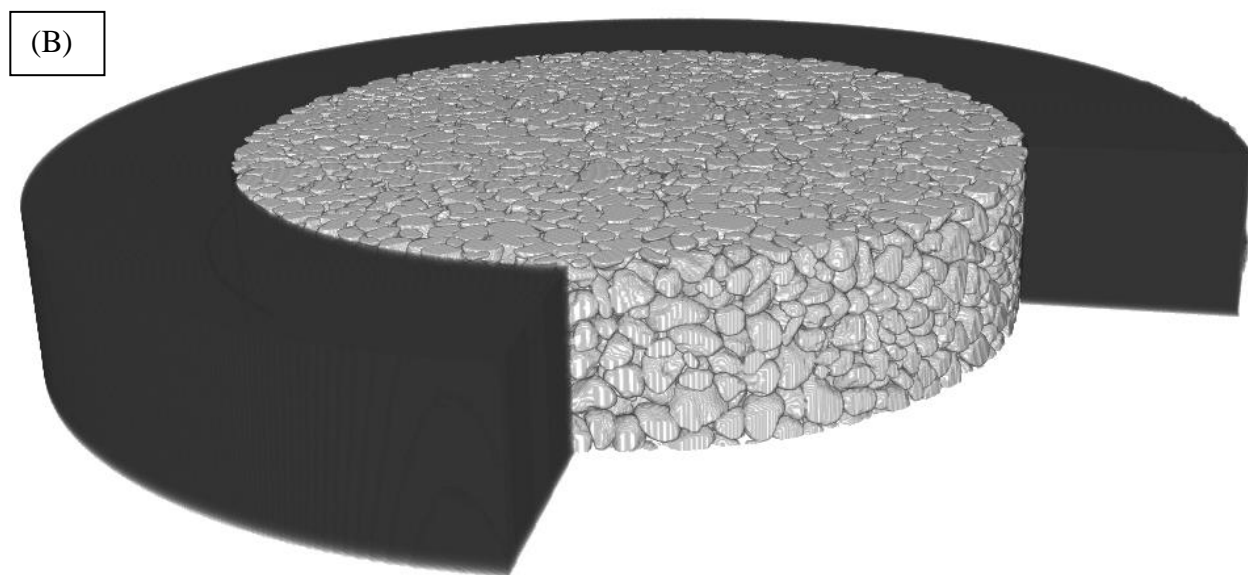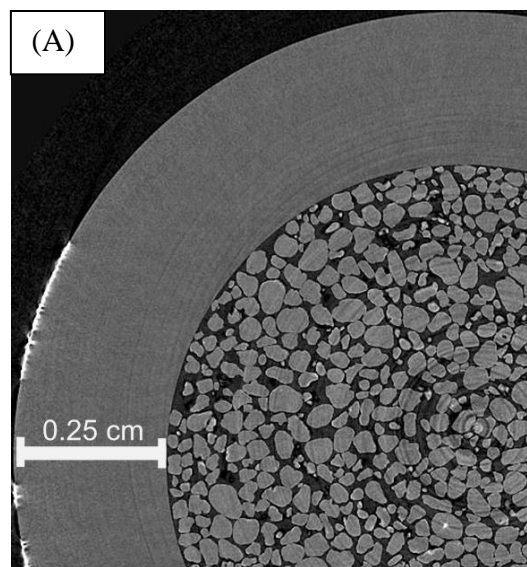
Figure 1: (A) Cross section view of sand column, obtained by x-ray tomography. Light colors correspond to higher x-ray adsorption. Dark grey corresponds to air/pore space. (B) Perspective view of sand column with cutaway to reveal sand packing structure. Data obtained at beamline 8.3.2

Prior to each experiment, the column is cleaned of residual iron oxides using a 0.1 M oxalic acid solution, and flushed with > 5 pore volumes of eluent. Each experiment is run using a mobile phase (eluent) of either deionized water, 2 mM, 4 mM, or 10 mM $NaNO_3$ solution. Flow speed is held constant at either 0.05 mL/min (~0.1 cm/min) or 0.1 mL/min (~0.2 cm/min) using a Jasco PU 2085 HPLC pump. 100 µL pluses of concentrated nanoparticles suspensions are injected into the column using a VICI Valco 6-way valve. Nanoparticle concentration at the column outflow is continuously monitored by optical absorption at a wavelength of 518 nm, using a quartz flow-through cuvette (path length 10 mm, chamber volume 80 µL). Absorption at this wavelength is proportional to nanoparticle concentration and independent of ionic strength. The optical

34

adsorption curves for each pulse are integrated over time to determine the quantity of nanoparticles that pass through the column and the fraction of nanoparticles deposited within the column is estimated by subtracting the quantity passed from the quantity of particles injected.

Nanoparticle deposition is modeled based on a simple deep bed filtration model that has been adapted from Tien and Payatakes.[22] The column is treated as a series of 100 unit bed elements, each with length, $l = 0.1$ cm and volume, $V = 0.079$ cm^3. When a pulse of particles passes through an element, a fraction of the particles is deposited, while the remaining particles continue to pass through the column. The fraction of particles deposited in each element is that element's collection efficiency, defined as $\eta = (m_{in} - m_{out})/m_{in}$, where m_{in} and m_{out} are the masses of particles which enter and leave the element, respectively. Collection efficiency may change as particles accumulate. The quantity of particles that an element has accumulated is equal to the element volume times its "specific deposit", σ, which has dimensions of particle mass per volume. On the basis of mass balance, it is also possible to describe the collection efficiency in terms of accumulated particles (the change in specific deposit).

Equation 1

$$\eta = V(\Delta\sigma)/m_{in}$$

Here, $\Delta\sigma$ represent the change in specific deposit within an element, after a pulse that carries an initial mass of m_{in} passes through the element. The value of η is somewhat arbitrary, as it depends upon how the column is modeled (the volume of the elements). The more fundamental parameter for describing column physics is the filter coefficient, λ, which has dimensions of inverse length and is related to the collection efficiency as follows:

Equation 2

$$\eta = 1 - \exp(-\lambda l)$$

Here, l represents the length of the unit element. The filter coefficient may depend upon flow velocity and solution chemistry, and will change over time as particles accumulate. Typical columns can only accumulate a finite amount of particles per unit volume, this corresponds to the "ultimate specific deposit" parameter, σ_{max}. In this study, the filter coefficient of an element is assumed to decrease linearly from a value of λ_0 when the element is clean, to a value of 0 when σ has reached a value of σ_{max}. Thus, $\lambda = \lambda_0(1 - \sigma/\sigma_{max})$. Although physically simple, it will be shown that this behavior does not hold for all experimental conditions. Continuing with this assumption, the change in an element's specific deposit, upon a small injection of particles is given as:

Equation 3

$$\frac{d\sigma}{dm} = \frac{\eta}{V} = \frac{1}{V}\left[1 - e^{-\lambda_0\left(1 - \frac{\sigma}{\sigma_{max}}\right)}\right]$$

When very large pulses of particles pass through a unit bed element, the first particles in the pulse will encounter a cleaner bed than the last particles in the pulse. For large pulses, the average collection efficiency of an element is obtained by separation of variables and integration. The result is Equation 4, which relates the final specific deposit after a pulse, σ_f, to the initial size of the pulse, m_{in}, the clean bed filter coefficient, λ_0, the ultimate specific deposit, σ_{max}, and any preexisting specific deposit, σ_i.

Equation 4

$$\left(1 - \frac{\sigma_f}{\sigma_{max}}\right) = \frac{1}{\lambda_0 l} \ln\left(1 - e^{-\frac{m_{in}\lambda_0 l}{V\sigma_{max}}}\left(1 - e^{-\lambda_0 l(1-\frac{\sigma_i}{\sigma_{max}})}\right)\right)$$

This can be compared with Equation 2 to obtain an expression for η, which is a function of the element's starting condition, and the mass of particles injected.

Equation 5

$$\eta = \frac{V}{m_{in}}\left\{\sigma_i - \sigma_{max} + \frac{\sigma_{max}}{\lambda_0 l}\ln\left(1 - e^{-\frac{m_{in}\lambda_0 l}{V\sigma_{max}}}\left[1 - e^{-\lambda_0 l\left(1-\frac{\sigma_i}{\sigma_{max}}\right)}\right]\right)\right\}$$

A simple model is then constructed, that treats the column as a series of 100 unit bed elements. With this model, one can calculate the fraction of nanoparticles deposited within each element as a pulse passes through the column. The total fraction of nanoparticles that successfully pass through the column can also be determined and compared with experiment. As more pulses pass through the column, elements will become saturated, and the fraction of particles eluted is expected to increase. The value of σ_{max} can be directly obtained from experimental data by calculating the total mass of particles that have been deposited within the column when saturation is reached, and then dividing by the total column volume. The value of λ_0 determines how rapidly saturation is approached. For high values of λ_0, the early particle pulses will have high deposition efficiency and saturation is reached quickly, but when λ_0 is low, more of the early particles will be able to pass through the column and deposits will accumulate more gradually. The value of λ_0 is estimated using a numerical least-squares algorithm, that compares the experimentally observed elution fractions for a series of pulses with numerical predictions.

3.3 Results

3.3.1 Aggregate Structure
Cryo-TEM results for all four syntheses in deionized water show nanoparticles that are between 2 to 4 nm in diameter, and are aggregated into extensive networks. These suspensions are also optically clear and unsedimented, and remain stable as such indefinitely. It is apparent that these aggregates have a very open, low density structure. There is a tendency to form linear particle chains, and in some cases, these chains transform into lathe-shaped particles over time. Other researchers studying similarly synthesized particles have determined that such transformations

36

occur via oriented aggregation.[49] Of these syntheses, only Syn10 shows extensive lathe formation, although Syn12 shows small amounts of lathes.

Images of the aggregate structures in deionized water are provided in Figure 2. Syn10 and Syn12 both show highly linear, low density aggregate structures, which can be of very large extent (exceeding several microns). Although small regions of dense packing can be found, as shown in Figure 2 (B), the open, linear structures dominate. Syn15 differs, in that the average aggregate size is significantly smaller, and many of the aggregates appear to be more densely packed. Additional images of Syn10 and Syn15 in deionized water are provided in Chapter 2.

In generally, the aggregates show limited interaction with the carbon support grids, which are visible in Figure 2 (A), (C), and (D). It is obvious that particles attach to the support grid surface, but they do so in a limited fashion.
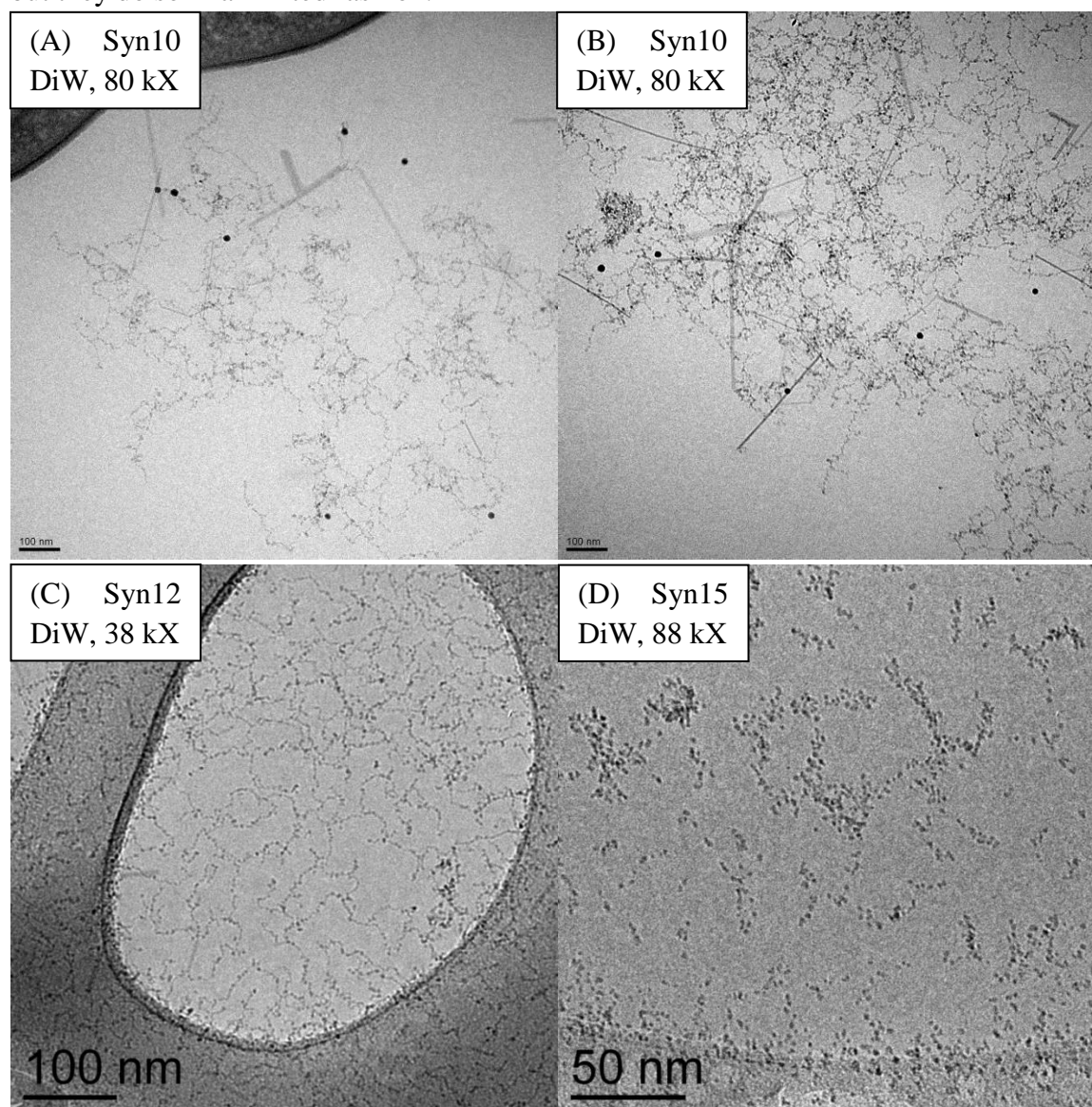

Figure 2: Cryo-TEM images of ferrihydrite nanoparticles in deionized water suspensions.

Upon introduction to a 20 mM NaNO$_3$ salt solution, the nanoparticle aggregates show identical primary particle size and shape, but a large percentage of the aggregates have apparently collapsed to become densely packed. Two selected images are shown in Figure 3. Very large aggregate clusters are observed, even for Syn15, where the aggregate size in deionized water was quite small. Perhaps more importantly, large regions of these aggregates have collapsed to become densely packed. The linear, low fractal dimension aggregate motif is still present in some areas, for example in the inset shown in Figure 3 (A), and at the edge of the large aggregates shown in Figure 3 (B), but larger, denser structures dominate these samples.
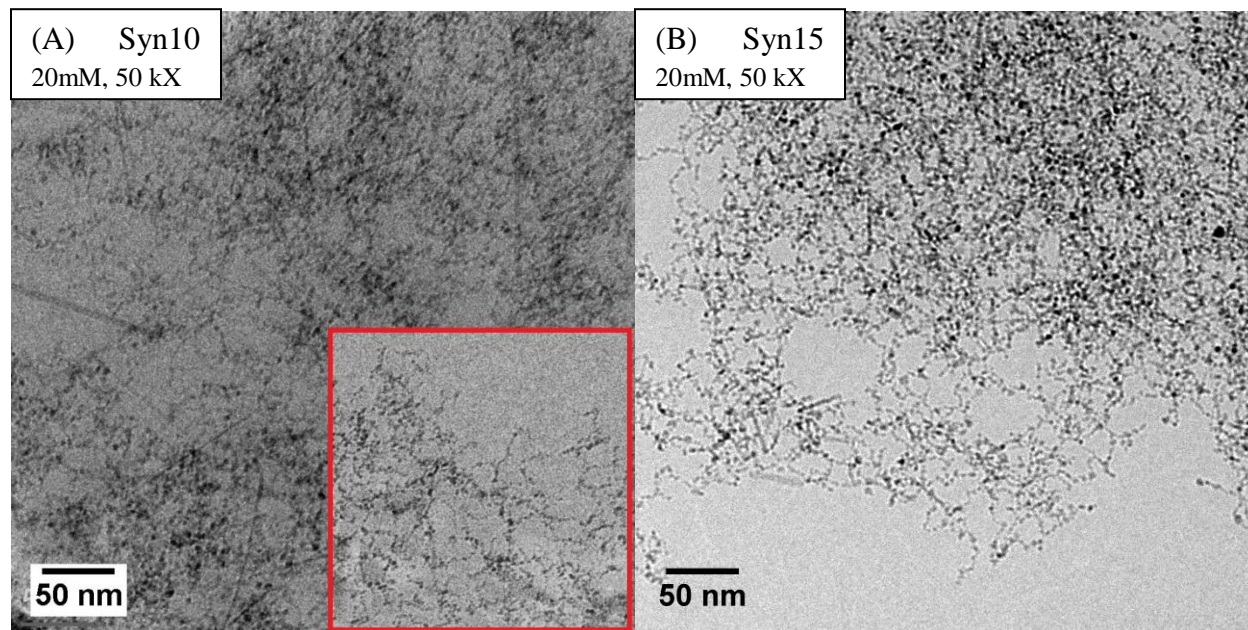

Figure 3: Cryo-TEM images of ferrihydrite nanoparticles suspended in 20 mM NaNO$_3$ solutions, both obtained at 50 kX using CM200. (A) Syn10. Inset is from the same sample, but shows the edge of a large aggregate where the open fractal structure is still visible (B) Syn15, this image focuses on the edge of a large aggregate. Both samples show the tendency for densely aggregated structures, in the presence of 20 mM NaNO$_3$. Image quality in (A) is lower than in (B), due to variations in ice thickness and quality of the sample vitrification process.

SAXS studies were performed in an effort to quantify the impact of aggregate storage temperature, aging time, and ionic strength on aggregate structure. After analyzing the results, that SAXS measurements were found to have too much statistical variation to fully characterize each of these variables. Storage time and temperature were found to have essentially no quantifiable effect on aggregate structure, while ionic strength showed significant impact on aggregate structure, irrespective of the other variables. We thus focus on ionic strength alone as the primary variable controlling aggregate structure.

Figure 4 displays SAXS scattering curves from samples of Syn12, Syn15, and Syn16, where the curves have been grouped with respect to ionic strength. In higher ionic strength solutions, the SAXS patterns tend to show greater scattering at low angles (low q values). This increase in low-q scattering reflects either an increase in the overall aggregate size or the collapse of aggregates to form denser structures. It is also obvious that there is a high amount of statistical variation

between SAXS samples. This variability appears to be inherent to the samples being studied, and is present even when comparing samples with identical preparation (the variation is not primarily due to aging time or temperature). As discussed in Chapter 2, aggregate size distributions frequently possess "long tails", where a large fraction of particles are associated with a few very large aggregates. The shape of the scattering curve may vary widely, depending on whether or not the sample volume contains one or more of these very large aggregates.

The apparent fractal dimension, d_f, has been used to quantify the differences between samples. This measurement is obtained from SAXS according the relationship

Equation 6

$$d_f = -\frac{d \log(I)}{d \log(q)}$$

This value is obtained by a linear regression of the log-log SAXS intensity plot, over the q range of 0.008 to 0.025 Å^{-1}. This corresponds to an approximate length scale of 25 to 80 nm. It is important to stress that this measurement should only be treated as an *apparent* fractal dimension, should *not* be interpreted as a true structural fractal dimension. As discussed in Chapter 2, apparent fractal dimensions may differ from the true structural fractal dimension when the suspension contains a wide range of aggregate sizes. Our cryo-TEM results show certain suspensions (Syn15 and Syn16) possess a wide range of aggregate sizes. This aggregate polydispersity will result in apparent fractal dimensions that are lower than the true structural fractal dimension. Furthermore, our results show that the suspensions contain mixtures of different aggregate morphologies, where dense collapsed aggregates that possess a high structural fractal dimension coexist with low density aggregates that possess an open structure and low structural fractal dimension. A single fractal dimension parameter will not be sufficient to fully describe such complex systems. Nevertheless, this approach does provide a method for understanding how aggregation state evolves. Increases in the apparent fractal dimension may reflect either an increase in the average aggregate size, or collapse of the aggregates to form more dense packed structures. The apparent fractal dimension, as a function of ionic strength is plotted in Figure 4.

In most cases, an increase in ionic strength leads to an increase in the apparent fractal dimension. This is most significant in Syn15 and Syn16. These samples were initially more polydisperse (this is accounts for their very low initial apparent fractal dimension), but when ionic strength is increased, the aggregates are allowed to grow. In Syn12, the initial aggregate size is already very large, so changes in aggregate structure must be primarily due to changes in the aggregate structure (i.e. aggregate collapse). In all systems, the trends show that increasing ionic strength leads to larger/denser aggregate structures.
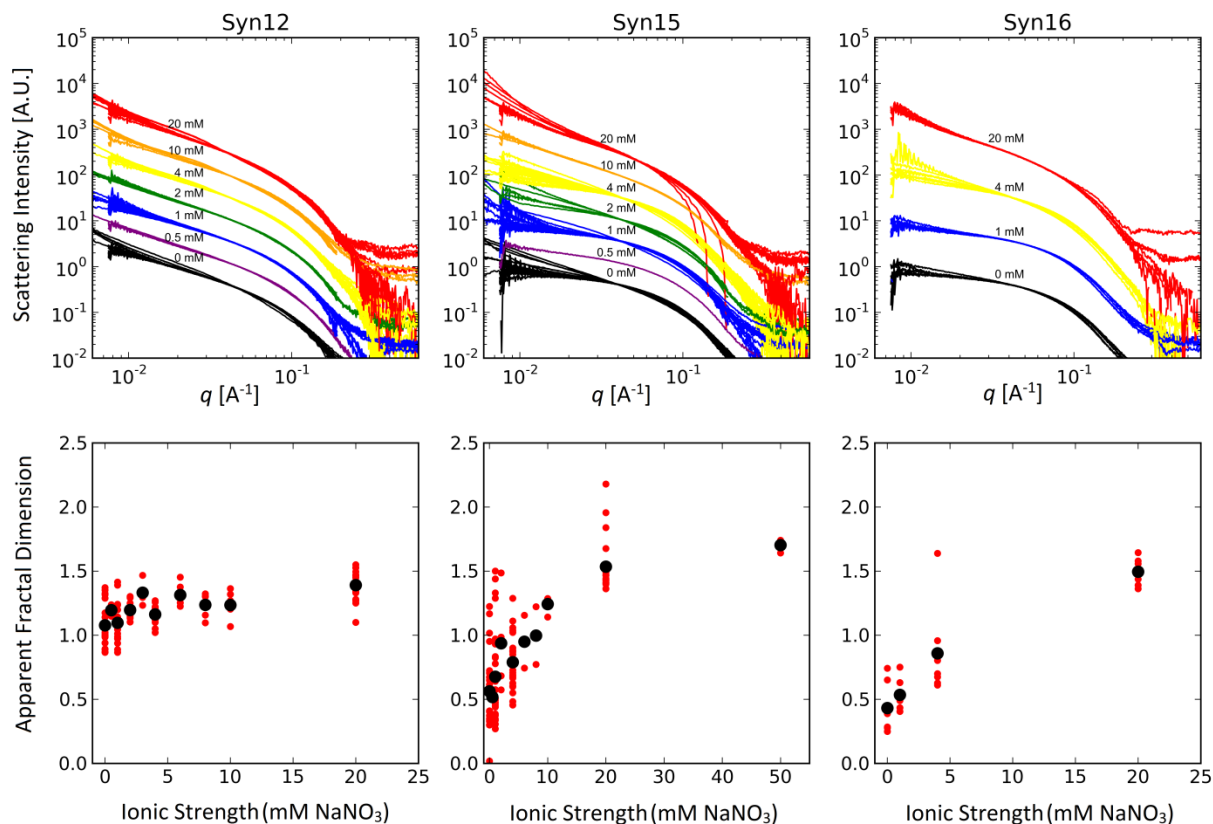
Figure 4: Upper plots show the processed SAXS data, obtained in solutions of 20 mM, 10 mM, 4 mM, 2 mM, 1 mM, 0.5 mM, and 0 mM NaNO₃. Scattering intensity is in arbitrary units, and curves have been shifted vertically for visual clarity. The log-log slope of these curves has been measured over the scattering range of 0.008 to 0.025 Å⁻¹, in order to obtain the apparent fractal dimension. The lower plots show the apparent SAXS fractal dimension, plotted as a function of the quantity of NaNO₃ salt in solution. Small red dots show the individual results from each experiment, while the large black dot shows the average fractal dimension at the salt concentration. In general, the apparent fractal dimension increases with ionic strength. However, these values reflect apparent fractal dimensions, and should not be interpreted as true structural fractal dimensions.

This interpretation is supported by optical observations of the solutions. Syn12 suspensions at become cloudy over the course of days, indicating the formation of dense, micron-scale aggregates, and sediment within weeks. After storage for > 1 year, a clear distinction is visible between suspensions which have been aged at different ionic strengths. Syn12 samples at concentrations of 1 mM or less are still optically transparent, homogenous suspensions. Those at concentrations of 4 mM or more have undergone extensive flocculation and gravitational sedimentation, with most particles settling out of suspension or adhering to the walls of the sample container. This increasing flocculation indicates a change in aggregate structure toward greater aggregate density.

3.3.2 Transport Behavior

Figure 5 displays four elution curves that were obtained in sequence during one nanoparticle transport experiment, using Syn10 in a 0 mM (deionized water) eluent. Each elution curve corresponds to one injection of nanoparticles, and the quantity of nanoparticles passing through the column is proportional to the integrated area under a curve. The behavior shown here is

typical of all experiments in terms of the evolving shape of the elution peak. For the example given, only a small fraction of particles pass through the column during the first injection, but more particles pass through the column on subsequent injections. Very little difference exists between injection 3, injection 4, and subsequent injections, suggesting the column is then saturated with particles.
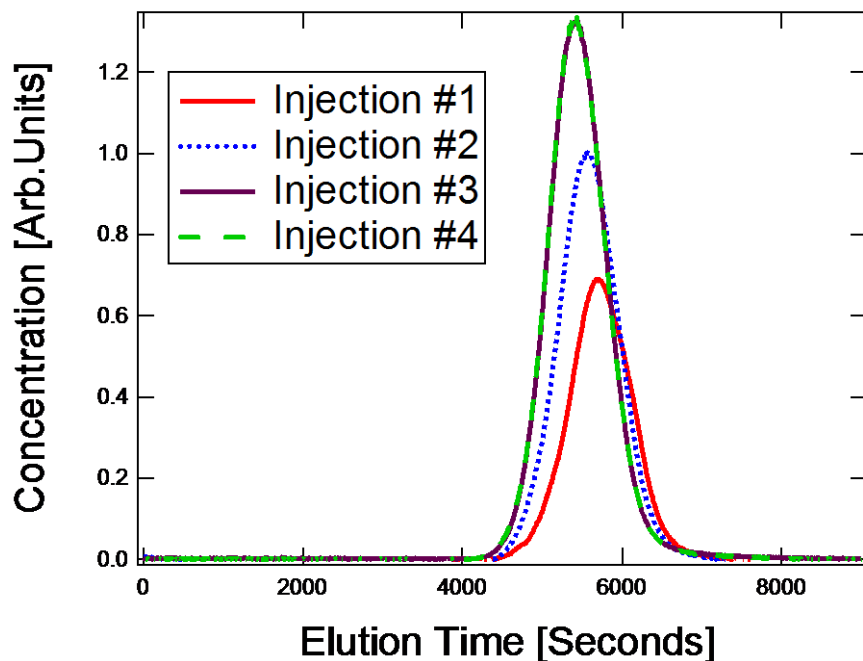

Figure 5: Example elution curves for ferrihydrite nanoparticles. (Syn10 in deionized water). Each curve corresponds to one injection in a series. Integrated area under the curve is proportional to the quantity of eluted particles.

Particle elution time depends on flow rate. Nanoparticle elution times are almost identical to those of an inert tracer (alizarin red dye). The peak elution concentration occurs from 45 to 50 minutes with a flow rate of 0.1 mL/min, and from 85 to 95 minutes at 0.05 mL/min flow rate. This is in good agreement with the predicted retention time for a non-interacting mobile phase based upon pore volume. Some variation is due to differences in column packing (columns were repacked between certain experiments, to remove air bubbles). Sand settling can create head space, which provides a mixing chamber, increasing retention time and smearing the elution peak. Close observation shows that the elution time depends upon column saturation, with later pulses eluting faster than initial pulses. Part of this effect can be explained by the selective removal of the first injected particles in each pulse, an effect which does not occur for saturated columns. Temporary attachment of particles to the sand surfaces will also increase elution time, so that more rapid elution may occur as sand surfaces become saturated and the sand-particle interactions decrease.

Deposition of particles within the column can be observed visually, due to the red/orange color of nanoparticles. Experiments using deionized water eluent result in a uniform orange color throughout the column, after the column has become saturated. At high ionic strengths (10 mM

41

with Syn10, and 4 mM with Syn12), large localized deposits of observed to form, and there is preferential deposition near the column outlet, see Figure 6. This is counter to the predictions of deep-bed filtration theory for a homogenous column, in which preferential deposition would be expected at the column inlet. Preferential deposition toward the column outlet may suggest aggregate reconstruction occurs during the course of elution.
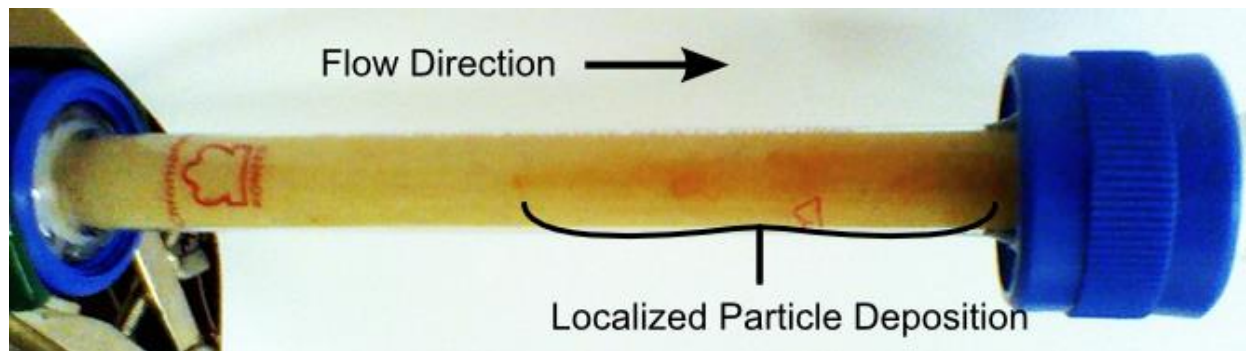
Figure 6: Column after several particle injections of particle, in a NaNO$_3$ solution for eluent. Localized deposits of particles are observed to accumulate near the column outflow.

A summary of the nanoparticle injection/elution measurements for all experiments is given in Figure 7. These plots show the fraction of nanoparticles eluted for each pulse that has been injected. Injection #1 corresponds to injection into a clean column. As expected, the initial injections tend to have very high particle retention (only a small fraction of particles are eluted). As the column begins to saturate with particles, a greater fraction of particles are eluted. The plots include three series of injections using Syn10 in deionized water, three series of injections using Syn12 in deionized water, three series of injections using Syn12 in 2 mM NaNO$_3$ solution, one series of injections with Syn10 in 10 mM NaNO$_3$, and one series of injections with Syn12 in 4 mM NaNO$_3$ solution.

Figure 7: Summary plots of nanoparticle pulse elution efficiency, for all experiments.

The experiments conducted in deionized water and in 2 mM NaNO$_3$ were modeled using deep bed filtration theory, to obtain maximum specific particle loadings, σ_{max}, and the clean bed

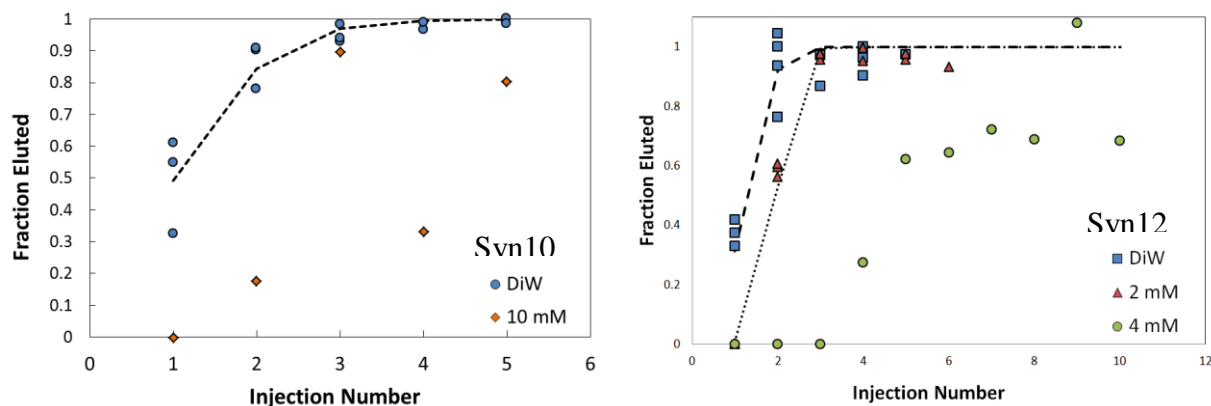filtration coefficient, λ_0. In all cases, the maximum particle loading is small, on the order of tens to hundreds of $\mu g/cm^3$. In the case of Syn12, a moderate increase in salt concentration from deionized water to 2 mM $NaNO_3$ lead to a doubling of σ_{max}, and a significant increase in the filtration coefficient.

Table 1: Estimated maximum specific particle loadings and filtration efficiencies.

Batch	Eluent [NaNO$_3$]	σ_{max} (pulses/column)	σ_{max} ($\mu g/cm^3$)	λ_0 (cm^{-1})
Syn10	0 mM	0.71 ± 0.16	31	0.128
Syn10	10 mM	>2.5	>110	-
Syn12	0 mM	0.77 ± 0.24	34	0.238
Syn12	2 mM	1.44 ± 0.04	64	13.8
Syn12	4 mM	>5	>220	-

Experiments with Syn12 in 4 mM $NaNO_3$ and Syn10 in 10 mM $NaNO_3$ showed dramatically different behavior. In both cases, 100% of the first ejection was retained, and subsequent injections showed erratic, unpredictable deposition behavior. Column saturation was not obtained, and deposition behavior suggested that it would not be obtainable in reasonable experimental timescales. Instead of an evenly distributed deposition, large localized deposits were observed.

In both of the higher ionic strength experiments, the elution fraction was erratic. In some cases, the eluted quantity of particles was estimated to be larger than the number of particles injected during that pulse. These pulses did not show the typically symmetric elution profile of other pulses. Our interpretation is that loosely adhered flocs can occasionally break loose, and that this can be triggered by interaction passing aggregates.

Particle straining and clogging effects are not expected to occur in this system. Particle straining is unlikely to be significant, due to the small particle sizes. Even very large aggregates are on the order of microns, while pores sizes between the sand grains are on the order of hundreds of microns. Clogging is also unlikely, with maximum deposits only on the order of hundreds of micrograms per cubic centimeter. Thus, deposition of particles is expected to involve particles sticking to the sand grain surfaces, and the maximum particle loadings are determined by the density of particles which can adhere to the surface.

3.3.3 Deposit Characterization

Scanning electron microscopy (SEM) was used in an attempt to characterize the structure of nanoparticle deposits on the sand grains. Sand grains were coated in carbon n by vapor deposition and imaged using a Leo 430 SEM, in both secondary electron (SE) and backscatter electron (BSE) imaging modes. In Figure 8, examples are shown of the clean sand. Although sand grains are generally macroscopically smooth, they are quite irregular at the micron scale as seen in Figure 8 (D). Despite cleaning, even crystallographically flat regions display some

amount of irregular deposits on the micron scale, as shown in Figure 8 (C). This irregular surface morphology makes the detection of nanoparticle deposits difficult.
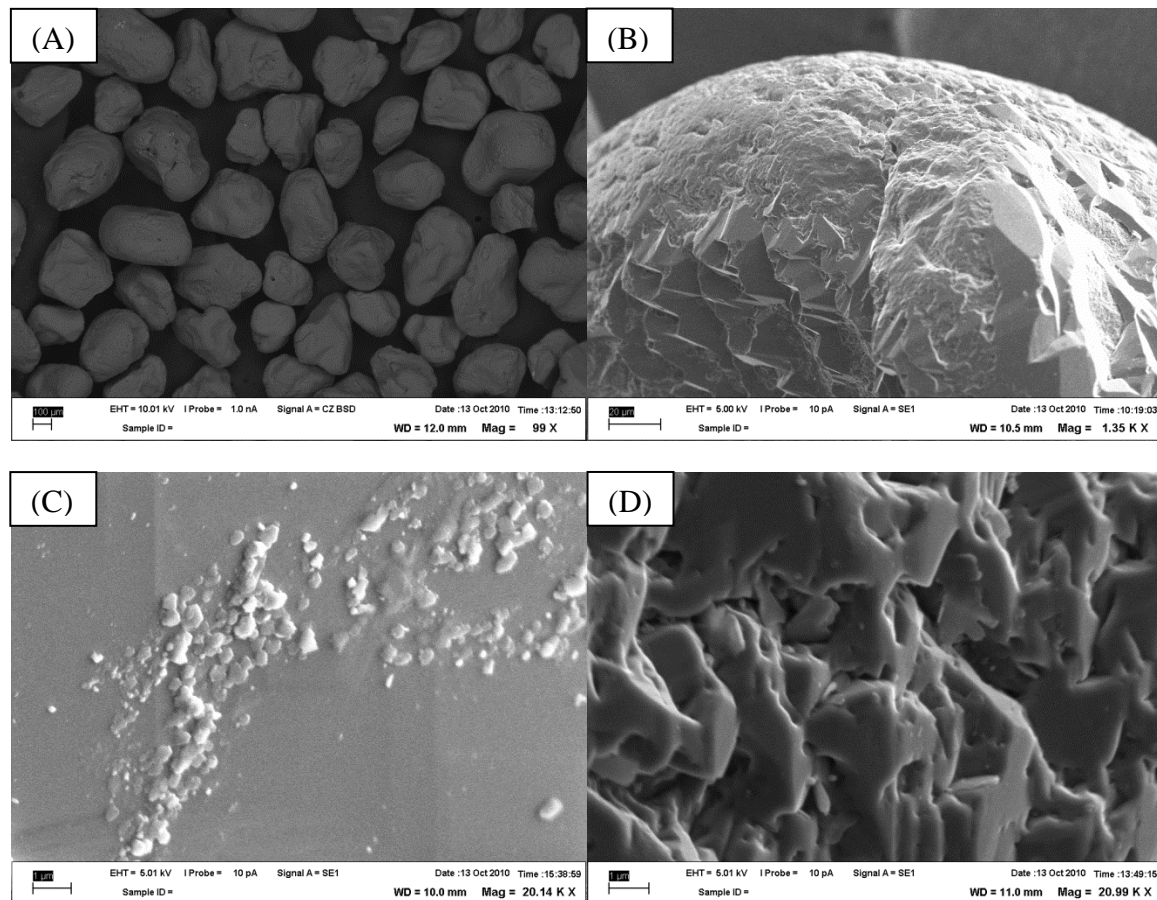

Figure 8: (A) Wide feed of view BSE image of clean sand grains, scale bar 100 µm. (B) Typical sand grain surface, SE image, scale bar 20 µm. (C) High resolution SE image of clean sand grain surface, showing deposits on a flat surface. (D) High resolution SE image of clean sand grain surface showing irregular surface geometry.

Sand grains that had accumulated ferrihydrite nanoparticles during column transport experiments were extracted from the Syn10 column experiments, both from DiW and 4 mM NaNO$_3$ eluents, and characterized similarly. Selected samples from Syn10 in 4 mM NaNO$_3$ are shown in Figure 9.

Although a visible orange/red tint makes it clear that ferrihydrite nanoparticle deposits are present on the surface of these sand grains, no distinct nanoparticle deposits could be confirmed. The maximum resolution is not sufficient to identify individual nanoparticles, only large particle aggregates. Because of iron's higher scattering coefficient than silica, BSE images were used to search for high contrast features that may contain ferrihydrite, and the chemical nature of these deposits were ascertained using energy dispersive spectroscopy (ESD). Many deposits, when analyzed at high resolution, showed signs of heterogeneous composition; not all surface features showed high BSE contrast. Over 20 spots were tested with ESD, although many of these contained iron, the elements titanium and chromium typically co-occurred, suggesting that these

44

were preexisting mineral deposits. No deposits were identified that showed the characteristic elemental signature of ferrihydrite.

Since the typical interactions of ferrihydrite nanoparticles with graphite coated Formvar showed sparse, relatively evenly distributed coatings on the Formvar surface, it may be possible that evenly distributed surface coatings of nanoparticles provide the most common type of deposit. In this case, the deposits would be too dispersed be easily resolved using SEM or ESD.
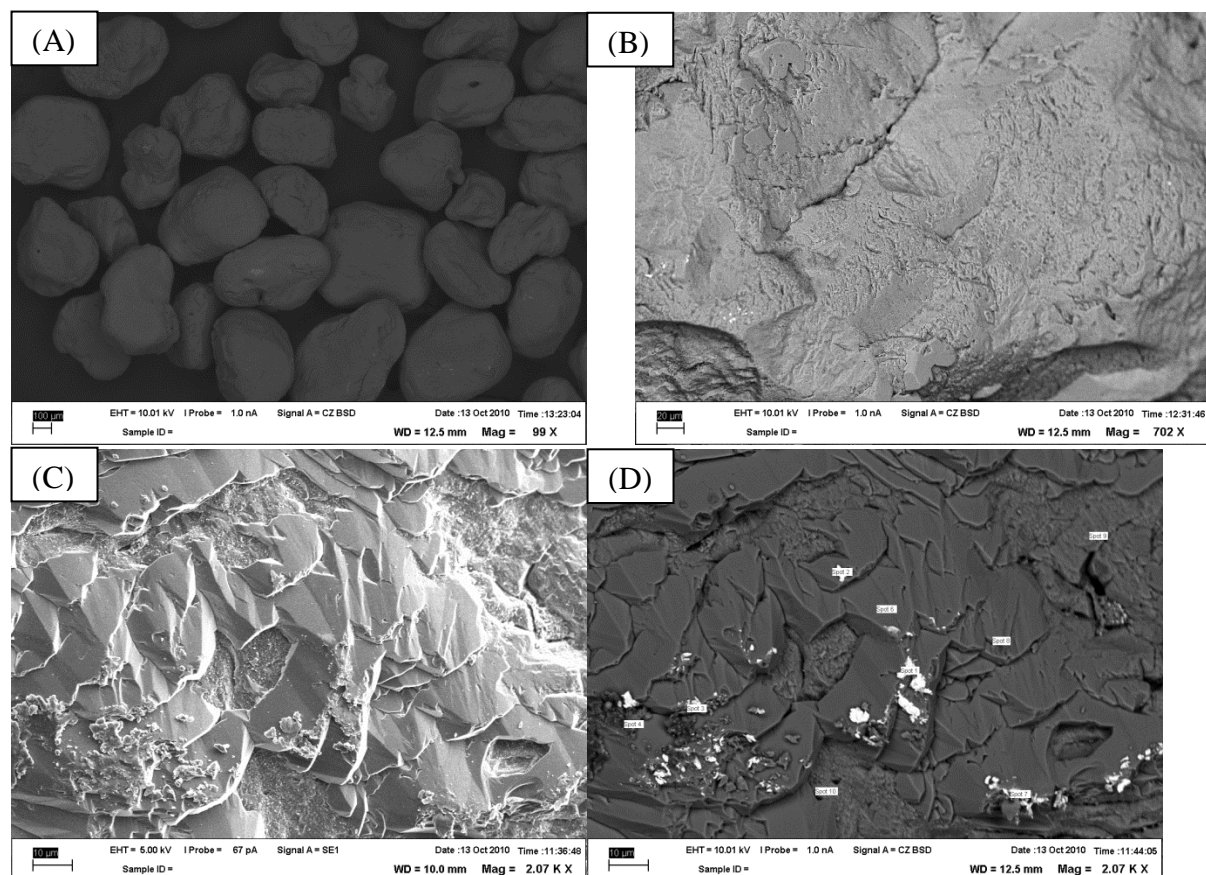
Figure 9: (A) Wide feed of view BSE image of sand grains extracted from 4 mM Syn10 column, scale bar 100 µm. (B) Typical sand grain surface, BSE image, scale bar 20 µm, with bright spots visible in lower left quadrant indicating the presence of heavier elements. (C) High resolution SE image of sand grain surface, extracted from 4 mM Syn10 column, showing deposits. Scale bar 10 µm. (D) Corresponding BSE image of the same area. Bright spots indicate the presence of heavier elements. Markers showing selections for ESD analysis are shown. Scale bar 10 µm.

3.4 Discussion

In this work, the ferrihydrite nanoparticles are consistently found exist in an aggregated state, even for suspensions that are stable against sedimentation and optically transparent over long time periods. This alone has important physical implications for nanoparticle transport, suggesting revisions to physical models for transport based on isolated particles. Traditional models based on Brownian diffusion, hydrodynamic collisions, and DLVO surface potentials for isolated spherical particles should not be expected to apply.

SAXS results show a clear increase in the apparent fractal dimension upon increasing ionic strength. This increase is due to two effects: the collapse of preexisting aggregates into denser packed structures with higher fractal dimension, and the growth of average aggregate size. These aggregate structural changes have profound impact on suspension stability. All samples, Syn10, Syn12, and Syn15, formed stable suspensions in deionized water conditions, but were found to flocculate and sediment after addition to moderate $NaNO_3$ solutions. This effect could be observed directly in cryo-TEM, where once open aggregate structures were replaced by densely packed structures.

At the same time, transport experiments showed that the presence of $NaNO_3$ leads to a significant increase in quantity of particles that can accumulate (*i.e.* greater maximum specific deposit), when compared with transport in deionized water. Comparison with cryo-TEM observations provides a potential explanation for this effect. Under deionized water conditions, nanoparticles tended to deposit evenly upon the carbon-coated Formvar support, and the maximum deposition density was relatively low, as aggregates maintained their relatively open, low density aggregate structure. In high salt solutions, very large particle clumps formed which also adhered to the carbon-coated Formvar support. It seems reasonable to extrapolate that the presence of salts in a subsurface environment will promote aggregate collapse, and enable greater particle loadings to accumulate.

It was found that $NaNO_3$ triggers a transition from particles being deposited evenly across the column, to a case where deposits are may be dense and localized. This shift in behavior may, in fact, be a consequence of aggregate growth and collapse. In low ionic strength conditions, a thin layer of nanoparticles may saturate a surface and inhibit further attachment at that location. When higher ionic strength favors aggregation, thicker layers of particles can accumulate, and favorable sites for deposit may accumulate large amounts of particles. These favorable sites for thick deposits may not be homogeneously distributed through the substrate. The results also indicated that thick accumulations of particles may become mechanically unstable; with massive releases of particles being observed at the column outlet, under high salt conditions. This has ramifications for monitoring nanoparticles as an emerging contaminant. If nanoparticles tend to be inhomogeneously distributed and/or transport in sudden particle releases, more extensive temporal and spatial sampling may be necessary to characterize the environmental distribution of particles.

The strong dependence of transport and depositional patterns on ionic strength has obvious importance for characterizing systems where ionic strength changes over time and space (*e.g.* due to seasonal variations in salinity), and may be important for determining how freshwater environments respond to saltwater intrusion, which may occur due to aquifer drawdown and sea-level rise.

The physical processes which determine how ferrihydrite aggregate structure form and what controls their deposition is still not fully determined, and appears to be highly sensitive to subtle

changes in suspension synthesis. More carefully controlled experiments are necessary to determine the physical controls on aggregate structure. It is worth noting that Syn12 transport behavior was more sensitive to ionic strength changes than Syn10. Although this unexpected complexity has made quantitative modeling difficult, it also suggests that future modifications to the synthesis procedure may be identified to enhance aggregate stability and increase the ability to deliver ferrihydrite nanoparticles into subsurface environments.

3.5 Acknowledgements

3.6 Works Cited

1. *Emerging Contaminant – Nanomaterials*, United States Environmental Protection Agency, May, 2012. EPA Publication Number: EPA 505-F-11-009
2. Wilkins, M.J.; Livens, F.R.; Vaughan, D.J.; Lloyd, J.R. The impact of Fe(III)-Reducing Bacteria on Uranium Mobility. *Biogeochemistry* **2006**, *78*, 125-150.
3. Lloyd, J.R.; Lovley, D.R.; Macaskie, L.E. Biotechnological Application of Metal-Reducing Microorganisms. *Adv. Appl. Microbiol.* **2003**, *53*, 85-128.
4. Hassellöv, M.; Kammer, F. Iron Oxides as Geochemical Nanovectors for Metal Transport in Soil-River Systems. *Elements* **2008**, *4*, 401-406.
5. Puis, R.W.; Powell, R.M. Transport of Inorganic Colloids through Natural Aquifer Material: Implications for Contaminant Transport. *Environ. Sci. Technol.* **1992**, *26*, 614-621.
6. Novikov, A.P.; Kalmykov, S.N.; Utsunomiya, S.; Ewing, R.C.; Horreard, F.; Merkulov, A.; Clark,S.B.; Tkachev, V.V.; Myasoedov, B.F. Colloid Transport of Plutonium in the Far-Field of the Mayak Production Association, Russia. *Science*. **2006**, *314*, 638-641.
7. Gilbert, B.; Lu, G. P.; Kim, C. S. Stable Cluster Formation in Aqueous Suspensions of Iron Oxyhydroxide Nanoparticles. *J. Colloid Interface Sci.* **2007,** *313*, 152-159.
8. Guyodo, Y.; Mostrom, A.; Penn, R.L.; Banerjee, S.K. From Nanodots to Nanorods: Oriented Aggregation and Magnetic Evolution of Nanocrystalline Goethite. *Geophys. Res. Lett.* **2003**, *30*, 1512 1-4.
9. Guzman,K.A.D.; Finnegan, M.P.; Banfield, J.F. Influence of Surface Potential on Aggregation and Transport of Titania Nanoparticles. *Environ. Sci. Technol.* **2006**, *40*, 7688–7693.
10. Gilbert, B.; Ono, K. R.; Chin, K.A.; Kim, C.S.; The Effects of Nanoparticle Aggregation Processes on Aggregate Structure and Metal Uptake. *J. Colloid Interface Sci.* **2009**, *330*, 285-295.
11. Liu, J.; Aruguete, D.M.; Murayama, M.; Hochella, M.F. Influence of Size and Aggregation on the Reactivity of an Environmentally and Industrially Relevant Nanomaterial (PbS). *Environ. Sci. Technol.* **2009**, *43*, 8178-8183.
12. McGechan, M.B.; Lewis, D.R. Transport of Particulate and Colloid-Sorbed Contaminants Through Soil, Part 1: General Principles. *Biosystems Engineering* **2002**, *83*, 255-273.
13. Ryan, J.N.; Elimelech, M. Colloid Mobilization and Transport in Groundwater. *Colloids Surf., A* **1996**, *107*, 1-56.
14. Sen, T.K.; Khilar, K.C. Review on Subsurface Colloids and Colloid-Associated Contaminant Transport in Saturated Porous Media. *Adv. Colloid Interface Sci.* **2006**, *119*, 71-96.
15. McCarthy, J.F.; Zachara, J.M. Subsurface Transport of Contaminants, *Environ. Sci. Technol.* **1989**, *23*, 496-502.

16. Tosco, T.; Bosch, J.; Meckenstock, R.U.; Rajandrea Sethi, R. Transport of Ferrihydrite Nanoparticles in Saturated Porous Media: Role of Ionic Strength and Flow Rate *Environ. Sci. Technol.* **2012**, *46*, 4008-4015.

17. Meakin, P.; Aggregation Kinetics. *Phys. Scr.* **1992**, *46*, 295-331.

18. Manley, S.; Cipelletti, L.; Trappe, V.; Bailey, A. E.; Christianson, Rebecca J.; Gasser, U.; Prasad, V.; Segre, P. N.; Doherty, M. P.; Sankaran, S.; Jankovsky, A. L.; Shiley, B.; Bowen, J.; Eggers, J.; Kurta, C.; Lorik, T.; Weitz, D. A., Limits to Gelation in Colloidal Aggregation. *Phys. Rev. Lett.* **2003**, *93*, 108302.

19. Gmachowski, L. Aggregate Structure and Hydrodynamics of Aggregated Systems. *Colloids Surf., A* **2005**, *255*, 105-110.

20. Roy, S.B.; Dzombak, D.A. Chemical Factors Influencing Colloid-Facilitated Transport of Contaminants in Porous Media. *Environ. Sci. Technol.* **1997,** *31* (3), *46*, 656-664.

21. Bai, R.; Tien, C. Particle Deposition Under Unfavorable Surface Interactions. *J. Colloid Interface Sci.* **1999**, *218*, 488–499.

22. Tien, C.; Payatakes, A.C. Advances in Deep Bed Filtration. *AlChE Journal* **1979**, *25* (5), 737-759.

23. Lin, M.Y.; Klein, R.; Lindsay, H.M.; Weitz, D.A.; Ball, R.C.; Meakin, P. The Structure of Fractal Colloidal Aggregates of Finite Extent. *J. Colloid Interface Sci.* **1990**, *137*, 263-280.

24. Yanwei, Z.; Meriani, S. Scaling Functions for the Finite-Size Effect in Fractal Aggregates. *J. Appl. Crystallogr.* **1994**, *27*, 782-790.

25. Teixeira, J. Small-Angle Scattering by Fractal Systems. *J. Appl. Crystallogr.* **1988**, *21*, 781-785.

26. Adrian, M.; Dubochet, J.; Lepault, J.; McDowall, A.W. Cryo-Electron Microscopy of Viruses. *Nature* **1984**, *308*, 32-36.

27. Gmachowski, L. Calculation of the Fractal Dimension of Aggregates. *Colloids Surf., A* **2002**, *211*, 197-203.

Chapter 4: Aggregation-induced Growth and Transformation of β-FeOOH Nanorods to Micron-Sized α-Fe₂O₃ Spindles

Intimate interconnection of crystal growth, aggregation and phase transformation are common during formation of nano- and microcrystalline materials from solutions. Yet the mechanistic linkages between the different processes are not well understood. This work studies the hydrothermal growth of akaganeite (β-FeOOH) nanorods and their transformation to micron-sized hematite (α-Fe₂O₃) spindles using high-resolution cryogenic transmission electron microscopy (cryo-TEM). Only akaganeite particles and hematite spindles were detected in the samples. Further, cryo-electron 3D tomograms show that akaganeite nanorods were aggregated into loose three-dimensional networks with some embedded hematite spindles. Based on cryo-TEM and additional X-ray diffraction, electron microscopy, and chemical data, a new mechanism for growth is proposed. First, formation of the early-stage hematite spindles is driven by phase stability change due to increase in size caused by oriented aggregation of akaganeite. Then, akaganeite particles continue to transform to hematite upon contact with and recrystallization onto hematite surfaces, making hematite grow with a constant aspect ratio and forming micron-sized nano-porous single-crystal spindles. This growth model is consistant with experimental observations, and presents a resolution to the long-time debate of whether the hematite spindles are formed via classical Ostwald ripening or by oriented aggregation of hematite nanoparticles. This aggregation-based concurrent growth and transformation model may also be applicable to crystal growth and phase transformation in other systems.

4.1 Introduction

In nanomaterials, aggregation, crystal growth, and phase stability can be interconnected. For example, 5 nm amorphous silica spheres have been shown to aggregate into 30-50 nm diameter particles that transform to single silicate crystals while retaining the size and shape of the precursor aggregate.[1] Another example is ferrihydrite particles, a few nm in diameter, that aggregate into rod-like chains, and then fuse into straight, single-crystalline goethite (α-FeOOH) rods.[2] Moreover, a study has reported how secondary crystals (of magnetite, Fe₃O₄) can continue to grow by addition and transformation of amorphous precursor particles.[3] The apparently tight mechanistic linkages between particle aggregation and phase transition seems relevant for describing (non-classical) crystal growth processes, but they are not fully understood.

Iron (oxyhydr)oxides provide an interesting system for development of models to explain linkages among aggregation, phase transformation and morphology development, because environmentally driven phase transitions and aggregation-based growth of iron (oxyhydr)oxides has been widely reported.[4-6] Additionally, iron (oxyhydr)oxide systems are important in many natural settings and industrial applications, and understanding the interplay between growth, nanocrystallinity, and phase transitions is important for understanding and controlling (for

example) corrosion processes, hydrometallurgy, heavy metal toxicity, pigment production, and magnetic data storage.

The formation of micron-sized α-Fe$_2$O$_3$ (hematite) particles from β-FeOOH (akaganeite) precursor nanoparticles has been reported under hydrothermal conditions.[7,8] The final product is monodisperse single hematite crystals. There has been considerable debate as to whether the hematite particles form by aggregation of hematite nanoparticles[9-11] or instead by dissolution and reprecipitation.[8,12]

In this study, the growth of akaganeite and its transformation to hematite in aqueous solution was analyzed using a combination of hydrothermal experiments, high-resolution transmission electron microscopy (HRTEM), cryogenic transmission electron microscopy (cryo-TEM), and synchrotron X-ray diffraction. A new growth model is proposed in which aggregation of primary akaganeite particles precedes phase transformation.

4.2 Experiments and Results

Nanoparticle suspensions were prepared by heat treating aqueous solution containing 20 mM FeCl$_3$ and 0.45 mM NaH$_2$PO$_4$ at 100°C for up to 7 days, following the method of Refs. 7 and 10. Additional details about methods are provided in section 4.4. Phosphate was added to the synthesis to induce formation of spindle-shaped hematite that is partly transparent to TEM. Without phosphate, micron-sized pseudo-cubes of hematite form.[9] It has been suggested that phosphate ions adsorb more strongly to the (hk0) crystal faces of hematite, and hence growth along the c-axis is favored.[13]

Upon heating at 100 °C for <1 hour, samples changed from their original translucent yellow color to a translucent deep red-brown color. After heating for ~50 hours, the samples became cloudy, and after 60 hours of aging the color turns more orange-brown and particle sedimentation occurs. The pH of the ferric solutions drops from 2.2 before heat treatment to 1.5 - 1.6 afterwards.

Ferron assay measurements of dissolved supernatant iron concentration in centrifuged samples showed a decrease from 20 mM to 10 mM after 1 hour, and a continuous decrease with increased heating time to a value of 0.9 mM after 167 hours.

Figure 1a shows synchrotron X-ray diffraction data at aging times from 15 hours to 102 hours. At early times, all diffraction lines were from akaganite, indicating that akaganeite is the dominant phase. Hematite remains below the detection limit until 56 h of aging. By 65 h, hematite is abundant. Only trace amounts of akaganeite can be detected by X-ray diffraction after 88 hours, indicating almost complete replacement (in wt%) of this phase by hematite.
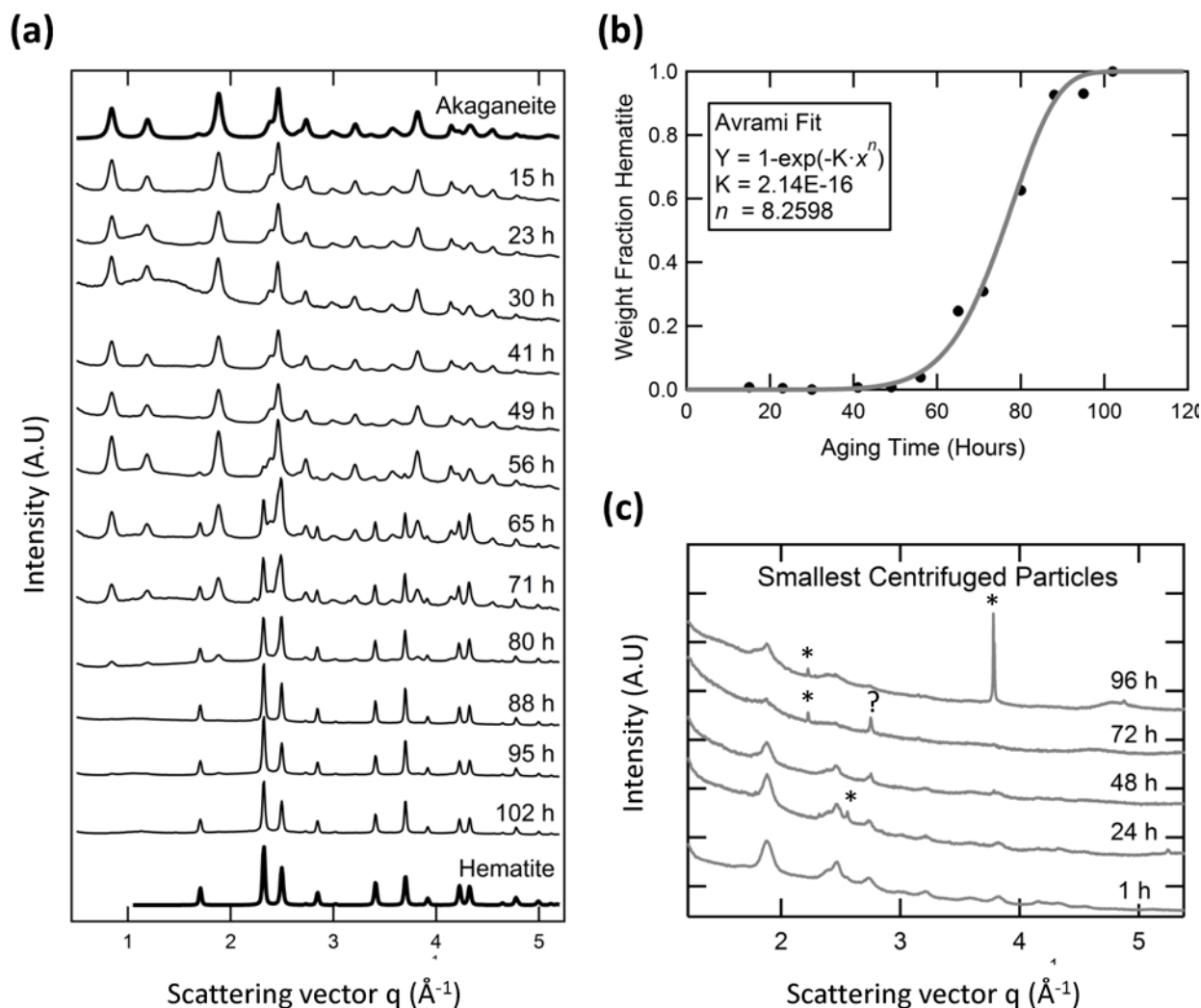
Figure 1. X-ray diffraction. (a) Synchrotron X-ray data of samples heat treated for 15 – 102 h. The top and bottom curves show computed, refined curves for 100% akaganeite and 100% hematite, respectively. (b) Weight fraction hematite with treatment time, obtained from (a); solid curve represents Avrami fit to data. (c) Powder X-ray diffraction (Co Kα λ) of the smallest particles in samples after heat treatment for 1 - 96 h. The narrow diffraction peaks in (c) denoted with asterisks are from the Si-substrate, the 2.82 d-spacing on 72 h data denoted ? is unidentified but not hematite. The scattering vector is defined as $q = 4\pi \sin(\theta)/\lambda$.

Rietveld total pattern fitting was performed to determine the mass fraction of each phase and respective particle sizes over time using MAUD.[14] Akaganeite (I 2/m) lattice parameters[15] (a, b, c, β) were refined by fitting the 15 h sample to a=10.587 Å, b = 3.032 Å, c= 10.513 Å and β = 90.41°. Hematite (R$\bar{3}$c) lattice parameters[16] (a, c) were refined by fitting the data from the 102 h sample to a = 5.032 Å and c = 13.800 Å. The mass fraction of each phase was obtained from whole pattern analysis of intermediate time-point X-ray data, with particle size and abundances as free refinement parameters. Fits of all data are good (Rwp% always less than 10, but typically between 2.6 and 4.6). The mass fraction curve was fit using an Avrami transformation model (Fig. 1b). An Avrami exponent of 8.3 was obtained. An Avrami exponent of >4 suggests non-standard growth kinetics, with rapid transformation following a significant incubation period.[17]
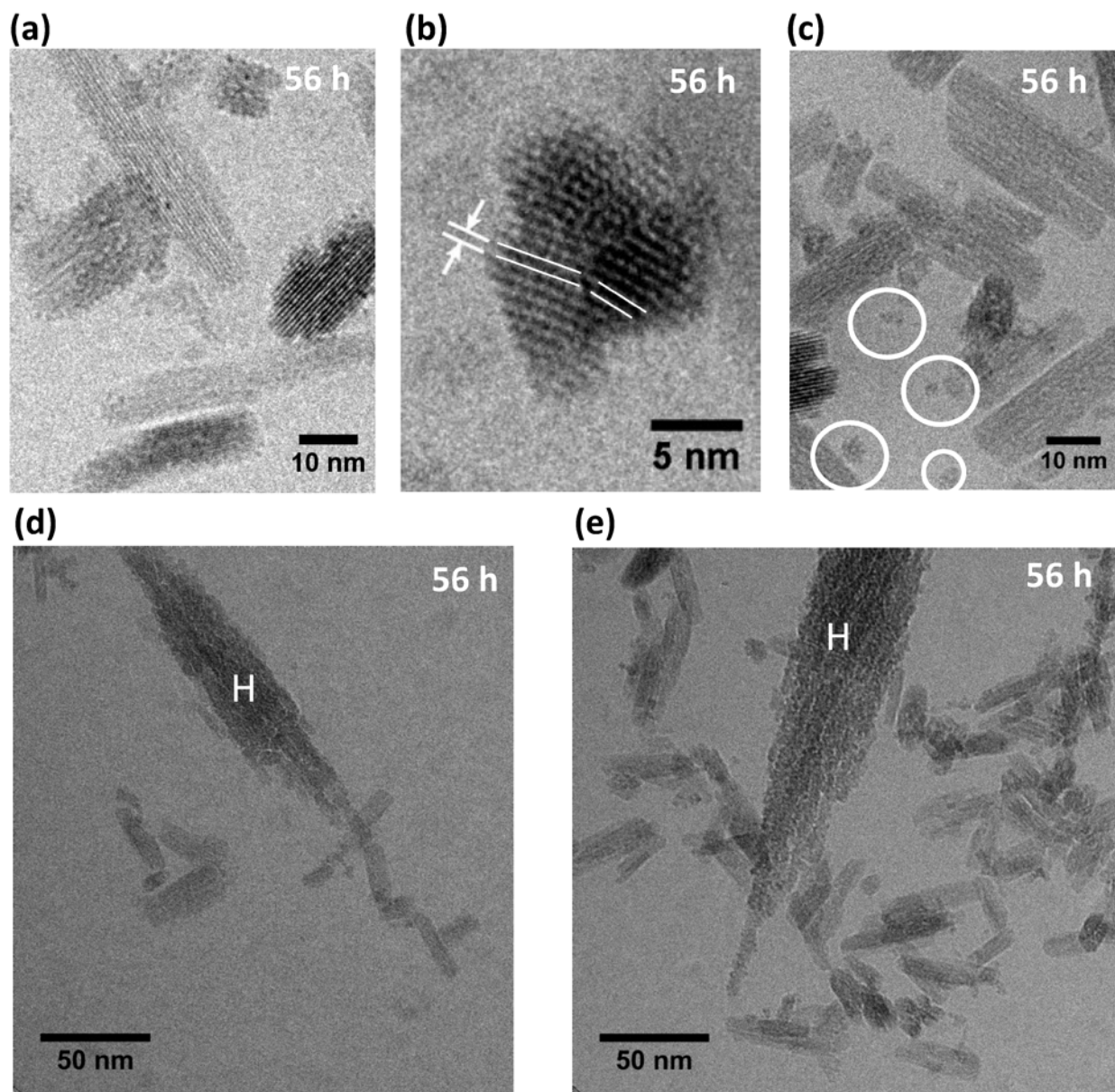
Figure 2. Cryo-TEM images, after 56 h heat treatment. (a)-(c) High-resolution images of akaganeite rods. Lattice spacings in (B) are ~0.74 nm. White circles in (c) surround very small akaganeite particles. (d)-(e) Broad-field views showing connectivity of akaganeite particles and hematite spindles (H).

TEM images of the samples taken after different times of heat treatment (examples shown in Figs. 2 and 3) showed in particular two particle types with different morphologies: rods of akaganeite and larger spindle-shaped hematite, as expected based on the synthesis approach.[7,10,12] Particle phases were identified from lattice fringe spacings. At early aging times, the akaganeite particles dominated but TEM also revealed that some spindle-shaped hematite particles were present after 23 h of treatment. In correspondence with TEM observations, X-ray diffraction of size selective samples obtained by centrifugation of samples aged for 1, 24, 48, 72, 96 h showed

54

that the largest size particle fractions contain hematite if samples had been aged for 24 hours or more.

TEM images also revealed a subset of very small particles with pseudo-spherical shape and size ≤5 nm (circled in Fig. 2c). Although previous authors[11] posited the existence of small hematite particles, no evidence for such particles was seen in this study. X-ray diffraction patterns obtained for the smallest size fractions of samples aged for 1, 24, 48, 72, and 96 h only revealed akaganeite (Fig. 1c).
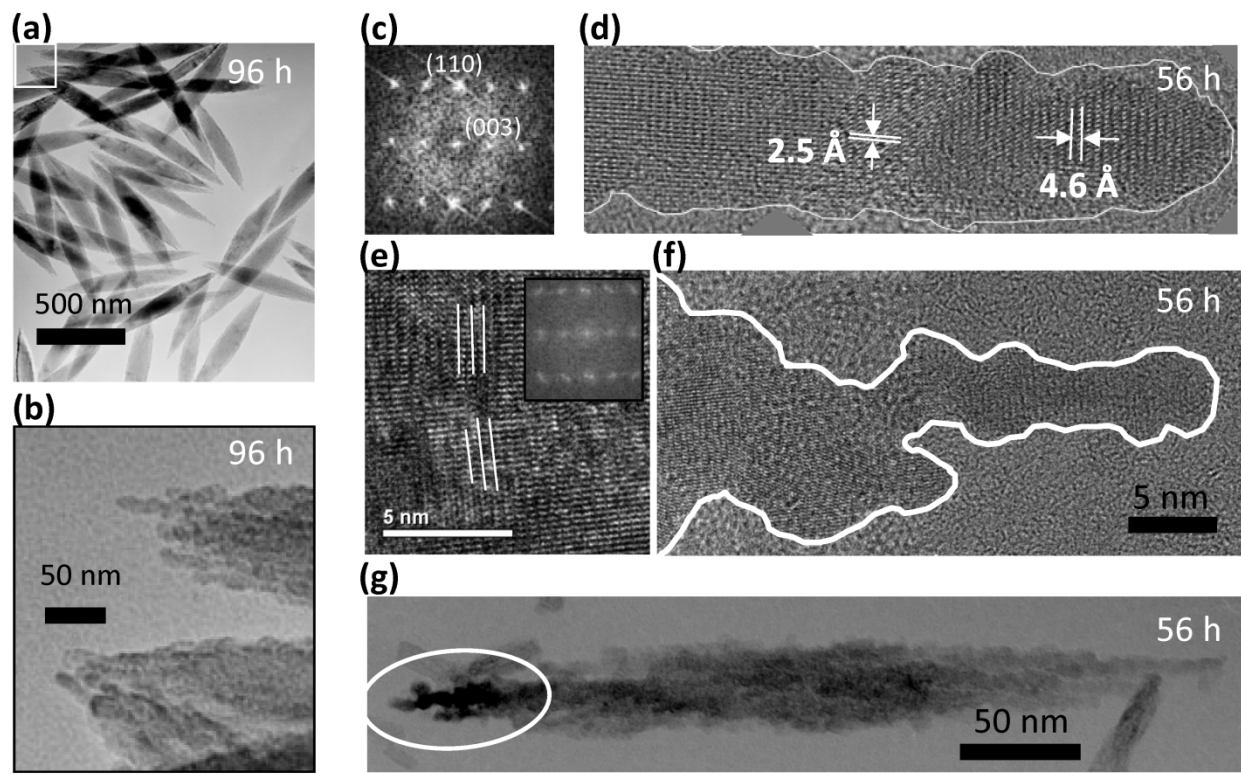
Figure 3. TEM images of hematite spindles, after 56 h and 96 h. White-boxed area in (a) is enlarged in (b). Fast-fourier transformed images in (c) and (e) show aligned and nearly aligned nanocrystalline grains in protruding spindle ends like those in (d) and (f). White ellipsoid in (g) surrounds contrast from hematite grains with different crystalline orientation.

 TEM images were used to measure the lengths and widths of akaganeite rods and hematite spindles in samples aged for 23, 49, 56, 71, 102, and 166 h. The lengths and widths of 300 akaganeite particles were measured for samples from each time point. The particle sizes of akaganeite were calculated as their lengths times widths squared, and the particle size distribution fit with a log-normal distribution (number weighted). Figure 4a shows the evolution of the akaganeite particle size distribution, with the populations normalized to reflect the total amount of akaganeite in suspension, as estimated from Rietveld refinement of synchrotron X-ray diffraction patterns. The mean particle size increased over time, with a very slight narrowing in the distribution breadth. This is due to an increase in mean particle width from 7.6±2.3 nm to 11.5±2.5 nm and decrease in the mean particle length over time. Particle aspect ratio decreases

monotonically from a value of 3.3±1.9 at 23 hours, to 1.7±0.8 at 102 hours (Fig. 4b). Hematite particles grew with a constant aspect ratio of 6-7 and increased in length from 200±30 nm at 23 h to 580±30 nm at 71 h and 670±60 nm at 166 h (Fig. 4c).
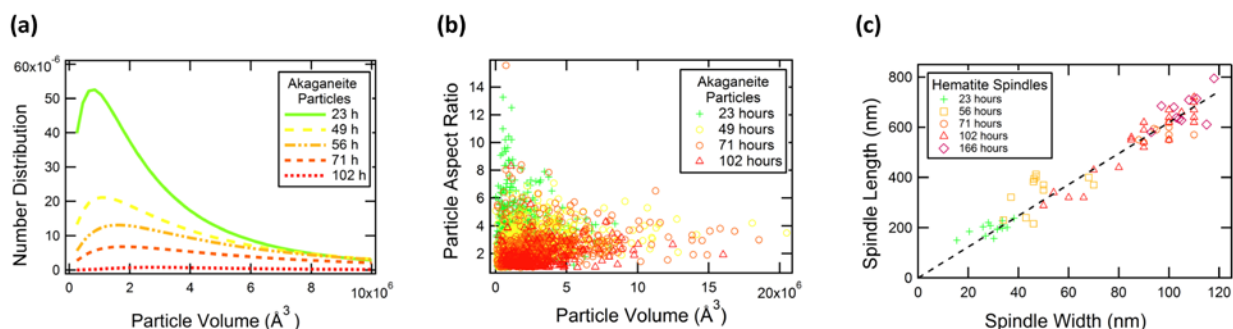
Figure 4. Particle growth with heat treatment time. (a) Particle size distribution of akaganeite. (b) Aspect ratio of akaganeite particles. (c) Hematite spindles' width and length.

High-resolution TEM images showed akaganeite rods are elongate along their *b* axis. Cryo-TEM analyses achieved lattice fringe resolution for akaganeite nanoparticles in a sample recovered after 56 h of treatment. Preservation in vitrified ice allowed us to image the akaganeite rods in multiple orientations, including side- and end-on (Figs. 2a,b), and to capture particle arrangements as *in aqua*. As also seen in conventional TEM analysis (data not shown), small groups of akaganeite rods were often crystallographically aligned and primarily attached on their (100) and (001) surfaces. The small discrepancy in lattice parameters for the *a* and *c* axes in akaganeite's monoclinic structure can lead to low angle grain boundaries, as observed in Fig. 2b.

The hematite spindles are much larger than the akaganeite rods and are nano-porous. The hematite spindles typically diffract as single crystals, but their outlines are very irregular and they appear to be composed of several thousand crystallographically aligned subparticles (3-5 nm thick) (Fig. 3a,b). The hematite spindles and their nanoporous structure are elongate along the hexagonal *c* axis of hematite (Figs. 3c,d). Substructure is most apparent where component units protrude from the spindle ends. Irregularities on hematite crystal surfaces (Figs. 3b,d,f,g) have shapes similar to those of primary akaganeite nanoparticle. Occasionally, low-angle grain boundaries are present within the hematite spindles (Fig. 3e). In addition, slight variations in diffraction contrast between adjacent regions of hematite (see white circle in Fig. 3g), suggests that the hematite spindles contain domains with slightly different crystallographic orientations.

Slices of TEM tomograms obtained for a hematite spindle after 56 h of aging revealed an irregular external surface and high internal porosity (see cross sections in Fig. 5a,b). With further aging time, the internal porosity appeared to decrease, but some porosity remained even after 96 h of aging (Fig. 3b).

56
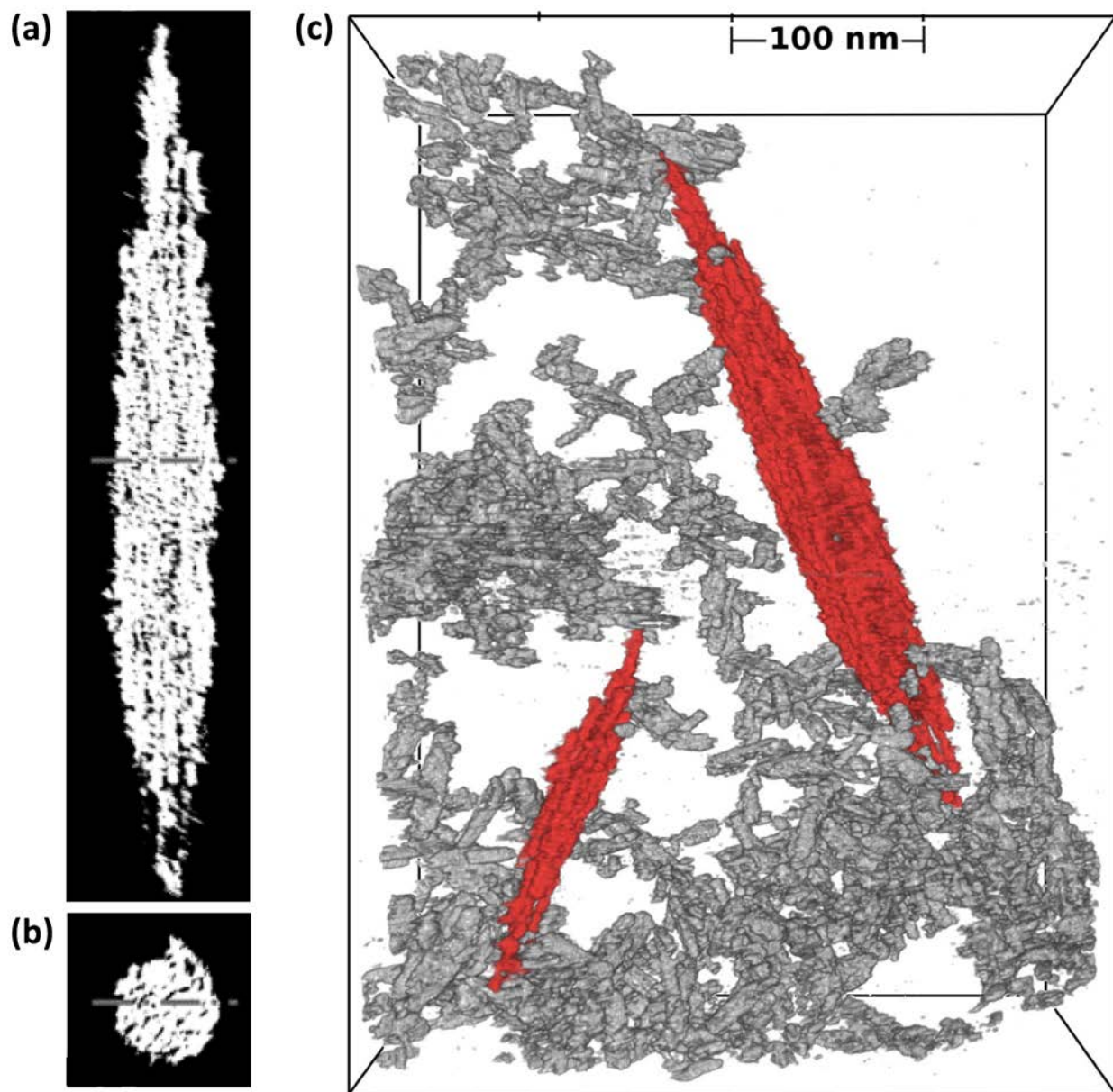
Figure 5. Cryo-TEM tomographs. (a)-(b) Cross sections of the large hematite spindle in (c). (c) Broad-field view of akaganeite particles (grey) in 3D-network with hematite spindle (red).

TEM images of dried samples suggest that akaganeite and hematite particles are co-aggregated (Fig. 3g), however these results may be influenced by drying artifacts. Cryo-TEM analysis circumvented this problem by directly imaging the particle aggregation state *in aqua* in three dimensions. Figure 5c shows a broad field-of-view 3D cryo-TEM image of a vitrified sample after aging for 56 h. The images show that akageneite particles form loose open networks around hematite. Akaganeite crystals are often observed in contact with the hematite spindles.

Dissolved iron concentrations were compared with chemical equilibrium calculations using MINTEQ. These calculations show that the starting solutions (20 mM $FeCl_3$, 0.45 mM

NaH$_2$PO$_4$, pH 2.2) should reach equilibrium with bulk hematite (log[{Fe^{3+}}^{2}/{H$^+$}^{6}] = -1.418) at a pH of 1.3 and a dissolved iron concentration of 0.28 mM. The pH values are in good agreement with measurements, and dissolved iron concentrations (~ 1 mM at 102 hours) are moderately higher than expected.

From the X-ray diffraction data, which provide relative weight fractions of akaganeite and hematite, and from the TEM data, which provide detailed information on particle shape and size distributions, the concentration of particles was estimated for samples recovered at each time-point. These calculations show that the number of akaganeite particles decreased by two orders of magnitude during the course of the experiment, from $1 \cdot 10^{21}$ particles/m^3 at 23 h to $2 \cdot 10^{19}$ particles/m^3 at 102 h. However, the number of hematite particles is roughly constant over time (~$1 \cdot 10^{17}$/m^3). Even at 102 h, when the suspension is dominated by hematite spindles on a mass basis, akaganeite nanoparticles still outnumber hematite particles, but the reactive surface areas of akaganeite and hematite are comparable.

4.3 Discussion

TEM observations show clear evidence for growth of akaganeite particles by oriented aggregation, where the particles (Fig. 6i) aggregate, align, and subsequently fuse to form a single crystal (Fig. 6ii). Many larger akaganeite particles have irregular surface morphology, and appear to consist of two or three rods sitting directly side by side (Fig. 2b). In some cases, particles were aligned, but not yet fused (Fig. 2a,c). Such aggregate-like particle morphologies with single-crystalline, low-angle and twin boundaries are often found in nanoparticle systems that grow by oriented aggregation.[18,19] This evidence is comparable to that reported previously to indicate operation of this growth mechanism, a pathway that was recently directly confirmed for a similar iron oxyhydroxide phase by *in situ* high-resolution TEM experiments.[6]

The initial formation of hematite spindles was not directly observed in this experiment. Because the number of hematite spindles is relatively constant over time (from 23 to 102 h), the formation of hematite spindles is presumably most rapid during the first hours of hydrolysis. It is possible that concurrent nucleation of a small number of hematite nanoparticles occurs concurrently with akaganeite during the early stages of precipitation. An alternative possibility is that all initial precipitates are akaganeite, and hematite forms later. It has been suggested that the transformation from akaganeite to hematite by dehydration and atomic rearrangement is thermodynamically favored only for large particles (surface area <2000 m^2/mol and particle width greater than 4 nm), due to akaganeite's lower interfacial energy, relative to hematite.[20] In this case, hematite nucleation may actually be driven by the aggregation of akaganeite rods (Fig. 6iii), i.e., akaganeite rods aggregate until the resulting particles reach a size where transformation to hematite is favorable. Size-driven phase transformations are common in the iron (oxyhydr)oxide systems.[20] This would be consistent with the fact that all observed hematite spindles were larger than 15 nm by 150 nm, significantly larger than the vast majority of akaganeite rods. The more rapid formation of hematite during early stages of precipitation could

be explained by evolving surface energies (due to changing pH), and evolving particle morphology (as the akaganeite particle aspect ratio is higher at earlier times).

The nucleation of hematite may involve more than just achieving a minimum aggregate size, it may also involve oriented attachment between particles. Phase transformation driven by oriented attachment has been proposed previously in other systems. For example, the twin interface that can form during oriented attachment-based growth of anatase shares some structural characteristics with rutile, thus may to serve to nucleate thermally-driven transformation to rutile.[21] Other studies have shown that aggregation of nanoparticles can alter nanoparticle crystallinity[22] and that surface-bound molecules may induce phase transformations in nanoparticles.[23] Thus, it seems probable that large aggregates of aggregated akaganeite particles may occasionally produce the conditions needed to nucleate hematite, subsequently leading to the formation of spindle by dehydration and atomic rearrangement.

The nano-porous structure of hematite spindles strongly suggests construction from crystallographically aligned (and nearly aligned) subparticles, as found for growth by oriented attachment.[4,18,24,25] It was proposed that similarly synthesized hematite spindles have formed by aggregation of hematite nanoparticles.[9-11] This idea has been very strongly argued against, in favor of a process where akaganeite dissolves and reprecipitates as hematite.[8,12] Sugimoto and Muramatsu[12] make a strong case that the formation of hematite spindles cannot be due to continuous precipitation and aggregation of individual hematite nanoparticles, based on their observations that the final number of spindles can be manipulated by adding hematite seeds (<5 nm diameter) to the solution. If small hematite particles were continuously generated in solution, such seed particles would not have a major impact on the final product. Notably, there is no sign of small hematite nanoparticles in the solution. Also, because chemical analyses show a low Fe concentration and low pH, it is unlikely that hematite particles could be nucleated homogenously. We therefore agree with Sugimoto and Muramatsu,[12] but note that their analysis does not preclude the possibility that the aggregation involves akaganeite onto hematite, followed by phase transformation.

A recent paper[11] studied cryo-plunged $FeCl_3$(aq)-samples that had aged in an autoclave at 160-200 °C and found that individual hematite nanoparticles exist as the sole precursors to hematite spindle formation. At this temperature, dehydration of individual precursor particles would be more strongly favored than in the experiments performed here, and thus growth by hematite nanoparticle aggregation may be favored.

Only the precursor nano-scale akaganeite and the end product hematite spindles are detectable in the samples from this study. The constant number of hematite spindles throughout the experiment (from 23 h to 102 h) indicates that hematite spindle nucleation is completed during the first hours of hydrolysis and the primary process controlling hematite formation thereafter is growth (not nucleation). This conclusion is supported by the high monodispersity of the spindle size distribution at all time points (Fig. 4c).

The *in aqua* cryo-TEM finding of akaganeite and hematite particles in extended networks in solution requires an altered view of particle interactions in suspension. Traditional models of stable colloidal suspensions, based on DLVO theory, posit that electrostatic repulsion inhibits direct contact between particles and formation of large clusters.[26] However, in this suspension there is extensive evidence for direct contact between particles, i.e., almost all particles participate in a network, and this particle contact may provide opportunities for enhanced crystal growth.

The simplest explanation for the observed hydrothermal growth of monodisperse micron-sized nanoporous hematite spindles at 100 °C is that akaganeite transforms to hematite upon making suitable contact with a hematite surface (Fig. 6iv,v). In this scenario, the transformation would occur by an advancement of the akaganeite-hematite interface. Intergrowths of akaganeite within hematite were not observed, suggesting that the reaction occurs rapidly upon suitable attachment.
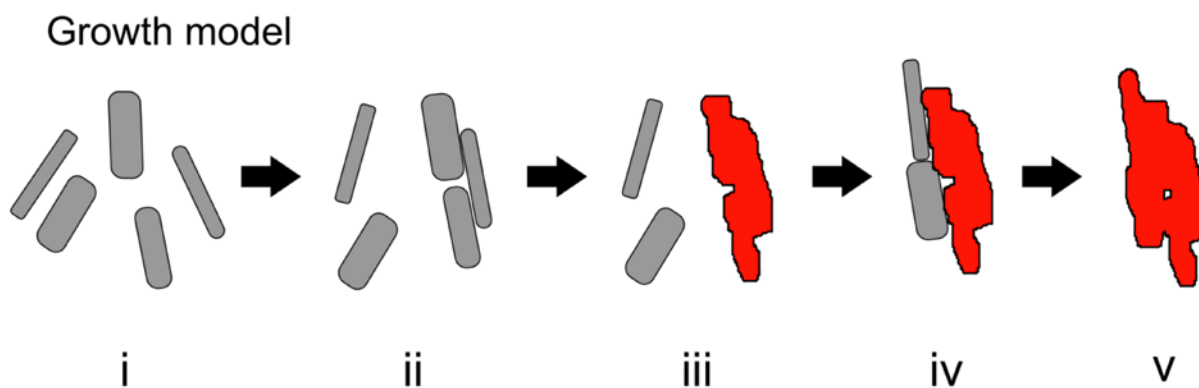
Growth model

Figure 6. Growth model. Akaganeite particles (grey rectangles, i) aggregate (ii) and transform to hematite spindles (red structures, iii). After the "incubation period" (i-iii), the hematite spindles grow more rapidly through aggregation of akaganeite particle (iv) followed by phase transformation of akaganeite to hematite (v).

A summary of the proposed model for growth, aggregation and transformation is shown in Fig. 6. In this model, growth and phase transition are induced first by oriented aggregation of primary particles (i.e. akaganeite) and later by aggregation of primary particles onto the secondary particles (i.e. hematite spindles). This model may be applicable in explaining growth and phase transitions in several other two-phase systems where particle aggregation exists and where ion concentrations and pH do not permit homogenous nucleation of the secondary particles.

4.4 Methods

Nanoparticle suspensions were prepared from an aqueous solution containing 20 mM $FeCl_3$ and 0.45 mM NaH_2PO_4. Solutions were filtered through 0.2 μm pores, and placed in closed Pyrex bottles. Precipitation was induced by heating in a preheated oven at 100 °C for up to 167 hours, following the method of Refs. 7 and 10. The particle growth and transformation processes were documented by removing a series of bottles from the oven at different time points. Containers were cooled by immersion in cold running water. The samples were stored in solution at room temperature prior to analysis.

Synchrotron X-ray diffraction patterns of dried suspensions were measured at the Advanced Light Source, Lawrence Berkeley National Laboratory, beam line 11-3-1 (photon wave length $\lambda = 0.729294$ Å).

Transmission electron microscopy (TEM) images of particle suspensions after 23, 56, 71, 102 and 166 h of heat treatment, drop-casted and dried onto holey amorphous carbon films, were obtained using a JEOL 200CX microscope and a FEI Technai microscope at the National Centre for Electron Microscopy, Lawrence Berkeley National Laboratory.

2D and 3D Cryo-TEM images were acquired on a JEOL–3100-FFC electron microscope equipped with a FEG electron source operating at 300 kV, an Omega energy filter (JEOL), cryo-transfer stage, and a Gatan 795 2Kx2K CCD camera (Gatan Inc., Pleasanton, CA, USA) at the Life Science Division, Lawrence Berkeley National Laboratory. Prior to sample addition, carbon-coated lacy formvar support grids (Ted Pella) were pretreated by plasma discharge to induce sample wetting. Citrate-capped, 10 nm colloidal gold particles (BBInternational) were added to the grid, to serve as fiducial markers for image alignment. A ~4 µm drop of sample suspension was added to each grid. Excess solution was removed by blotting with cellulose filter paper, leaving a thin film, between 100 and 400 nm thick, which is immediate plunged into liquid ethane at -180 °C. This transforms the solution to vitreous ice, allowing particle and aggregate structures to be imaged directly in the TEM.

Five tomographic datasets, at magnifications of 50 kX to 110 kX, were produced by acquiring a tilt series, over a range of ±65 degrees, at 2° increments. Image alignment was achieved by fiducial tracking with etomo.[27] Fiducial particles were digitally removed and a 3D reconstruction was computed using tomo3d.[28] The tomogram was converted into a 3D binary image, using the automated trainable segmentation algorithm in FIJI.[29]

Size selective ultra-centrifugation (up to 300 k rcf for 30 minutes) was used to sediment out increasingly smaller particles, allowing us to isolate very large and very small particles for further analysis by X-ray diffraction, via PANalytical X'Pert Pro diffractometer with a Co source (Kα $\lambda = 1.79021$ Å). After the final centrifugation step, the dissolved iron concentrations in the remaining supernatant solutions (which are colorless and transparent) were measured using UV-Vis spectroscopy with ferron dye (600 nm adsorption band).[30] This chemical assay is only sensitive to dissolved iron species.

4.5 Acknowledgements

4.6 Works Cited

1. Kumar, S.; Wang, Z.; Penn, R. L.; Tsapatsis, M. A Structural Resolution Cryo-TEM Study of the Early Stages of MFI Growth. *J. Am. Chem. Soc.* **2008**, 130, 17284-17286.

2. Yuwono, V.M.; Burrows, N.D.; Soltis, J.A.; Penn, R.L. Oriented Aggregation: Formation and Transformation of Mesocrystal Intermediates Revealed. *J. Am. Chem. Soc.* **2010**, 132, 2163-2165.

3. Baumgartner J.; Dey, A.; Bomans, P.H.H.; Coadou, C.L.; Fratzl, P.; Sommerdijk, N.A.J.M.; Faivre, D. Nucleation and Growth of Magnetite from Solution. *Nature Mater.* **2013**, 12, 310-314.

4. Banfield, J.F.; Welch, S.A.; Zhang, H.; Ebert, T.T.; Penn R.L. Aggregation-Based Crystal Growth and Microstructure Development in Natural Iron Oxyhydroxide Biomineralization Products. *Science* **2000**, 289, 751-754.

5. Yuwono, V.M.; Burrows, N.D.; Soltis, J.A.; Do, T.A.; Penn, R.L. Aggregation of Ferrihydrite Nanoparticles in Aqueous Systems. *Faraday Discussions* 2012, **159**, 235-245.

6. Li, D; Nielsen, M.H.; Lee, J.R.; Frandsen, C.; Banfield, J.F.; De Yoreo, J. J. Direction-Specific Interactions Control Crystal Growth by Oriented Attachment. *Science* **336** (2012) 1014-1018.

7. Ozaki, M.; Kratohvil, S.; Matijevic, E. Formation of Monodisperse Spindle-Type Hematite Particles. *J. Colloid. Interface Sci.* **1984**, 102, 146-151.

8. Sugimoto, T.; Muramatsu, A.; Sakata, K.; Shindo, D, Characterization of Hematite Particles of Different Shapes. *J. Colloid. Interface Sci.* **1993**, 158, 420-428.

9. Morales, M.P.; González-Carreño, T.; Serna, C.J. The Formation of Alpha-Fe2O3 Monodispersed Particles in Solution. *J. Mater. Res.* **1992**, 7, 2538-2545.

10. Ocaña, M.; Morales, M.P.; Serna, C.J. The Growth-Mechanism of Alpha-Fe2O3 Ellipsoidal Particles in Solution. *J. Colloid. Interface Sci.* **1995**, 171, 85-91.

11. Almeida, T. P.; Fay, M.V.; Zhu, Y. Q.; Brown, P. D. A Valve-Assisted Snapshot Approach to Understand the Hydrothermal Synthesis of Alpha-Fe_2O_3 Nanorods. *CrystEngComm* **2010**, *12*, 1700-1704.

12. Sugimoto, T.; Muramatsu, A.J. Formation Mechanism of Monodispersed Alpha-Fe_2O_3 Particles in Dilute $FeCl_3$ Solutions. *Colloid. Interface Sci.* **1996**, 184, 626-638.

13. Sugimoto, T.; Wang, Y.; Itoh, H.; Muramatsu, A. Systematic Control of Size, Shape and Internal Structure of Monodisperse Alpha-Fe_2O_3 Particles. *Colloids and Surfaces A* **1998**, 134, 265-279.

14. Lutterotti, L. Total Pattern Fitting for the Combined Size-Strain-Stress-Texture Determination in Thin Film Diffraction. *Nuclear Inst. and Methods in Physics Research, B*, **2010**, *268*, 334-340.

15. Post, J.E.; Heaney, P.J.; Von Dreele, R.B.; Hanson, J.C. Neutron and Temperature-resolved Synchrotron X-ray Powder Diffraction Study of Akaganeite. *Am. Min.* **2003**, *88*, 782-788.

16. Blake, R.L.; Hessevick, R.E. Refinement of the Hematite Structure. *Am. Min.* **1966**, *51*, 123-129.

17. Christian, J.W. *The Theory of Transformations in Metals and Alloys, 3ʳᵈ Edition*; Pergamon: New York, 2002; pp 546.

18. Penn, R.L.; Banfield, J. F. Imperfect Oriented Attachment: Dislocation Generation in Defect-Free Nanocrystals. *Science* **1998**, 281, 969-971.

19. Penn, R.L.; Erbs, J.J.; Gulliver, D.M. Controlled Growth of Alpha-FeOOH Nanorods by Exploiting-Oriented Aggregation. *J. Crystal Growth* **2006**, 293, 1-4.

20. Navrotsky, A.; Mazeina, L; Majzian, J. Size-Driven Structural and Thermodynamic Complexity in Iron Oxides. *Science* **2008**, 319, 1635-1638.

21. Penn, R.L.; Banfield, J.F. Formation of Rutile Nuclei at Anatase {112} Twin Interfaces and the Phase Transformation Mechanism in Nanocrystalline Titania. *Am. Min.* **1999**, 84, 871-876.

22. Huang, F.; Gilbert, B.; Zhang, H.Z.; Banfield, J. F. Reversible, Surface-Controlled Structure Transformation in Nanoparticles Induced by an Aggregation State. *Phys. Rev. Lett.* **2004**, 92, 155501.

23. Goodell, C.M.; Gilbert, B.; Weigand, S.J.; Banfield, J.F. Kinetics of Water Induced Structural Transformation in ZnS Nanoparticles. *J. Phys. Chem. C* **2008**, 112, 4791-4796.

24. Penn, R.L.; Banfield, J.F. Morphology Development and Crystal Growth in Nanocrystalline Aggregates under Hydrothermal Conditions: Insights from Titania. *Geochim. Cosmochim. Acta* **1999**, 63,1549-1557.

25. Niederberger, M.; Coelfen, H. Oriented Attachment and Mesocrystals: Non-Classical Crystallization Mechanisms Based on Nanoparticle Assembly. *Phys. Chem. Chem. Phys.* **2006**, 8, 3271-3287.

26. Addai-Mensah, J.; Prestudge, C.A. Structure Formation in Dispersed Systems. In *Coagulation and Flocculation*; Stechemesser, H; Dobias, B; Eds. CRC Press. 2005.

27. Kremer, J.R.; Mastronarde, D.N.; McIntosh, J.R. Computer Visualization of Three-Dimensional Image Data Using IMOD. *J. Struct. Biol.* **1996**, 116, 71-76.

28. Agulleiro, J.I.; Fernandez, J.J. Fast Tomographic Reconstruction on Multicore Computers. *Bioinformatics* **2011**, *27*, 582.

29. Kaynig, V.; Fuchs, T.; Buhmann, J. M. Neuron Geometry Extraction by Perceptual Grouping in ssTEM Images. In *2010 IEEE Conference on Computer Vision and Pattern Recognition (CVPR)*; **2010**; pp. 2902–2909.

30. Jiang, J. Q.; Graham, N. J. D. Observations of the Comparative Hydrolysis/Precipitation Behaviour of Polyferric Sulphate and Ferric Sulphate. *Water Res.* **1998**, 32, 930-935.

Chapter 5: Energetics of Akaganeite Nucleation Clusters Determined by *in situ* Small Angle X-ray Scattering Studies of Nucleation and Growth

Nucleation and crystal growth are fundamental processes with great importance for describing mineral precipitation, materials synthesis, and nanoparticle generation. Despite this, there remain important cases, such as the aqueous precipitation of oxyhydroxides, where the quantitative links between experimental results and theoretical rates of nucleation have remained elusive. Reliable values for the interfacial tension of the precipitate are needed for predicting the precipitation pathway, but these are often unavailable.

In this work, the precipitation of β-FeOOH (akaganeite) nanoparticles from acidic (pH 1.5-3) FeCl$_3$ solutions by thermal hydrolysis is tracked using *in situ* small angle x-ray scattering (SAXS). This process creates highly monodisperse particles, whose size, shape, and nucleation rate can be tuned by varying solution saturation and temperature. Precipitation modeling using classical nucleation theory allows us to determine the interfacial tension of the precipitate.

Within the experimental conditions, the interfacial tension of the β-FeOOH nucleus ranges from 0.06 to 0.12 J/m^2, and it shows a strong pH dependence is consistent with a protonated surface. An expression for the interfacial tension is presented that can be applied to ensembles of clusters with arbitrarily small size. This construction can be used to define an interfacial tension for the monomeric iron species, as well as the clusters involved in nucleation. Experimental results show that the interfacial tension of the critical nucleus is consistent with values derived from the thermodynamic stability of aqueous clusters. Furthermore, an analysis of nucleation rates shows that the critical nuclei contain just 4 to 30 iron atoms at the onset of precipitation, suggesting that this oxyhydroxide precipitation process is operating near the edge of the classical nucleation regime.

5.1 Introduction

The nucleation and growth of nanoparticles is a problem of broad scientific and engineering importance. The precipitation process impacts final crystalline phase, particle size distribution, and particle reactivity. Fine control over the precipitation process is needed to generate monodisperse nanoparticles for technological applications.

Historically, most precipitation processes are understood via classical theories of nucleation. These theories posit that forming a new particle requires overcoming an energy barrier associated with generating new interfaces. Such theories are well established, and have been used to describe diverse systems, such as condensation of vapors and crystallization of metals,[1,2] and they provide the basis for fine control of nanoparticle precipitation. [3,4] Additionally, the classical nucleation theory establishes a strong relationship between nucleation rate and interfacial energy that has been used to determine the interfacial energy of many phases.[5,6]

There have been numerous challenges and complexities, however, in describing the nucleation of metal oxyhydroxides such as FeOOH from aqueous solutions. Ferric iron is sparingly soluble and displays a complex solution chemistry involving multiple hydrolysis states and polymeric species.[7] There are also several solid phases which may form (e.g. ferrihydrite, goethite, akaganeite, and hematite). The first-formed phase depends upon temperature, pH, saturation, and

counter-ion identity,[8] but there is not a comprehensive understanding of why one phase is preferred over another. It is commonly assumed that the first formed phase is determined by its lower interfacial energy,[9] and new theoretical models for two-stage iron oxyhydroxide precipitation have been developed on this assumption.[10] However, these models are somewhat speculative, as the precise values of interfacial energies that would be needed to test these models and compare experimental results theoretical models are unknown. Furthermore, the mechanism and kinetics of crystal growth may play a role in determining which phases form and these may be quite complex. Molecular attachment to a growing solid may involve a competition between olation and oxolation condensation reactions,[12] and may even include non-classical growth mechanisms such as particle aggregation.[11]

Historically, nucleation models have been dependent on rough proxies for the nucleation rate such as 'induction time'.[12] These are not generally sufficient to describe the precipitation of materials such as iron oxyhydroxide, because of the complexities described above.

The aim of this study is to determine the fundamental parameters that control iron oxyhydroxide nucleation. The interfacial energy (interfacial tension) of the β-FeOOH nucleation clusters is one of the most important parameters to determine, because the nucleation rate is extremely sensitive to interfacial energy. The interfacial energy is obtained by establishing a quantitative relationship between solution saturation, pH, temperature, and nucleation rates; then modeling the nucleation process with classical nucleation theory. Previous, commonly cited measurements for iron oxyhydroxide interfacial energies are based on calorimetric measurements of the interfacial enthalpy and were determined for interfaces with vacuum or water vapor.[9,13] These values will not generally apply during conditions of nanoparticle nucleation, since the iron oxyhydroxide surface undergoes acid-base interactions in aqueous solution, and the interfacial tension may depend strongly upon pH.

This study focuses on the batch precipitation of β-FeOOH nanoparticles via thermal hydrolysis of aqueous $FeCl_3$ solutions. β-FeOOH particles are of interest due to their self-assembly capabilities,[14] their role as precursors to the formation of nanostructured hematite,[15,16] their potential as industrial catalysts[17] and their natural occurrence in geothermal systems.[18] This system is ideal for exploring nucleation and growth processes, because the hydrothermal precipitation process produces particles with well-defined size and shape, and the particle nucleation rates can be easily varied by changing the $FeCl_3$ concentration and reaction temperature.[19,20] Such well controlled processes are needed in order to develop quantitative models for the nucleation rate. The hydrothermal process allows for more precise control than base-induced hydrolysis, in which local concentration gradients in the reactants may lead to near-instantaneous precipitation of poorly crystalline products.[12]

Recent work has demonstrated that homogenous nucleation and growth from aqueous solutions can be characterized with time-resolved, *in situ* small angle x-ray scattering (SAXS). Previous SAXS studies have addressed the nucleation of Stöber silica particles,[25,26] and the nucleation of gold nanoparticles[27,28] and studies on the growth kinetics of nanoparticles in solution.[29]

SAXS allows for direct measurement of particle size, mass precipitated, and number of particles precipitated. Thus, time-resolved SAXS allows for a comprehensive description of the precipitation process. By performing a series of experiments, it is possible to show now nucleation and growth rates depend upon solution chemistry, supersaturation, and temperature.

Interpretation is aided with complimentary transmission electron microscopy and thermochemical speciation calculations. Apparent activation energies for growth can be obtained, and it is possible to determine the size of the nucleation barrier and the interfacial energy of the nucleus via classical nucleation modeling.

This approach provides the first truly quantitative description of classical homogenous nucleation rates in the iron oxyhydroxide system. Such descriptions should prove useful for improving nanoparticle synthesis procedures, but they also provide the thermodynamic values that are needed to test classical nucleation theories, and begin to understand the molecular-scale processes involved in oxyhydroxide nucleation.

5.2 Experimental Design and Methods

β-FeOOH nanoparticles are generated by thermally induced hydrolysis of $FeCl_3$ aqueous solutions with initial concentrations of 5, 10, 20, 50, 100, 200, 400, and 800 mM $FeCl_3$. The 800 mM $FeCl_3$ stock solution is prepared from analytical grade $FeCl_3 \cdot 6H_2O$ and deionized water, and filtered to 0.2 μm. Other samples are prepared by serial dilution with deionized water. $FeCl_3$ solutions of 20 mM or less are unstable at room temperature and are diluted less than 30 minutes prior to the experiment. Stock solutions are prepared less than 48 hours prior to use. The precipitation experiments are performed in batch reactions, with solutions held in a 2 mm diameter Kapton tube, supported by a copper sample holder. Precipitation is initiated by placing the sample holder into a preheated, temperature controlled copper block. Reactions were performed at 47, 57, 62, 67, 73, and 80 °C.

The precipitation process was tracked *in situ* with small angle x-ray scattering (SAXS), which provides time resolved measurements of particle size (radius of gyration), and precipitate volume. Experiments were performed at Lawrence Berkeley National Labs, Advanced Light Source, beamline 7.3.3, with 10 keV photons in transmission mode and a Pilatus 1M detector. The experimentally observed scattering range depended upon detector path-length, which is calibrated by silver behenate standard. A 3.8 m path-length provided a scattering range of q_{min} = 0.0041 Å^{-1} to q_{max} = 0.21 Å^{-1}, best for large particles. In other experiments, a 1.3 m path-length provided a scattering range of q_{min} = 0.013 Å^{-1} to q_{max} = 0.60 Å^{-1}, best suited for small particles. SAXS measurements are initiated approximately 50 seconds after insertion, and repeated at intervals of 10-60 seconds.

Table 1: Small Angle X-Ray scattering sample matrix.

	5 mM	10 mM	20 mM	50 mM	100 mM	200 mM	400 mM
47	X		X			X	
57	X	X	X	X	X	X	
62			X			X	
67	X	X	X	X	X	X	X
73	X		X			X	
80	X	X	X	X	X	X	X

SAXS scattering data is radially averaged to produce 1-D scattering profiles, $I(q)$, using Irena[24] and the particle scattering signal was isolated by subtracting an appropriate background pattern. Details are provided in supplemental materials.

The SAXS scattering patterns were processed to obtain precipitated volume fraction and particle size. Particle volume was obtained by calculating the Porod invariant, defined as $Q = \int_0^{q_{max}} I(q)q^2 dq$, which is directly proportional to the volume precipitated.[21] Example Kratky plots and discussion of the integration limits for determining the invariant are provided in supplemental materials.

The particle sizes were estimated via Guinier analysis,[22] in which the particle radius of gyration, R_g, is obtained by calculating low-q slope of the Guinier plot (i.e. $\ln(I(q))$ vs q^2). Details of this analysis and sample plots are provided in supplemental materials.

On conclusion of SAXS experiments, samples were removed from the copper sample holder and allowed to cool to room temperature. Selected TEM samples were prepared by applying 2 µL of solution to a TEM grid, blotting to remove excess solution, and air drying. TEM observations were performed using a Phillips CM200 operated at 200 keV to document particle size, shape, and crystalline structure. Particle size distributions and aspect ratio were obtained by manual counting of particles from TEM images.

Complimentary experiments were performed to determine the equilibrium solubility of β-FeOOH, for each initial concentration. 5 mL samples of $FeCl_3$ solutions were placed in sealed glass vials, placed in an oven for 24 hours at 80 °C, and allowed to precipitate to reach equilibrium. The supernatant solution was obtained by filtering with a 0.1 µm Supor filter, and the iron concentration remaining in the supernatant was measured by 600 nm UV-Vis adsorption with a "ferron" assay.[23] Initial and final pH also measured with Ag-AgCl electrode.

Thermodynamic properties and chemical speciation of the aqueous solution were determined by with Visual MINTEQ 3.0 thermochemical calculations. The thermodynamic parameters for iron complexes are taken from the MINTEQ thermodynamic database, which was derived from iron speciation calculations in $FeCl_3$ solutions by Liu and Millero, and Martell.[31,32] (See supplementary materials for equilibrium constants used). Activity coefficients are calculated using the Davies activity model. MINTEQ is used to estimate the pH, aqueous speciation, and chemical activity of each species as a function of initial $FeCl_3$ concentration, temperature, and the amount of precipitated FeOOH. Calculations assume an idealized dissolution reaction of β-FeOOH → $Fe^{3+} + 2H_2O - 3H^+$, which neglects incorporation of Cl^- into the β-FeOOH structure. The solubility constant for β-FeOOH was determined to have a value of $\log(K_s)$= 2.3, based on the ferron assay experimental results, while the enthalpy of formation for β-FeOOH is taken from Mazeina *et al.*, as -554.7 kJ/mol,[13] which corresponds to an enthalpy for the dissolution reaction of -65.4 kJ/mol.

5.3 Results

5.3.1 TEM Observations
High resolution TEM images with lattice fringe imaging, Figure 2, shows that particles consist of β-FeOOH (Akaganeite, space group I 2/m). Particle elongation is along the [010] axis. When

viewed down this axis, the particles are found to have a square cross-section, terminated on the (100) and (001) planes. 0.707 nm lattice fringes, corresponding to the (101) and (10$\bar{1}$) planes are clearly visible from both end-on and side views.
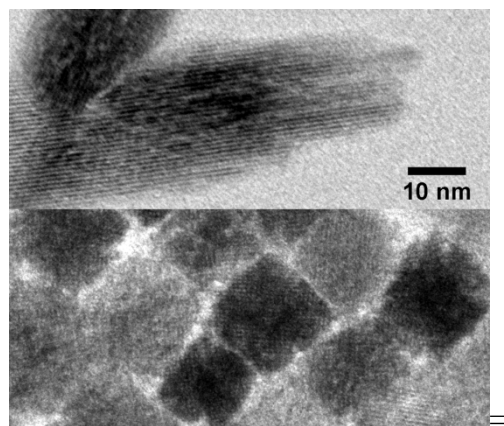
Figure 1: High resolution TEM images, both obtained at 150 kX magnification. Top: side view of a twinned particle synthesized from 100 mM FeCl3 at 67 °C. Prominent (101) fringes are visible. Bottom: Particles synthesized from 200 mM FeCl3 at 67 °C., packed into a 2-D colloidal crystal. Particles are viewed down the [010] (long) axis, and the square cross section terminated by the (100) and (001) faces is visible. The (101) and (10$\bar{1}$) lattice fringes can be seen.
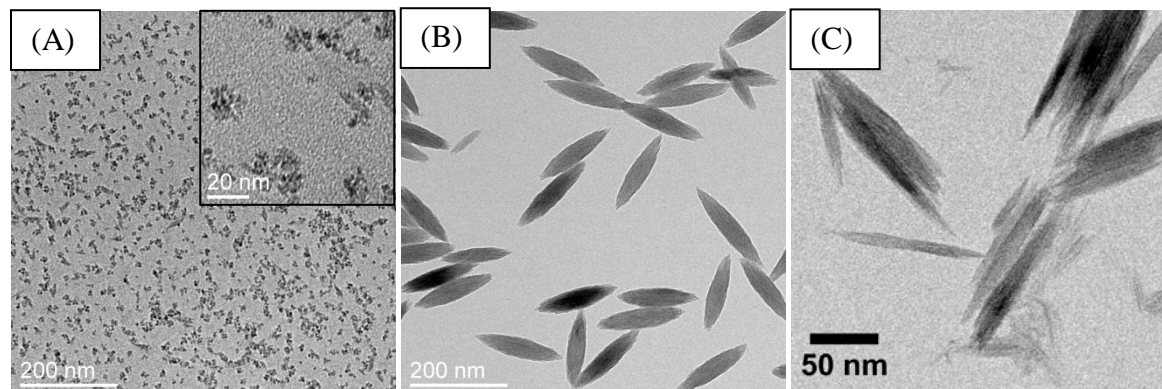
Figure 2: TEM images of nanoparticles precipitated at (A) 5 mM FeCl$_3$, 47 °C (B) 100 mM FeCl$_3$, 57 °C (C) 400 mM, 67 °C.

Particle shape and size depends strongly upon initial FeCl$_3$ concentration, Figure 2. At low initial concentrations, the morphology is poorly defined and size distributions are relatively polydisperse. The largest and most uniform particles are obtained at intermediate concentrations of 50-200 mM. These particles have well defined (100) and (001) surfaces, seen clearly in end-on TEM views (Figure 1), but show a gradual tapering toward the particle ends. At 50 mM and 100 mM, particle intergrowths are common (see upper right corner of Figure 2 (B)). These appear to form at special twinning angles, with a rotation of either 66° or 90° about the [100], [001],[10$\bar{1}$] or [101] axes. After extended aging, the particles formed from 100 mM, 200 mM, and 400 mM solutions form raft like aggregates, eventually self-organizing into two dimensional supercrystals with particles stacked parallel along the [010] axis into a disordered square lattice (Figure 1). At 400 mM initial concentration, particles show an almost needle-like morphology.

69

However, the very finest needles observed in Figure 2 (C) are most likely formed during sample drying.

TEM particle counting is performed to quantitatively assess the average particle size and aspect ratio. The radius of gyration was estimated according to the equation $2R_g = \sqrt{length^2/5 + 2\,width^2/5}$. Results are displayed in Table 2. The largest particles are generated in 100 and 200 mM samples. Particle aspect ratio increases dramatically with initial $FeCl_3$ concentration and decreases slightly with temperature.

Table 2: Summary of particle size (mass-averaged R_g), and aspect ratio (AR), obtained by TEM particle measurement at the conclusion of SAXS experiments.

		47 °C	57 °C	67 °C	80 °C
5 mM	R_g (nm)	4.0	2.6		
	AR	1.4	1.2		
10 mM	R_g (nm)		4.2		2.9
	AR		1.7		1.4
20 mM	R_g (nm)	44	27	7.0	4.8
	AR	2.9	2.6	2.6	2.0
50 mM	R_g (nm)			10.4	5.9
	AR			3.6	2.1
100 mM	R_g (nm)		43	47	49
	AR		4.3	4.8	3.6
200mM	R_g (nm)			23	60
	AR			5.2	4.3
400 mM	R_g (nm)			33	
	AR			9.9	

5.3.2 Aqueous Speciation and Solubility

In order to confirm the solubility of β-FeOOH, ferron assay measurements were used to measure the supernatant iron concentration and determine how much iron precipitates from solution at 80 °C. These results are shown in Figure 3. Solubility depends on initial $FeCl_3$ concentration. 96% of the Fe precipitates from a 5 mM $FeCl_3$ solution, while only 17% of Fe precipitates from the 200 mM solutions. This is because iron hydrolysis makes the higher $FeCl_3$ solutions very acidic, allowing more iron to remain dissolved. MINTEQ calculations can be used to predict the equilibrium fraction precipitated, if the solubility constant for β-FeOOH is known. The best agreement between experiment and prediction occurs when $\log(K_s) = 2.3$, at 25 °C. This is in good agreement with literature values; the free energy of dissolution from Mazeina *et al.*[13] corresponds to $\log_{10}(K_s)$ of 2.0 at 25 °C. As expected, β-FeOOH is slightly more soluble than goethite or hematite phases and less soluble than ferrihydrite[33]. Note that the enthalpy of dissolution for β-FeOOH is negative, so that the solubility decreases with increased temperature.
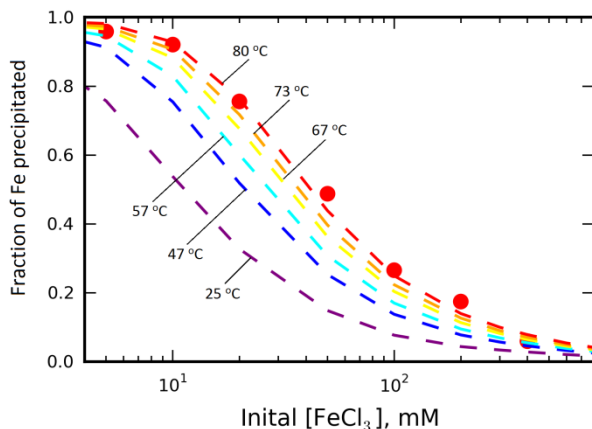
Figure 3: Red circles show ferron assay measurements of the fraction of Fe that precipitates after aging at 80 °C, for solutions with initial FeCl3 concentrations between 5 and 200 mM. Dashed lines show the corresponding MINTEQ predictions of precipitated volume fraction, at temperatures of 25 to 80 °C, assuming a 25 °C solubility constant of log(K_s)= 2.3, and an enthalpy of reaction of -65.4 kJ/mol.

Having determined the solubility of β-FeOOH, MINTEQ models can be used to calculate the solution saturation as a function of temperature, concentration, and degree of reaction. The saturation parameter is defined as $\sigma = \ln(\{Fe^{3+}\}/\{H^+\}^3) - \ln(K_s)$. Later, this saturation parameter will be used to determine the driving force for nucleation during a precipitation reaction. Figure 4 maps the initial solution saturation as a function of concentration and temperature. Iron salt solutions display two atypical behaviors worth noting. The saturation increases with temperature, and the acid-base chemistry of ferric iron causes a minimum to occur at intermediate concentrations of 100-200 mM FeCl3. As precipitation proceeds from any initial state, the saturation will drop until equilibrium is reached at $\sigma = 0$. This response is important for determining the number of particles nucleated, because nucleation rates depend sensitively on σ, and will decrease dramatically as the saturation drops. Selected curves showing the response of the saturation to precipitation are displayed in supplementary materials.
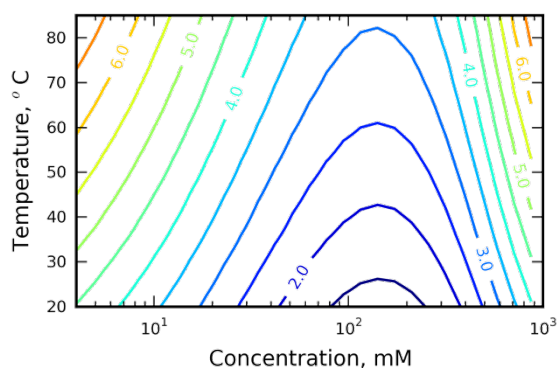
Figure 4: Contour plot showing the initial saturation parameter, σ (with respect to akaganeite), as a function of temperature and concentration, prior to precipitation. This value is calculated with MINTEQ, assuming log(K_s) = 2.3 at 25 °C, and dissolution enthalpy of -65.4 kJ/mol.

5.3.3 SAXS Precipitation Curves

Figure 5 shows two representative time series of SAXS scattering profiles for precipitation from 5 mM, and 100 mM FeCl3 solutions at 67 °C. Each curve represents a single timepoint, with

71

measurements taken at 10 second intervals. Over time, the total scattering intensity increases, reflecting an increase in precipitated volume, and there is a general shift toward scattering at smaller angles (lower *q*-values), which reflects increasing particle size. Several higher order scattering lobes are visible in the 100 mM sample. These indicate that the particles have a very well defined shape and narrow size distribution. The scattering profile of the 5 mM sample extends to higher q-ranges, indicating a smaller average particle size, while the lack of higher order oscillations indicates a broader distribution of sizes and shapes.
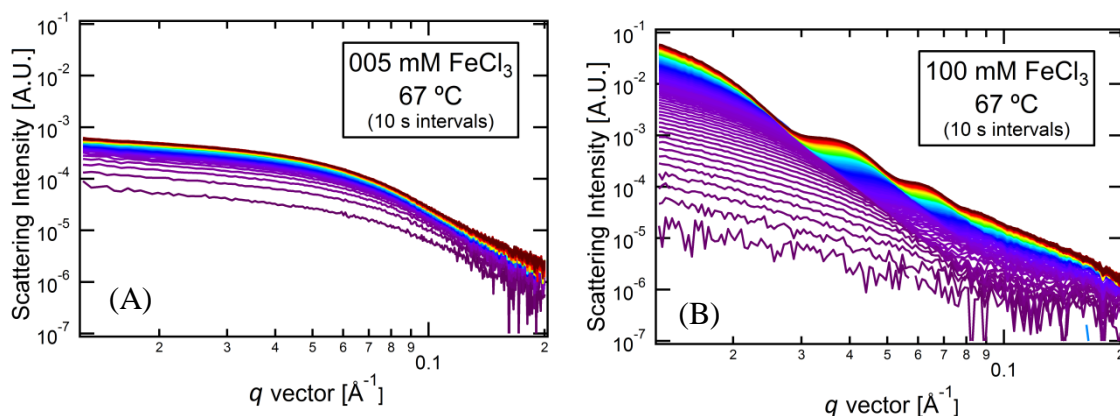
Figure 5: SAXS scattering profiles of nanoparticle precipitation. (A) for from 5 mM FeCl₃ (B) 100 mM FeCl₃. Both datasets are obtained at 67 °C. Each curve corresponds to one timepoint, obtained at 10 s intervals.

The Porod invariant is calculated to determine mass precipitated (reported as either the molar concentration β-FeOOH, or as the suspension volume fraction, ϕ) while the Guinier analysis is used to determine average particle size. Some representative curves for precipitated volume and particle size as a function of time are given in Figure 6, while curves from additional sample conditions, as well as complimentary information such as the apparent number of particles formed are provided in the supplementary materials.
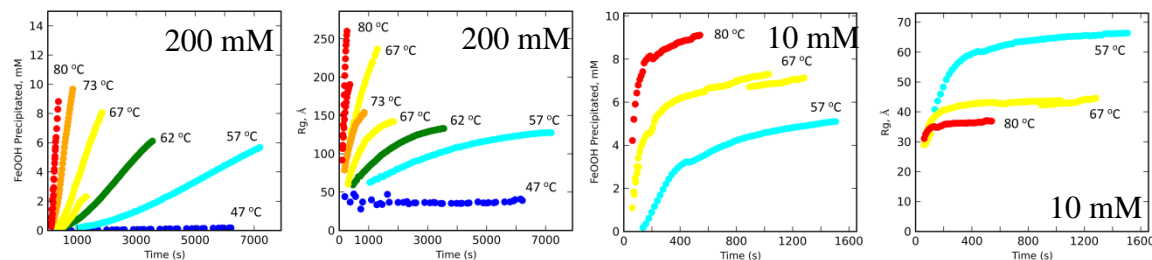
Figure 6: Mass precipitation curves obtained from SAXS invariant, and particle size curves obtained by Guinier analysis, at two representative concentrations.

The apparent number of particles formed is roughly estimated as $N_{app} = \phi/(\alpha R_g^{3})$. The symbol α represents a geometrical factor that relates R_g^{3} to particle volume. Its value depends upon particle aspect ratio, which has been estimated from TEM observations (Table 2). Treating the particles as spheroidal:

Equation 1

$$\alpha = \frac{4\pi AR}{3} \left(\frac{2 + AR^2}{5} \right)^{-3/2}$$

Note that for real suspensions, N_{app} will be less than the actual number of particles by factor that depends on the suspension polydispersity. This is because the Guinier measurement of R_g is more sensitive to large particles than small particles. After nucleation ends, continued growth may cause the suspension to become less polydisperse (the average particle size increases more quickly than the distribution breadth). Thus the apparent number of particles may continue rise while the actual number of particles remains constant.

Figure 6 includes precipitation curves from 200 mM FeCl$_3$, at temperatures between 47 °C and 80 °C. Multiple curves are shown for certain experiments (80°C and 67 °C), which were repeated on different days. Absolute precipitation rates differ slightly between days, but general trends are consistent. Precipitation is dramatically faster at high temperatures. During the early growth stages, new particles are being formed directly from solution. Despite rapid nucleation, the initial volume-precipitation rates are limited by the availability of growth surfaces; precipitation accelerates as new particles (and surfaces) are formed. When the quantity of precipitate passes a few mM of FeOOH, the supersaturation drops enough that particle nucleation ceases, and the number of particles stabilizes at a constant value. These particles continue to grow, and the growth rates gradually slow as equilibrium is approached. Unfortunately, it is not always possible to track the reaction to completion. Time constraints make this unfeasible in some cases, and for concentrations above 100 mM, the formation of self-assembled colloidal crystals makes this impossible.

Figure 6 also shows precipitation curves from 10 mM FeCl$_3$, which is representative of the lower concentration samples. At these lower concentrations, the initial nucleation rates are much more rapid, and the formation of new particles is over quickly. Even at the relatively cool reaction temperature of 57 °C, the apparent nucleation stage has largely ended after about 300 seconds. Continued precipitation after nucleation stops is driven by particle growth. In these low concentration samples, the initial nucleation rate and number of particles formed depends strongly upon temperature, with higher temperatures generating more and smaller particles. Because fewer particles form in the low temperature cases, there is less competition for growth material and particles eventually reach a larger size.

5.3.4 Particle Growth Rates
Although the primary goal of this study is to determine nucleation rates, the period of active nucleation depends sensitively upon growth kinetics. (Particle growth leads to a reduction in supersaturation, which subsequently leads to a reduction in both nucleation rates and growth rates). Thus, a reliable description of the growth rate is needed to constrain and model the nucleation rate. In this paper, the growth rate is defined with respect to the rate of change in the radius of gyration, as $v = \dot{R}_g$. In Figure 7, the growth rate is plotted versus the 'degree of reaction', defined as $x = \phi/\phi_{eq}$ for each concentration. Here, ϕ_{eq} is the volume fraction of β-FeOOH for a sample at equilibrium (calculated with MINTEQ). Neglecting Ostwald ripening, the growth rate should go to zero as x approaches 1. The solid lines in Figure 7 represent experimental measurements of growth rate, which have been smoothed by binning with respect

to the degree of reaction. There is no strong evidence for particle size effects on the growth rate. The growth rate appears to decay exponentially with respect to degree of reaction, and shows a strong Arrhenius type temperature dependence. A least squares fitting approach is used to develop an empirical rate law for growth is determined at each concentration.

Equation 2

$$v = v_0 \exp(-C \cdot x) \exp(E_a/RT)$$

A summary of the fit parameters for each concentration is provided in Table 3, and the fit results are shown in Figure 3 as dashed lines. Extrapolated initial growth rates are on the order of 0.01-10 Å/s for all concentrations. The apparent activation energies for growth are quite large, between 140 and 200 kJ/mol, depending upon solution chemistry. The highest activation energies are seen at concentrations of 50-200 mM, which is roughly correlated with the lowest degree of supersaturation.
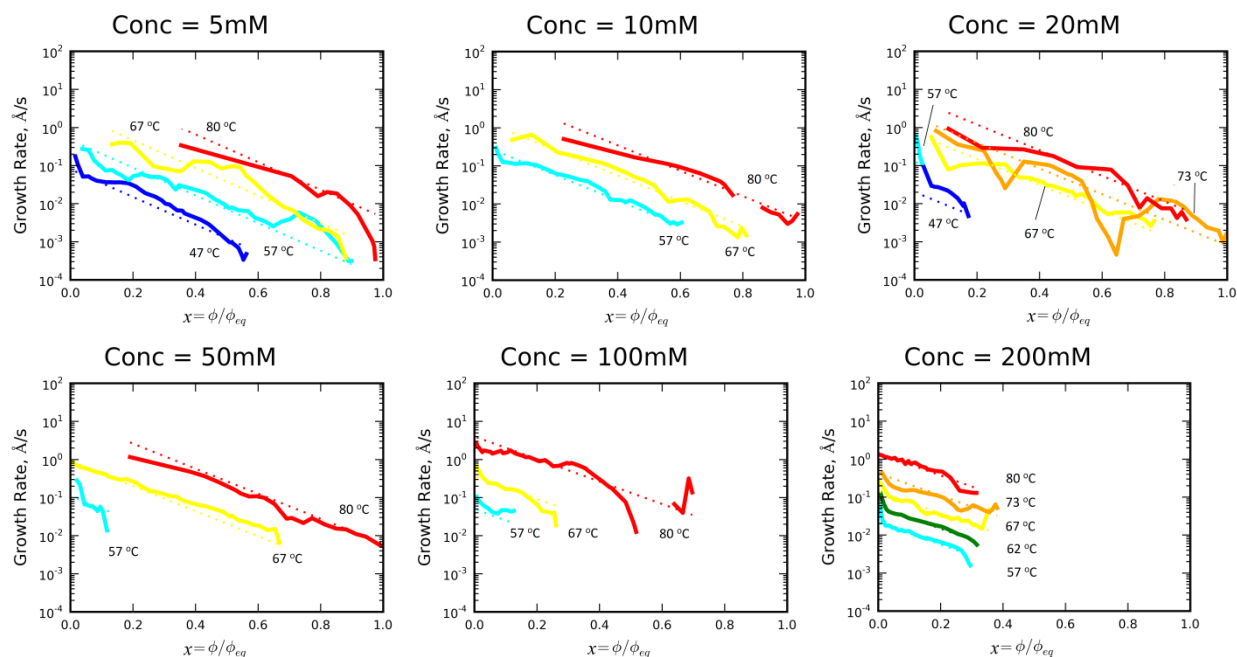
Figure 7: Growth rates, as a function of degree of reaction. Solid lines are smoothed experimental data. Dashed lines are multidimensional fits, used to obtain decay parameter, and apparent activation energy (Red: 80 °C, Orange: 73 °C, Yellow: 67 °C, green: 62 °C, cyan: 57 °C, blue: 47 °C.)

Table 3: Growth Rate Parameter Fits

[FeCl$_3$], mM	v_0, m/s	E$_a$, kJ/mol	C
5	$1.7 \cdot 10^{24}$	155	8.4
10	$4.6 \cdot 10^{21}$	140	7.7
20	$2.9 \cdot 10^{24}$	160	7.8
50	$1.9 \cdot 10^{30}$	197	7.6
100	$8.9 \cdot 10^{27}$	185	6.8
200	$1.9 \cdot 10^{26}$	177	6.8

The apparent activation energies for growth are quite high, approximately 10 times greater than that for diffusion in water. This suggests a reaction-controlled growth mechanism,[34] as opposed to a simple diffusion controlled growth mechanism.

The growth rates have been modeled as a function of the degree of reaction, x, because this is convenient for precipitation modeling, and it allows an overall apparent activation energy for growth to be highlighted. It would also be possible, and would perhaps be more physically meaningful to develop rate laws with respect to the concentration of various reactive species or with respect to the solution saturation. However, this approach was avoided, since it may imply knowledge of growth mechanism where none is firmly identified. The general growth mechanism may be a quite complex, including the formation of a reactive species in solution, the formation of a reactive surface site, attachment of the reactive species to the surface, and incorporation via oxolation or olation.[12] Considering the high apparent activation energies, each of these steps is likely to contribute to the apparent energy barrier in a coordinated process that involves many atoms.

5.4.5 Particle Nucleation
For each experiment, a curve has been measured that describes the apparent number of particles as a function of time (see supplemental materials). This curve was fit with a simple exponential function of the form $N_{app}(t) = N_{max} - N_{max}\exp(-t/t_{app})$, in order to estimate the total number of particles formed during each experiment, N_{max}, as well as the apparent nucleation timescale for nucleation, t_{app}. These results are summarized in Table 4. Because the impact of particle size polydispersity was neglected, these calculations will tend to underestimate the number of particles, and overestimate t_{app}. Nevertheless, clear trends can be observed. The number of particles varies widely, from $2 \cdot 10^{14}$ to $9 \cdot 10^{20}$ particles/m³. In Figure 8, N_{max} is shown as a function of concentration and temperature. By comparing Figure 8 with Figure 4, it is obvious that initial supersaturation has a strong correlation with the amount of nucleation. The most particles form from the highly supersaturated 5 mM solutions, while the least form in less saturated 100-200 mM solutions. In all cases, increasing the temperature leads to a shorter nucleation period. Under most conditions, high temperature nucleation is more vigorous, so that more particles are created. The exception is the 200 mM sample, where higher temperatures lead to fewer particles. This shows that supersaturation alone cannot explain the number of particles formed, but that other factors such as temperature, growth rate, and interfacial energy must also play a role. The detailed modeling of nucleation rates will be discussed in the following section. Results are not reported for 400 mM or 800 mM experiments, because the SAXS dataset was not sufficient to determine the particle size in these cases.
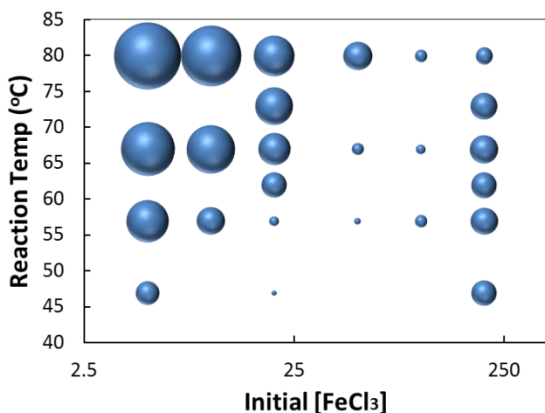
Figure 8: Each bubble represents an experiment performed the given temperature and concentration. The apparent bubble volume is proportional to N_{max} which is the (apparent) number of particles generated per unit volume for that experiment. Larger bubbles represent a greater number of particles.

Table 4: Apparent number of particles generated at the conclusion of the SAXS precipitation experiment, N_{max}, and time period for active (apparent) nucleation, t_{app}. If a range of numbers is given, this represents the range of results for multiple experiments.

		47 °C	57 °C	62 °C	67 °C	73 °C	80 °C
5 mM	N_{max}	$3.2 \cdot 10^{19}$	$1.6 \cdot 10^{20}$		$4.6 \cdot 10^{20}$		$7.7 \cdot 10^{20}$
	t_{app}	510 s	210 s		110 s		22 s
10 mM	N_{max}		$5.3 \cdot 10^{19}$		$2.5 \cdot 10^{20}$		$5.5 \cdot 10^{20}$
	t_{app}		290 s		40 to 60 s		40 s
20 mM	N_{max}	$3.1 \cdot 10^{17}$	$2 \cdot 10^{18}$	$4 \cdot 10^{19}$	$6.9 \cdot 10^{19}$	$1.4 \cdot 10^{20}$	$1.4 \cdot 10^{20}$ to $1.8 \cdot 10^{20}$
	t_{app}	5300 s	800 s	430 s	210 s	125 s	80 to 110 s
50 mM	N_{max}		$\sim 6 \cdot 10^{17}$		$3.0 \cdot 10^{18}$ to $3.0 \cdot 10^{18}$		$6.0 \cdot 10^{19}$
	t_{app}		>1400 s		500 to 530 s		90 s
100 mM	N_{max}		$4.4 \cdot 10^{18}$		$1.5 \cdot 10^{18}$ to $2.3 \cdot 10^{18}$		$4.0 \cdot 10^{18}$ to $4.4 \cdot 10^{18}$
	t_{app}		7000 s		800 to 2400 s		280 to 310 s
200mM	N_{max}	$4 \cdot 10^{19}$	$5.0 \cdot 10^{19}$	$4.1 \cdot 10^{19}$	$3 \cdot 10^{18}$ to $4.8 \cdot 10^{19}$	$4.7 \cdot 10^{19}$	$6.6 \cdot 10^{18}$ to $2.0 \cdot 10^{19}$
	t_{app}	-	5200 s	1740 s	600 to 1120 s	520 s	170 to 190 s

5.4 Calculations

5.4.1 Classical Nucleation Model

The particle nucleation rate is modeled using a simple variation on the classical nucleation theory originally developed by Volmer and Weber.[2] This theory is developed on the assumption that a population of iron clusters exists in solution, some of which are critically poised to form stable β-FeOOH particles. Molecular clusters that are smaller than the critical size are called embryos, and are statistically more likely to shrink than to grow, while larger clusters are more likely to grow and ultimately become stable nanoparticles. The critically poised clusters are referred to as nuclei. At steady state, the rate of particle nucleation is proportional to the number of critically poised nuclei, and the rate at which these nuclei can be stabilized by attachment of a molecule or ion from solution. The rate of nucleation, I, can be then be described by Equation 3.

Equation 3

$$I = A \exp\left(\frac{-\Delta G_c}{kT}\right)$$

76

Here, ΔG_c represents the free energy of formation for a critically poised nucleus, and is important in determining the number of critical clusters that are present in the system. In the classical nucleation theory, the free energy of formation for a cluster containing n atoms or molecules is commonly described using Equation 4. In this study, n is defined as the number of Fe atoms that a cluster contains. The first term, $-nkT\sigma$, describes the volumetric driving force that favors cluster formation, and is written in terms of the solution saturation. In this study, σ is estimated from MINTEQ calculations. (Since MINTEQ does not explicitly consider the formation of large clusters, this approach is only valid when clusters represent a small fraction of the total dissolved iron species, so that cluster formation doesn't significantly reduce the chemical potential of the reactants). In the second term of Equation 4, γ represents the interfacial tension, which is the thermodynamic work required to form new interface. For simplicity, the cluster is treated as spherical, so that a cluster with n Fe atoms has an interfacial area of $4\pi r_n^2$. Although large particles may possess a well-defined geometry and interfacial area, this is not necessary true of small clusters whose diameter is on the length scale of typical surface roughness features. Thus, no attempt is made to model the actual cluster geometry. Instead, the cluster geometry is defined using a Gibbs construction, an approach which is common to surface-thermodynamics. A spherical cluster containing n iron atoms is assigned a volume of nV_m/N_a (V_m is the molar volume of bulk β-FeOOH) such that the cluster will possess zero excess iron relative to a hypothetical reference system where the interior of this volume has the average properties of bulk β-FeOOH and the region surrounding this volume possesses the average properties of the resulting aqueous solution. Thus $r_n = (3nV_m/4\pi N_a)^{1/3}$. The supplementary materials provide a more complete discussion of this construction.

Equation 4

$$\Delta G_n = -nkT\sigma + 4\pi r_n^2 \gamma$$

During application of Equation 4, it is commonly assumed that γ is equivalent to the surface tension for a large, macroscopic interface between the same materials. However, the value of γ for very small clusters with high surface curvature may differ significantly from that of a macroscopic interface. Furthermore, the free energy of a cluster may also include energetic contributions that would not be accounted for by a macroscopic interfacial tension, such as the rotational and translational entropy gains associated with creating a free particle. There is significant debate in the literature about how free particle entropy should be accounted for in the classical nucleation theory,[2,30] but these contributions can be mostly be neglected for large clusters embedded in a fluid.

In order to minimize the free energy of the total system, the free energy cost of creating a nucleus must be balanced with the configurational entropy gains of creating a particle that can exist anywhere within the system. In the classical approach, the configurational entropy provided by a cluster of size n is approximately $k \ln(N_n/N_{tot})$, where N_n is the number of such clusters and N_{tot} is the total number of molecules in the system. N_{tot} is approximately 55.6 mol/L for aqueous systems. By minimizing the total free energy of the system, one obtains the standard Boltzmann distribution for estimating the equilibrium population of clusters, which is can be applied for clusters with size less than the critical size:

Equation 5

$$N_n = N_{tot} \cdot \exp\left(-\frac{\Delta G_n}{kT}\right)$$

This result is identical to the cluster distribution assumed by the Volmer-Weber formulation of classical nucleation theory. In reality, the Boltzmann distribution will not be attained because a nucleating system is not in equilibrium, but more sophisticated treatments of steady state nucleation kinetics, such as Becker-Döring theory predict only subtle differences from this distribution, and the Volmer-Weber approach is sufficiently accurate for our purposes. Continuing in the classical approach, if the value of the interfacial energy does not vary too strongly with cluster size, Equation 4 can be used to identify the cluster size with highest free energy of formation. This cluster corresponds to the critically poised nucleus, which has its radius and size given by Equation 6, and its free energy of formation is given by Equation 7.

Equation 6

$$r_c = \frac{2\gamma V_m}{RT\sigma}, \qquad n_c = N_A \frac{32\pi\gamma^3 V_m{}^2}{3(RT\sigma)^3},$$

Equation 7

$$\Delta G_c = \frac{16\pi\gamma^3 V_m{}^2}{3(RT\sigma)^2}$$

Equation 7 can be combined with

Equation 5 to estimate the population of critically poised nuclei. The preexponential factor, A, in Equation 3 must then describe how quickly these nuclei are converted into stable particles. Many theoretical models have been developed to estimate the magnitude of A, but these vary widely and are not reliable without a firmly established mechanism of cluster growth.[2,30] For the purposes of this study, it is simply proposed that attachment to a critical nucleus is analogous to the growth of small nanoparticles, so that v (which was measured for growth of small particles) provides a proxy for the rate of monomer attachment to the surface of a nucleus. This is performed under the assumption that particle growth is limited by the attachment of molecules to the surface, and that detachment rates are negligible. The resulting expression for A is proportional to the surface area of the critical nucleus, the particle growth rate, and the number of molecules in the system. Particle aspect ratio effects were neglected in this derivation, because the precise shape, size, and reactivity of the nucleus are unknown.

Equation 8

$$A = 4\pi r_c{}^2 \cdot \frac{N_A}{V_m} \sqrt{5/3} \, v \cdot \frac{N_{tot}}{V}$$

This provides values of $1 \cdot 10^{24}$ to $1 \cdot 10^{26}$ m^{-3}s^{-1} that are well within the range of expected values for similar systems.[1,12] This estimate could deviate from the actual value by several orders of magnitude, but this level of uncertainty can be tolerated, because our primary goal in nucleation modeling is to determine the interfacial energy, and the overall nucleation rate is far more sensitive to γ than A.

5.4.2 Precipitation Modeling

Equipped an empirical expression for the particle growth rate, $v(x)$; and a simple physical model for nucleation, a numerical precipitation model is developed, which can be used to replicate the experimental SAXS profiles. This is achieved by numerical solution of the following integral equation.

Equation 9

$$x(t) = \frac{1}{\phi_{eq}} \int_{t'=t_o}^{t} I(x)\, \alpha \left(\int_{t''=t'}^{t} v(x)\, dt'' \right)^3 dt'$$

In this equation, particles are generated at a rate, $I(x)$. A particle is nucleated at the time t' with the critical size, which is typically negligibly small, and will continue to grow with a rate, $v(x)$. The radius of gyration for that particle at a later time t is obtained by integrating, as $R_g(t) = \int_{t''=t'}^{t} v(x)\, dt''$, and the particle volume is equal to $\alpha \cdot R_g^3$. The total volume precipitated per unit volume, ϕ, is obtained by integrating over all the particles that have been nucleated. This can be converted to the degree of reaction, as $x = \phi/\phi_{eq}$. Solving Equation 9 numerically will provide the precipitation profile, $x(t)$, and at the same time it is possible to calculate complimentary information such as the particle size distribution.

In order to compare with experiment, this equation is solved numerically to determine the mass-average radius of gyration as a function of time, and hence the apparent number of particles, where $N_{app} = \phi/(\alpha\, R_g^3)$.

For modeling experimental data, all of the terms involved in Equation 9 have been developed. ϕ_{eq} depends upon initial solution concentration and temperature, and can be calculated using MINTEQ. The particle shape factor, α, is assumed to depend only on the initial $FeCl_3$ concentration, and is estimated using Equation 1 and the data in Table 2. The growth rate, $v(x)$, is known from experimental data, following Equation 2 and Table 3. Finally, the steady state nucleation rate, $I(x)$, is estimated using Equation 3. Important parameters that control the nucleation rate are the supersaturation, $\sigma(x)$, which is known from MINTEQ speciation models. The only unconstrained parameter for modeling the precipitation rates is the interfacial tension, γ. Thus, the interfacial tension can be obtained by comparing experimental results with the numerical models.

There are various ways in which a precipitation model's quality-of-fit can be ranked. In this study, the best-fit value for γ has been selected such that the apparent number of particles formed, N_{max}, will best match the experimental results listed in Table 4. This value does not always produce the best reproduction of the $R_g(t)$ or $x(t)$ curves, but considering that there is only one truly free parameter, the numerical model is able to replicate all aspects of the growth curves with remarkable fidelity. Discrepancies must result due to imperfect descriptions for the growth rate, imperfect geometrical models of the particle shape, imperfect reproduction of the particle size distribution, and systematic measurement errors in the measurement of R_g and x. However, the discrepancies are all within reason, and the fundamental behavior is captured. The supplementary materials contain all experimental precipitation curves, along with numerical modeling results.

Tn Figure 9 (A), the best estimates for γ are plotted for each temperature, as a function of initial solution chemistry. The results show that interfacial tension depends systematically on $FeCl_3$ concentration, and is lower in high $FeCl_3$ solutions (i.e. lower pH), and the interfacial tension increases slightly with temperature. The magnitudes of the interfacial tensions are between 0.06 and 0.14 J/m^2.

The total number of nuclei formed during an experiment depends primarily upon γ, but it also upon the nucleation preexponential factor, A. There is a high degree of uncertainty in the value of A, and so the best fits for γ have also been determined under the assumptions that A could be three orders of magnitude greater or smaller than the best estimate (following Equation 8). These additional results are provided in the supplementary information. The analysis confirms that nucleation rate depends far more sensitively to changes in γ than changes in A, so that even three orders of magnitude deviation in A can be accounted for adjusting γ by less than 20%. Even in the most extreme reasonably expected case, where molecular attachment to the nucleus is diffusion limited, and A takes on its maximum physically attainable values of approximately 10^{40} $m^{-3}s^{-1}$, the estimates for γ would show similar trends with respect to concentration, and would be no more than 40% greater than the best estimates that are plotted in Figure 9.

Having calculated γ, Equation 6 is then applied to estimate the size of the critical nucleus at the onset of nucleation. These results are shown in Figure 9 (B). Similarly, Equation 7 can be applied to determine the free energy of formation for the nucleus, which ranges from 40 kJ/mol to 70 kJ/mol. These values are only valid at the beginning of precipitation. As the reaction proceeds, the supersaturation will drop, causing the nucleus size and free energy of formation to increase.
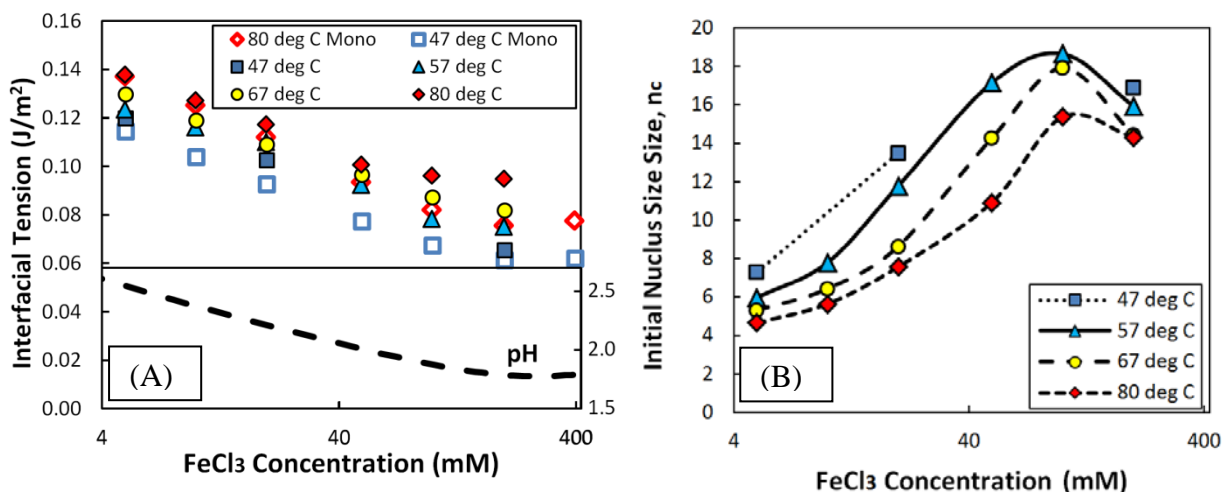
Figure 9: A) Filled symbols show the effective interfacial energies of the critical cluster plotted as a function of the initial $FeCl_3$ concentration, as estimated by modeling precipitation rates. For comparison, the open symbols represent the effective interfacial energy of an Fe_1 cluster at 47 °C and 80 °C, as estimated from thermodynamic stability data. Lower portion of the plot shows initial solution pH. B) Estimated number of iron atoms in the critical nucleus at the onset of precipitation.

5.4.3 Free Energy of Dissolved Ions
Previously established literature values for iron oxyhydroxide interfacial energy are not available in in low pH ranges. Instead, molecular scale solubility data provides the best check for

experimental values. There is historical precedent for this approach. Previous researchers have established strong correlations between the interfacial energies of solids and the energetics of free ions. For example, Grosse showed correlations between the surface energy of a liquid metal and its heat of vaporization,[35] while Nielsen and Söhnel[5] established a correlation between the hydration energy for ions and interfacial energy of their corresponding solids in aqueous systems. Later, Mersmann presented an excess interfacial energy construction that allowed the interfacial energy of an ionic solid to be estimated from knowledge of ion solubility.[6]

Because the thermodynamic construction for a cluster's free energy of formation (Equation 4) can be applied to arbitrarily small clusters (i.e., monomeric clusters, or clusters that contain just a few Fe atoms), it provides an easy means for comparing the energetics of embryonic oxyhydroxide clusters with those of small ionic species. Since it will be shown that the relevant nucleation clusters contain just a few Fe atoms, this must be true, or the classical nucleation theories could not be applied. In order to directly obtain interfacial energies, Equation 4 and

Equation 5 are combined. Solving for γ provides the following expression for interfacial tension of a cluster with size n (or an ensemble of different clusters with that size):

Equation 10

$$\gamma = \left(nkT\sigma - kT \ln \frac{N_n}{N_0} \right) / \ 4\pi r_n^2$$

This expression can be used to determine the interfacial energy for clusters of arbitrary size, including the monomeric species (a "cluster" of β-FeOOH with just one iron atom). Because r_n is defined with respect to an ideal reference volume of size nV_m/N_a there is no ambiguity regarding the interfacial area, although the physical properties of this interface will not necessarily reflect that of a bulk surface. For a given solution, MINTEQ speciation calculations provide the solution saturation with respect to β-FeOOH, and the concentration of monomeric iron species, which is obtained $N_1 = [Fe^{3+}] + [Fe(OH)^{2+}] + [FeOH^{2+}] + [Fe(OH)_3] + [Fe(OH)_4^-] + [FeCl^{2+}]$. Thus, Equation 10 can be combined with thermodynamic speciation calculations to easily determine the value of γ for a monomer.

In Figure 9 (A), the calculated of interfacial tension of the β-FeOOH monomers are plotted at both 47 and 80 °C, at each experimental concentration. (The value is calculated using initial $FeCl_3$ concentrations, prior to the onset of precipitation).The calculated interfacial tension of the monomer shows remarkable agreement with the experimentally determined interfacial tension of the nucleation clusters, both in terms of absolute magnitude and the trends with how with respect to $FeCl_3$ concentration and temperature.

An important observation, clearly demonstrated above in the discussion of the monomeric cluster, is that the cluster of size n does not correspond to just a single molecular entity. Rather, the cluster of size n consists of an ensemble of different clusters that each contain n Fe atoms, but which may potentially have different hydration states, protonation states, and structural conformations. Having more than one possible type of cluster increases the configurational entropy for the cluster of size n, and thus reduces the free energy of the particle ensemble (as well as reducing the effective interfacial tension of the cluster ensemble). Thus, the value of γ determined for such an ensemble does not represent a surface tension in the traditional mechanical sense, but still reflects a surface tension in the thermodynamic sense, in that it represents the work of creating an interface.

5.5 Discussion

5.5.1 Comparison with historical nucleation and growth modeling
This study has utilized classical nucleation and growth theories to model precipitation rates and subsequently determine the interfacial energies of the FeOOH nucleation clusters. This is possible because of the very strong dependence of nucleation rates upon interfacial energy.

The approach is inspired by the work of Nielsen and Söhnel[5] in which nucleation rates were used to determine the interfacial energies for a wide range of aqueous precipitates. However, these earlier studies had several limitations that prevented their application to iron oxyhydroxides. Nucleation rates were only roughly estimated using solution turbidity as a measure of "induction time", and this approach could not be successfully applied to characterize the precipitation of sparingly soluble salts. Many simplifying assumptions (*e.g.* diffusion limited growth rates) were also needed in order to obtain analytical solutions to the precipitation equation. In this study refines that approach by directly measuring particle size and particle growth rates with SAXS. The results show that growth rates are reaction limited, and a quantitative description of the growth rates allows for the entire precipitation process (including nucleation) to be modeled numerically from start to finish.

Several simplifying assumptions have been made. For example, the interfacial tension is assumed to remain constant throughout the course of the experiment, being only a function of the initial experimental conditions. This apparently contradicts the results, which show that γ is pH dependent, and that pH drops during the course of precipitation. However, even with pH dependent interfacial energies taken into account, the vast majority of nucleation is expected to occur during the onset of precipitation, and it is fair to assume that γ represents the interfacial tension at the initial experimental conditions. More sophisticated modeling may be possible, but are probably unnecessary in this system. A second major approximation, common in nucleation and growth modeling, is the use of theoretical expressions for nucleation rates that assume steady state nucleation. The transient processes associated with establishing and evolving an embryonic cluster distribution in response to changing solution saturation have not been considered. However, such effects are most significant for large critical clusters,[2] and are thus likely to be minimal in this system, where nuclei contain just a few tens of atoms.

5.5.2 Error Analysis
Estimates for γ are contingent upon use of a reasonable nucleation model and reliable values for σ, A, and v.

The overall nucleation rate is dependent upon the ratio of γ^3/σ^2. Error propagation suggests that a small error in the magnate of σ will result in corresponding, but slightly smaller errors in the magnitude of γ. Experimental measurements of particle solubility show good agreement with literature values, and the pH dependence of solubility shows good agreement with MINTEQ predicted trends (see Figure 3). This suggests that our approach of estimating σ from MINTEQ calculations is reliable. However, MINTEQ speciation calculations are extrapolated from dilute solution measurements, and there are uncertainties involved with activity corrections at high ionic strength, so supersaturation (and interfacial energy) estimates may be less reliable at higher $FeCl_3$ concentrations.

The preexponential factor, A, presents a large source of uncertainty for directly predicting nucleation rates, but has marginal influence on estimates of γ. Exact values for A are unknown, but are estimated on the assumption that growth of embryos and small particles are analogous. This assumption seems reasonable, and previous researchers have shown general correlations between the reactivity of molecular clusters and the reactivity of bulk mineral surfaces, for processes such as dissolution.[36] However, it has also been shown that molecular clusters transform via complex coordinated motions, with rates that may vary by orders of magnitude, depending upon the details of cluster structure.[37] Thus, it would not be surprising if the rates of attachment to embryo surfaces differed from the rates of attachment to bulk surfaces by several orders of magnitude. This level of uncertainty is tolerable; as the value of γ is robust with respect to large errors in the value of A. Three orders of magnitude error in A will produce errors in γ of only 10-20%.

Because growth rates, v, have been measured directly, large errors are not expected here. However, the numerical simulations, have utilized simple, imperfect models for the growth rate. Errors in these models make it impossible to simultaneously reproducing all aspects of precipitation with perfect accuracy (*i.e.* if growth rates are incorrect, it is not possible to simultaneously reproduce the nucleation rates and total mass precipitated). However, the growth modeling has still been able to reproduce the general character of the precipitation. As for the preexponential factor, moderate errors in v have rather small influence on estimates for γ.

Thus, estimates for γ should be quite robust. However, estimates for the size and free energy of formation for the nucleus are more sensitive to errors, and should be considered more tentative. This is because both n_c and ΔG_c are both proportional to γ^3, so that small errors in γ may be amplified.

5.5.3 Interfacial Tension Dependence on Solution Chemistry
The interfacial tensions obtained for the critical cluster are on the order of 0.05-0.12 J/m^2 and depend strongly upon the solution the cluster is in contact with. This result is significantly lower than commonly reported values for the excess interfacial enthalpy of dried iron oxyhydroxide surface or surfaces hydrated with water vapor, which exceed 0.4 J/m^2.[9] Within the experimental regime, it is found that lower pH results in significantly lower interfacial energies. All of these observations point to the importance of considering protonation state when discussing the interfacial energy of oxyhydroxides. The presence of chlorine may also impact interfacial energies, but this effect is likely secondary in importance. The interfacial tension increases slightly with temperature, suggesting entropic contributions to the interfacial tension. In fact, over the pH range studied, it is likely that the excess interfacial enthalpy is negative due to the high surface protonation, and the positive interfacial tension would be entirely entropic.

It is important to note that the interfacial tension of the critical nucleus may not be identical to that of bulk β-FeOOH. The ensemble of critically poised nuclei actually consists of small clusters, which may contain as few as 4 Fe atoms. Although such clusters may eventually grow and develop into β-FeOOH crystals, they are too small to be considered crystalline and they should not be expected to possess exactly the same structures, surface terminations, or interfacial tensions as a macroscopic β-FeOOH particle.

5.5.4 Nature of the Nucleus and Embryonic Clusters

In this study, the typical critical nucleus at the onset of precipitation is extremely small, between 4-20 iron atoms. Of course, as precipitation proceeds and saturation drops, the size of the nucleus will increase dramatically (at equilibrium, the critical nucleus will be infinitely large).

It is worth noting that for very small clusters and particles, the interfacial energy may be expected to vary with radius. This presents a challenge to the classical nucleation theory, in which the nucleus size and free energy of formation are derived under the assumption of a constant interfacial tension. The supplementary information contains a brief discussion of the complications introduced by variable interfacial tensions. Fortunately, our results show that the interfacial tension of the cluster similar to that of the monomeric dissolved species. Thus, it is reasonable to assume that interfacial tensions are relatively constant over the size range between the monomer and the nuclei, and the radius-dependence of the interfacial tension can be neglected for the purposes of nucleation modeling.

We then come to the question, what does the critical nucleus look like? Small nuclei will not possess crystal periodicities, and cannot truly be said to possess the structure of bulk β-FeOOH. Rather, the nucleus is merely collection of atoms, which is critically poised so that addition of a single molecule can set it on a trajectory toward becoming a stable β-FeOOH particle. Furthermore, the critical nucleus may not consist of a single structure, but there may be an ensemble of different structures that are all critically poised. The most important structures will be those with the lowest free energy of formation and hence greatest abundance, but the existence of alternate nucleus structures will add additional nucleation pathways and thus reduce the free energy cost of forming a nucleus.

In future research, it may be important to determine what characteristics besides size are important for determining whether a cluster has been sent on a trajectory toward becoming β-FeOOH. Because the early nuclei are so small, computational modeling may soon be able to explore this question, and reveal the structure, energetics, and reaction kinetics of the most important members of the critical nuclei ensemble.

5.5.5 Energy Barriers to Precipitation

In this work, two energetic barriers to precipitation have been determined: one for formation of a nucleus, and one for particle growth. Based on the temperature dependence of growth rates, the effective activation energy for growth was found to range from 140 kJ/mol to 200 kJ/mol. Although the precise growth mechanism is unknown, this energy barrier is remarkably high, probably representing a coordinated multi-step attachment process. In comparison, the free energy of formation for the initial critical nuclei are relatively small, in the range of 40 kJ/mol to 70 kJ/mol. Note however, that the process of nucleation requires *growth* of a critical nucleus, so that the barrier to nucleation depends upon both values.

In the development of nucleation and growth theory, the barrier for molecular addition and subtraction was first explicitly considered as an activated process in the work of Turnbull and Fisher.[38] The total process of nucleation can then be represented schematically, as in Figure 10 (A). In this figure, the dashed grey curve represents the free energy of a cluster with n Fe atoms, which has a maximum at ΔG_c. Superimposed upon this curve is an oscillating function that represents the activation energy for adding or subtracting a molecule to the cluster. The barriers to molecular addition and subtraction are often assumed to be small, arising from processes such as diffusion, and these are often neglected when constructing diagrams to represent nucleation.

Our results lead to a conceptual revision of this free energy landscape, to one where the activation energy for molecular addition may exceed that of the nucleus itself (at least during the early stages of precipitation). This revision is represented schematically by Figure 10 (B). The classical nucleation theory still applies in this new picture and its influence on precipitation is still profound, since the nucleation process still ensures that precipitate growth only occurs on a small number of distinct particles. Furthermore, as supersaturation drops, ΔG_c rises dramatically and the system will soon returns to scenario shown in Figure 10 (A). However, this conceptual revision is important, because it indicates a situation where the detailed mechanism of molecular addition may be as important for determining which crystalline phase precipitates first as the details of interfacial energy and solubility.
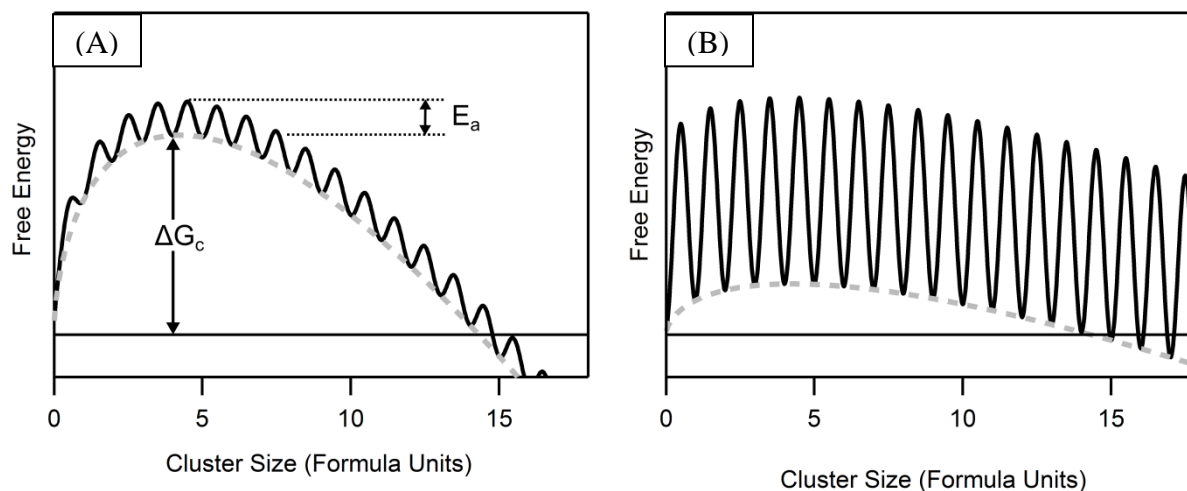

Figure 10: Schematic diagrams of the free energy landscape for nucleation for two cases with similar nucleation rates. Horizontal axis is the reaction coordinate. (A) Traditional nucleation model where the formation of a critical nucleus represents the primary barrier to nucleation. ΔG_{crit} is much larger than the free energy barrier to growth. (B) Growth limited nucleation. The energy barrier for addition and subtraction of a structural unit is much greater than the energy of the critical nucleus itself.

5.5.6 Limits of Classical Nucleation Theory

The FeOOH precipitation results presented here appear to be well described by classical nucleation theory. However, the very small nucleus sizes and very high growth barriers suggest that the limits of the classical nucleation regime are being approached. One can anticipate that for only moderately higher supersaturations (obtainable by adjusting pH), it may be possible to create situations where $n_c \leq 1$. When this occurs, clusters of any size are thermodynamically favored to grow and classical nucleation theory can no longer be used to predict nucleation rates. The behavior of systems where $n_c \leq 1$ have not be studied historically in much detail. Very recently, a paper by Vekilov has suggested that such systems are governed by spinodal decomposition.[39] However, the behavior of aqueous systems where $n_c \leq 1$ will be significantly more complex than traditional spinodal decomposition in solid-state systems. During precipitation from a dilute aqueous solution, structural changes in chemical bonding must occur and cluster-cluster aggregation may be a method for particle growth. Recent studies on the neutralization of ferric salts by base addition[40] have shown that the rapid formation of poorly crystalline precipitates is then followed by aggregation and phase transformation. On the basis of this study, it seems likely that such poorly controlled precipitation processes are occurring under conditions where $n_c \leq 1$. Indeed, this threshold may have been approached during the course of

this experiment. Attempts to characterize 800 mM $FeCl_3$ solution precipitation were unsuccessful because there was rapid formation of large scale structures that were too large for SAXS analysis. A rapid nucleation-free decomposition may explain this result.

5.5.7 The Monomer as a Cluster

The use of Equation 10 to define an interfacial tension for the monomer has proven to be a useful construct. It has provided a secondary method for predicting the interfacial energy of a cluster, showing how the interfacial energy depends upon pH.

The close agreement between interfacial tensions predicted by Equation 10 from monomer stability, and those determined from experiment for nucleation clusters is remarkable. In fact, it is better than might be expected, considering the approximations involved with defining interfacial area for small clusters, and the fact that a molecular cluster can undergo far more complicated interactions with the aqueous solution than a monomer. Equation 10 should not be expected to provide a perfect estimate for interfacial tension of the critical cluster, just as the interfacial tension of the critical cluster should not be expected to be identical with that of a bulk surface.

Nevertheless, the results suggest that Equation 10 can provide a useful tool for predicting how the interfacial tension of a cluster or particle depends upon solution chemistry when direct measurements of the interfacial tension are unavailable. This equation should be adaptable to many metal-oxyhydroxide systems; especially those where the addition and subtraction of a metal ion to the cluster is difficult, but where a variety of hydrolysis and acid-base reactions can occur relatively freely (so that the number of metal ions is a valid description of particle size).

The estimation of interfacial tension from solubility data can be made even easier in some special cases. For example, if the solid phase is in equilibrium with its solution, then the supersaturation term becomes zero, and Equation 10 can be simplified to the expression, $\gamma = kT \ln \frac{N_n}{N_0} / 4\pi r_n{}^2$. If large cluster formation is rare, than the solution is dominated by monomeric species, and N_1/N_0 is directly obtainable from the solubility of the solid phase. Thus, the interfacial tension for the monomer can be directly obtained from solubility data. This supports the work of Nielsen and Söhnel[5], and Mersmann[6], who uncovered relationships between solubility and interfacial tension through alternative derivations. This may have broad applications, because solubility data is typically much easier to obtain than interfacial energy measurements.

5.6 Conclusion

In this work, the nucleation and growth of β-FeOOH (akaganeite) nanoparticles as studied using *in situ* small angle x-ray scattering (SAXS). This method has allowed simultaneous determination of the particle growth rate and the overall precipitation rate. By classical nucleation and growth modeling, it is possible to determine nucleation rates and extract the interfacial energies for growing clusters.

For the nucleus interfacial tension, values are shown to be in the range of 0.05-0.12 J/m^2, with lower values at lower pH. These estimates are relatively robust against modeling errors. Although it has been generally understood that oxyhydroxide interfacial tensions must depend upon chemistry of the solution they are in contact with, this fact is often neglected. pH effects are

shown to be significant and non-neglectable, and this study represents the first quantitative measurements of iron oxyhydroxide interfacial tensions under the low pH conditions that are relevant to nanoparticle formation.

In order to model nucleation precisely and determine the size of the critical nucleus, it is important to have a reasonable description for the rate of cluster growth. This has been obtained here by directly measuring nanoparticle growth rates with SAXS. For detailed nucleation modeling, it was assumed that the process of molecular addition to a nucleus is analogous to the process of nanoparticle growth.

In this study, the apparent activation energy for particle growth is large (140 kJ/mol to 200 kJ/mol), but that the initial size of the critical nucleus is small, containing only 4 to 20 iron atoms, and the free energy of the critical nucleus (40-70 kJ/mol) only represents a small fraction of the total energy barrier for nucleation at the onset. The small size of the critical nucleus suggests that precipitation is occurring near the limits of classical nucleation, and this explains the difficulties in modeling iron oxyhydroxide precipitation. In such a system, relative growth rates may determine which iron oxyhydroxide phases first precipitate, since the kinetics of molecular addition to the nucleus may be more influential on nucleation rates than the interfacial energy or solubility of the precipitating phase.

Although the barrier provided by the critical nucleus is energetically small, its importance to the overall nucleation process should not be neglected. The presence of a nucleation barrier still ensures that precipitation occurs at some limited number of nucleation centers and that well defined particles are formed. If one attempts to increase nucleation rates by increasing the supersaturation further, the size of the nucleation barrier would become negligibly small (less than 1 or 2 Fe atoms). At this point, a dramatic shift in the precipitation mechanism may occur. With critical nucleus sizes on the order of 4-30 atoms, it appears that the systems studied here are poised at the limits of the classical nucleation regime.

One of the more powerful observations that has been identified, is that the cluster free energy construction can be extended to the molecular level for oxyhydroxide phases, and thus define an interfacial tension for monomeric metal ions dissolved in water. This construction allows one to predict the interfacial tension of a solid phase, based only upon knowledge of that solids solubility and aqueous speciation. This approach shows remarkable agreement with the interfacial tensions determined from nucleation rate modeling.

5.7 Supplementary

5.7.1 SAXS Background Subtraction
The unprocessed SAXS scattering pattern includes scattering due to the aqueous solution and the experimental apparatus. The particle scattering signal was isolated by subtracting an appropriate empty-field scattering pattern. For slowly precipitating samples, the first measured scattering pattern is essentially particle free, and was designated as the empty-field pattern. For rapidly precipitating samples where significant precipitation has already occurred before the first data acquisition, the empty-field pattern was obtained from a lower-temperature sample with identical initial chemistry and experimental configuration.

Because the synchrotron beam intensity can vary over time, the scattering intensity is normalized with respect to total transmitted beam intensity. The total transmitted beam intensity is determined by an ion chamber that is located along the x-ray flight path directly after the sample.

5.7.2 Calculation of Volume Precipitated by Invariant
Calculation of the Porod invariant, Q, for particle scattering is obtained by calculating the following

Equation 11

$$Q = \int_0^{q_{max}} I(q)q^2 \, dq$$

Expression corresponds to the area under the scattering curve in a Kratky plot, which shows $I(q)q^2$ *vs. q*. Assuming (1) that the precipitating phase contains a roughly constant and homogenous x-ray scattering density, and (2) that the particle volume remains a small fraction of the total suspension, than the value of Q will be proportional to the volume of particles precipitated.[22] At each timepoint, Q is calculated by numerical integration of the Kratky scattering curve using trapezoidal interpolation. SAXS can only obtain a finite range of scattering intensity, from q_{min} to q_{max}. Linear interpolation is used between $q = 0$ and q_{min}, by assuming that $I(0)0^2 = 0$. Example Kratky plots for 10 mM and 200 mM precipitation series at 80 degree are given below.
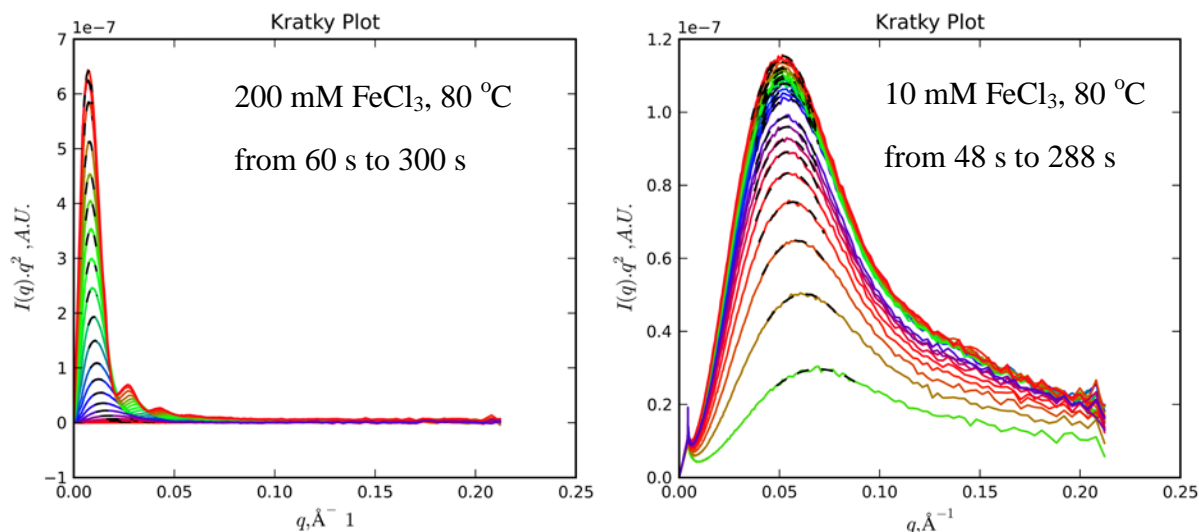
Figure 11:Example Kratky plots for two different experiments. Each curve corresponds to one timepoint. Curves are acquired at 10 second intervals. Black dashes indicate a fit, used to determine the q-value where $I(q)q^2$ shows a maximum value.

The volume of precipitated FeOOH is proportional to the area under these curves. Thus, it is crucial the experimental data contains all (or at least most) of the significant scattering. For each curve, a primary Kratky scattering peak can be observed. The location of this maximum in q-space is inversely related to particle size. During the course of experiment, as particles grow, this peak moves toward smaller q values. The invariant can only be accurately calculated if most of the Kratky peak is contained within the experimental observed scattering range. This is true for all of the data shown above, but for some experiments (i.e. 800 mM $FeCl_3$ precipitation, and some later stage 100 mM $FeCl_3$ precipitates) the structures formed were so large that the Kratky peak appeared below our measured q-range. In these cases, the dataset was discarded, and no attempt to calculate the invariant was made.

The invariant calculations must also be discarded after the onset of colloidal crystallization, since this leads to an increased scattering intensity at very low angles which fall below the observable q-range. The onset of colloidal crystallization is signaled by a decrease in the maximum of the primary Kratky scattering peak, and the appearance of one or more Bragg scattering peaks.

For very large particles, such as those formed from 200 mM $FeCl_3$, there is almost no relevant scattering intensity at high q-values relative to the background scattering by the aqueous suspension. Better estimates of Q can be obtained by trimming the dataset and only integrating over the lower q-range.

For very small particles though, such as those produced from 10 mM $FeCl_3$, there is significant scattering at high q-ranges, even above the maximum experimental scattering range. In these cases, the integration was performed up to the maximum experimentally obtained q-value, recognizing that the precipitate volume may be slightly underestimated.

For each experimental configuration, a scaling factor was determined, so that the invariant Q, could be interpreted as moles of akaganeite precipitated per unit volume. This scaling factor was calibrated by measuring suspensions of known Akaganeite particle concentrations, that were

prepared by reacting 5 mM $FeCl_3$ solutions to equilibrium at 80 °C (a condition at which near 100% precipitation is achieved under short timescales).

5.7.3 Calculation of Radius of Gyration by Guinier Method

The average particle radius of gyration, R_g, was obtained using the Guinier method, in which it can be shown that

Equation 12

$$R_g = -3 \frac{d\ln(I(q))}{d(q^2)}$$

This relationship is only valid over a limited region, at very low scattering angles. Example Guinier plots are shown below, again for 200 mM $FeCl_3$ and 10 mM $FeCl_3$ at 80 °C.
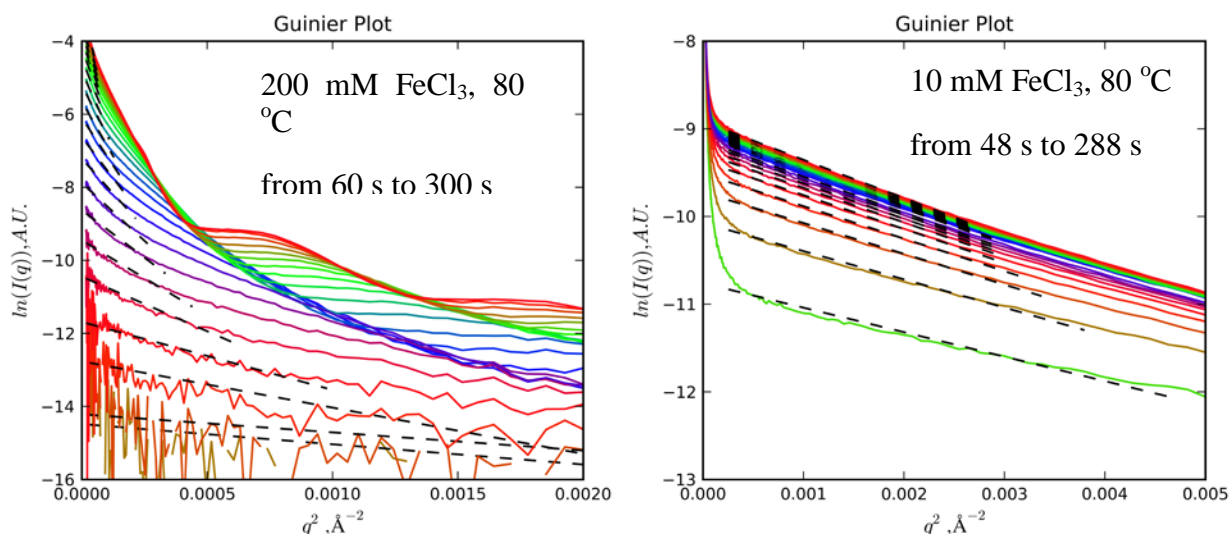
Each curve in the figures shown above corresponds to one time-point. Steeper slopes correspond to larger particles. Over time, the particles get larger and slopes become steeper. This is especially obvious in the 200 mM sample. The radius of gyration is obtained by linear regression to fit the slope in the lower q-range. Dashed black lines represent the Guinier fit, and extend over the range of q-values that fitting was performed for.

The Guinier relationship between slope and particle size is only valid for very low q-ranges. The Guinier region is commonly defined as $R_g \cdot q < 1.3$.[22] For this experiment, the slope is measured over the range $q_{min} < q < q_{kp}$, where q_{kp} is the location of the primary Kratky maximum. This q-range extends slightly outside of the commonly defined Guinier region, since $R_g \cdot q_{kp} \cong 1.9$. Although this wider region will contribute a small systematic error to the estimated radius of gyration of a few percent, the larger data range produces much better statistical reliability.

Even within the standard Guinier region, the slope is not perfectly linear. This non-ideal behavior is likely due to the presence of highly anisotropic particles and/or broad particle size distributions. The highly anisotropic particles formed in 400 mM did not have a clear linear

region, and it was not possible to determine the radius of gyration for these samples. The experiment performed at 800 mM could also not be characterized in this way.

In several experiments, such as the 10 mM sample shown above, a very sharp discontinuity in the Guinier slope can be observed. (In the 10 mM sample, this occurs just below 0.0002 Å^{-2}). This is most likely due to a small number of very large particles in the suspension, formed during sample preparation. In the case of the 10 mM sample, these particles appear to be a minor component of the overall system with a negligible volume fraction. Thus, the low-q range is trimmed from the dataset, so that the Guinier slope will be determined over a slightly smaller region, to measure the particle size of the main population separately from that of the few large particles.

However, in some of the initial 5, 10, and 20 mM samples, the population of large particles at the beginning of the experiment was significant and could not be neglected (This was confirmed with TEM). The larger particles were presumably generated by room-temperature nucleation and growth, when solutions were diluted several hours prior to thermal hydrolysis. These experiments were discarded and repeated with samples that were diluted less than 15 minutes prior to thermal growth.

5.7.4 Precipitation Curves and fits
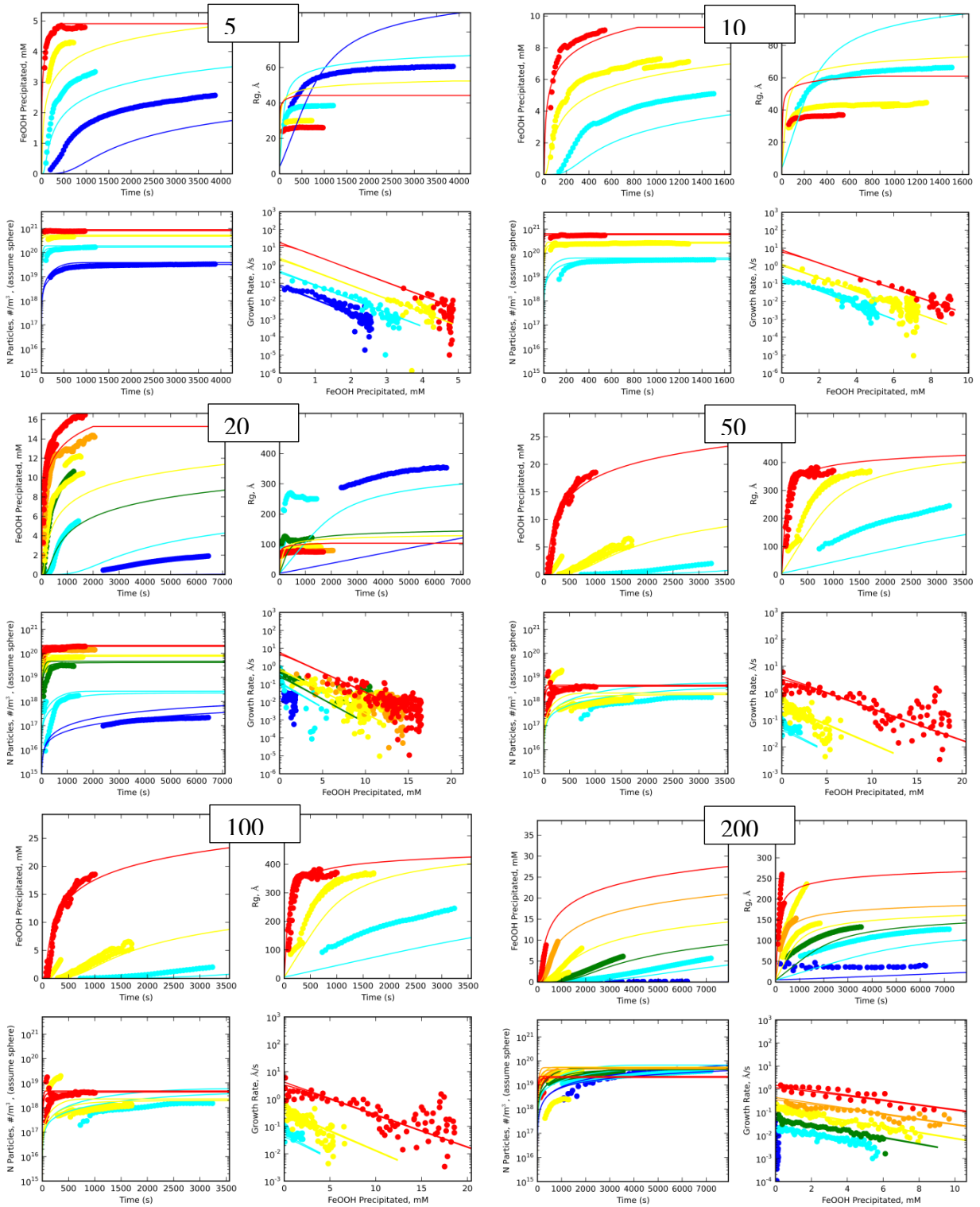
The figures above represent all experimental data sets that were used to calculate particle growth rates and perform nucleation and growth modeling. The colors represent temperature Red: 80 °C, Orange: 73 °C, Yellow : 67 °C, Green: 62 °C, Cyan: 57 °C, Blue: 47 °C. Circles represent experimental data points, while lines are fits obtained by nucleation and growth modeling.

The nucleation and growth fits were determined, such that the maximum apparent number of particles, N_{max}, is best reproduced. This does not necessarily produce the best fit for FeOOH precipitation profile or the radius of gyration profile, but the general characteristics of these curves are reproduced well.

In the plots that show number of particles vs. time, two fitting curves are plotted for each experiment. One curve corresponds to the actual number of particles produced in the experiment, while the second corresponds to the apparent number of particles produced in the experiment (this second curve has a slightly lower value). To estimate γ, the value of γ was found which best replicated the number of particles nucleated (N_{max}).

5.7.5 Geometric relationship between particle size, radius of gyration, and volume
Particles can be roughly approximated as ellipsoidal volumes. The radius of gyration for an ellipsoidal object of uniform density is given in terms of the semi-principle axes, r_1, r_2, and r_3 as:

Equation 13

$$R_g = \sqrt{(r_1^2 + r_2^2 + r_3^2)/5}$$

For these particles, a spheroidal shape is assumed, where $r_1 = r_2 = width/2$, and $r_3 = length/2$. The aspect ratio is defined as $AR = length/width$. Thus, one can calculate the radius of gyration from TEM images, by measuring particle length and width.

The volume of an ellipsoid with these semi-principle axes is given as:

Equation 14

$$V = \frac{4\pi}{3} r_1 r_2 r_3$$

For a given aspect ratio, it can be shown that

Equation 15

$$V = R_g{}^3 \frac{4\pi AR}{3} \left(\frac{2 + AR^2}{5}\right)^{-3/2}$$

Thus, to satisfy the equation $V = \alpha R_g{}^3$, one can obtain the identity

Equation 16

$$\alpha = \frac{4\pi AR}{3} \left(\frac{2 + AR^2}{5}\right)^{-3/2}$$

93

This relationship is necessary for estimating particle volume, because the SAXS Guinier technique only provides radius of gyration. This relationship was developed on the assumption of spheroidal particle shapes, but analogous expressions can be developed for rectangular prisms or other reasonable particle shapes. This will have a negligible impact on the relationship between volume and radius of gyration (<20% error), so long as the aspect ratio is accounted for.

5.7.6 Estimation of the preexponential factor.

The rate of change in the radius of gyration, v, is proportional to the rate at which the particle surface advances, and thus the frequency of attachment to a growing particle surface (in units of $m^{-2}s^{-1}$) can be is estimated in terms of the growth rate as:

Equation 17

$$f_1 = v \frac{N_A}{V_m} \sqrt{5/3}$$

Again, this formulation is only valid if the frequency of attachment is much greater than the frequency of detachment. This formulation also assumes that the unit of attachment corresponds to the addition of one molecular unit of FeOOH. (In practice, the surface advancement may acutally be controlled by addition of Fe-dimer species, or by addition of non-stoiciometric reactive species, but this will have a small impact on the overall model). The factor of $\sqrt{5/3}$ in Equation 17 is merely a geometric correction, relating the sphere's radius of gyration to its geometric radius. This geometric correction assumes a spherical particle surface area, and neglects particle shape effects. A critically sized nucleus has a surface area of $4\pi r_c^2$, and so the frequency of attachement to a given nucleus (in units of s^{-1}) is given as:

Equation 18

$$f_2 = 4\pi r_c^2 \cdot v \frac{N_A}{V_m} \sqrt{5/3}$$

The number of critically sized nuclei per unit volume of suspension is obtained from the Volmer-Weber distribution as:

Equation 19

$$\frac{N_n}{V} = \frac{N_{tot}}{V} \cdot \exp\left(-\frac{\Delta G_n}{kT}\right)$$

Thus, the total rate of nucleation (in units of $m^{-3}s^{-1}$) should be

Equation 20

$$I = 4\pi r_c^2 \cdot v \frac{N_A}{V_m} \sqrt{5/3} \cdot \frac{N_{tot}}{V} \cdot \exp\left(-\frac{\Delta G_n}{kT}\right)$$

This equation can be written in the more compact form of Equation 3, when we identify the preexponential term, A, according to Equation 8. The values for A that are obtained based on this derivation are within the expected range.

94

5.7.6 Notes on MINTEQ Chemical Speciation Calculations.

All aqueous speciation calculations are performed using Visual MINTEQ version 3.0, using the following species tableau:

Table 5: Thermodynamic parameters and chemical composition of aqueous species considered during solubility analysis.

Species	$\log_{10}(K)$ (at 25 °C)	ΔH_r (kJ/mol)	Cl^{-1}	Fe^{+3}	H^{+1}	H_2O
$FeOH^{+2}$	-2.02	25.1	0	1	-1	1
$Fe(OH)^{2+}$	-5.75	37.7	0	1	-2	2
$Fe(OH)_3$ (aq)	-15	75.3	0	1	-3	3
$Fe(OH)_4^-$	-22.7	154.8	0	1	-4	4
$Fe_2(OH)_2^{+4}$	-2.894	56.42	0	2	-2	2
$Fe_3(OH)_4^{+5}$	-6.288	65.24	0	3	-4	4
$FeCl^{+2}$	1.48	23	1	1	0	0
OH-	-13.997	55.81	0	0	-1	1

Activity is corrected using the Davies approach, with a *b* parameter of 0.3. For $FeCl_3$ solutions of 400 mM and higher, this may slightly exceed the intended ionic strength range of the Davies equation (1 M).

The equilibrium solution conditions are calculated iteratively, allowing 5000 iterations, and solids are not allowed to precipitate. The final pH is calculated by mass balance, and the ionic strength is not fixed (it is calculated from input). The initial saturation is plotted in Figure 4 in the main body of the paper, as a function of temperature and initial $FeCl_3$ concentration (C_o). This is obtained by MINTEQ calculation, where the input components are:

Equation 21

$$[Fe^{3+}] = C_o$$
$$[Cl^-] = 3C_o$$

The response of supersaturation to precipitation was also calculated. Starting with a concentration of $[FeCl_3] = C_o$, the effective solution concentrations for a solution in which C_{precip} moles/liter of β-FeOOH have been precipitated are given as follows:

Equation 22

$$[Fe^{3+}] = C_o - C_{precip}$$

$$[Cl^-] = 3C_o$$

$$[H^+] = 3C_{precip}$$

A series of MINTEQ calculations for every experimental temperature and starting concentration were performed. Plots of how saturation responds to the degree of reaction are shown below, for just two different initial temperatures. When the suspension reaches equilibrium, then $x = 1$ and $\sigma = 0$. As degree of reaction pass 1.0, the solution becomes under-saturated; this condition is not expected to be experimentally obtainable. In this calculation, no attempt has been made to account for how particle size and surface tension may influence solubility.
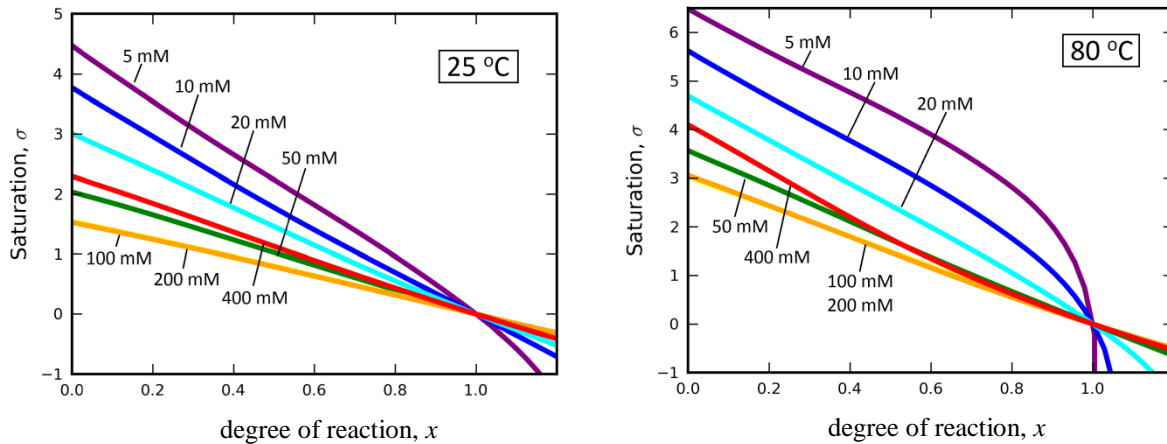
Figure 12: Response of solution saturation with respect to β-FeOOH, as precipitation proceeds. (When the solution reaches equilibrium with β-FeOOH , the degree of reaction equals 1.

5.7.7 Tables of Data

Table 6: This table summarizes each SAXS precipitation experiment that was performed, and the fitting results.

C_0	T	Experiment ID	Length (m)	N_{max}	t_{nuc}	Fitting range	Notes	γ	γ-low	γ-high	γ-max
mM	°C				s	s		J/m^2	J/m^2	J/m^2	J/m^2
5	47	005_47_3	3.87	$3.2 \cdot 10^{19}$	510	3910	-	0.1195	0.1027	0.1324	0.1682
5	57	005_57_2	1.33	$2.3 \cdot 10^{20}$	270	1250	-	0.1225	0.1019	0.1376	0.1750
		005_57_3	3.87	$1.6 \cdot 10^{20}$	210	1220	-	0.1237	0.1037	0.1386	0.1757
5	67	005_67_2	1.33	$3.4 \cdot 10^{20}$	130	940	-	0.1299	0.1071	0.1464	0.1921
		005_67_3	3.87	$4.6 \cdot 10^{20}$	110	730	-	0.1287	0.1054	0.1455	0.1916
		005_67_4	3.87	$3.9 \cdot 10^{20}$	90	430	-	0.1293	0.1064	0.1460	0.1919
5	73	005_73_2	1.33	-	-	-	prenuc	-	-	-	-
5	80	005_80_2	1.33	-	-	-	prenuc	-	-	-	-
		005_80_3	3.87	$7.7 \cdot 10^{20}$	20	980	-	0.1378	0.1113	0.1565	0.1901
10	57	010_57_3	3.87	$5.3 \cdot 10^{19}$	290		-	0.1156	-	0.1282	0.1607
10	67	010_67_2	1.33	$3.2 \cdot 10^{20}$	50	950	-	0.1185	0.0983	0.1333	0.1726
		010_67_3	3.87	$2.5 \cdot 10^{20}$	60	740	-	0.1194	0.0995	0.1340	0.1729
10	80	010_80_3	3.87	$5.5 \cdot 10^{20}$	40	550	-	0.1273	0.1043	0.1438	0.1808
20	47	020_47_3	3.87	$3.1 \cdot 10^{17}$	5330	6500		0.1027	0.0919	0.1115	0.1370
20	57	020_57_2	1.33	-	-	-	prenuc	-	-	-	-
		020_57_3	3.87	$2.0 \cdot 10^{18}$	800	1450		0.1094	0.0972	0.1191	0.1463
20	62	020_62_2	1.33	$4.0 \cdot 10^{19}$	430	180		0.1069	0.0921	0.1182	0.1476
20	67	020_67_2	1.33	$8.7 \cdot 10^{19}$	-	1560		0.1088	0.0927	0.1210	0.1511
		020_67_3	3.87	$6.9 \cdot 10^{19}$	210	1600		0.1094	0.0936	0.1215	0.1515
		020_67_4	3.87	$9.5 \cdot 10^{19}$	-	1700		0.1085	0.0924	0.1208	0.1510
20	73	020_73_1	3.36	$1.4 \cdot 10^{20}$	125	2060		0.1122	0.0950	0.1252	0.1563
20	80	020_80_1	3.36	$1.8 \cdot 10^{20}$	110	1700		0.1170	0.0986	0.1308	0.1621
		020_80_2	1.33	$1.9 \cdot 10^{20}$	70	920		0.1168	0.0984	0.1307	0.1620
		020_80_3	3.87	$1.4 \cdot 10^{20}$	80	600		0.1177	0.0997	0.1314	0.1625
50	57	050_57_3	3.87	$\sim 6 \cdot 10^{17}$	>1400	1600		0.0916	0.0823	0.0993	0.1206
50	67	050_67_3a	3.87	$3.0 \cdot 10^{18}$	500	1220		0.0970	0.0862	0.1059	0.1282
		050_67_3b	3.87	$3.7 \cdot 10^{18}$	530	1320		0.0966	0.0857	0.1055	0.1280
		050_67_4	3.87	$5.6 \cdot 10^{18}$	355	4400		0.0958	0.0847	0.1049	0.1276
50	80	050_80_3	3.87	$6.0 \cdot 10^{19}$	90	1100		0.1007	0.0867	0.1116	0.1361
100	57	100_57_3	3.87	$4.4 \cdot 10^{18}$	7000	3300		0.0779	0.0690	0.0852	0.1051
100	67	100_67_2	1.33	-	-	-	q-range	-	-	-	-
		100_67_3a	3.87	$1.6 \cdot 10^{18}$	1000	1500		0.0875	0.0782	0.0951	0.1152
		100_67_3b	3.87	$2.3 \cdot 10^{18}$	2400	1750		0.0869	0.0774	0.0946	0.1149
100	80	100_80_2	1.33	-	-	-	q-range	-	-	-	-
		100_80_3a	3.87	$4.0 \cdot 10^{18}$	-	450		0.0959	0.0851	0.1047	0.1257
		100_80_3b	3.87	$4.4 \cdot 10^{18}$	280	720		0.0957	0.0850	0.1046	0.1256
200	47	200_47_1	3.36	$4.0 \cdot 10^{19}$	-	6000		0.0821	0.0821	0.0821	0.0821
200	57	200_57_1	3.36	$5.0 \cdot 10^{19}$	5200	7300		0.0815	0.0815	0.0815	0.0815
200	62	200_62_1	3.36	$4.1 \cdot 10^{19}$	1740	3600		0.0821	0.0821	0.0821	0.0821
200	67	200_67_1	3.36	$4.8 \cdot 10^{19}$	1120	1875		0.0821	0.0709	0.0907	0.1133
		200_67_2	1.33	-	-	-	q-range	-	-	-	-
		200_67_3	3.87	$6.5 \cdot 10^{18}$	2300	1350		0.0815	0.0701	0.0902	0.1130
200	73	200_73_1	3.36	$4.7 \cdot 10^{19}$	520	850		0.0865	0.0748	0.0956	0.1186
200	80	200_80_1	3.36	$2.0 \cdot 10^{19}$	170	380		0.0935	0.0816	0.1028	0.1257
		200_80_3	3.87	$6.6 \cdot 10^{18}$	190	270		0.0956	0.0845	0.1046	0.1269
400	67	400_67_2	1.33	-	-	-	AR	-	-	-	-
400	80	400_80_2	1.33	-	-	-	AR	-	-	-	-
800	80	800_80_1	3.36	-	-	-	q-range	-	-	-	-

Meaning of Notes (continued on next page):

prenuc: the experiment was not used, because there was strong evidence for prenucleation: this includes the presence of a large-particle scattering signal in the first obtained SAXS patterns, and subsequent growth with a strong bimodal size distribution.

q-range: the experiment was not used, because the experimental q-range did not cover enough low-q scattering to properly characterize the large particle sizes produced in this experiment.

AR: the radius of gyration could not be accurately determined, because the particle aspect ratio was too large, and a linear Guinier region was not present within the visible q-range.

5.7.8 Derivation of the Work of Formation for a Particle

In this section, the derivation of the expression given earlier as Equation 4 is discussed. Equation 4 (i.e. $\Delta G_n = -nk_bT\sigma + 4\pi r_n^2\gamma$), is commonly referred to as the "free energy of particle formation", or sometimes the "work of particle formation." This formulation was originally developed by Gibbs, and is employed in most common nucleation and growth models. However, in most common derivations of ΔG_n, the possibility of surface adsorption is not explicitly considered. In the Gibbs surface construction, it is well established that surface adsorption causes a difference between surface (interfacial) tension, γ, and the surface (interfacial) excess free energy. In this derivation, surface adsorption will be explicitly allowed to occur, and it will be shown that Equation 4 still holds, and that, γ (the interfacial tension, according to the standard definitions for surface thermodynamics) is indeed the proper interfacial energy term to employ for determining ΔG_n.

We shall begin deriving this expression by considering the general precipitation of a solid phase, β, from a solution phase, α, and then show how this applies to the precipitation of β-FeOOH.

The physical quantity that ΔG_n describes is the change in the Gibbs free energy of the entire system, upon formation of a cluster of size n in a fixed location. We must specify that the cluster forms at a fixed location, otherwise we would be required to include a configurational entropy term, that accounts for the possibility that such a cluster may form at any location within the system, and which has a value of approximately $k\ln(N_n/N_{tot})$. As previously, N_n refers to the number of clusters with size n, and N_{tot} is the total number of molecules in the system.

The change in Gibbs free energy of the system upon formation of a particle at some fixed location is simply the difference between the initial free energy of the system prior to particle formation, G^i, and the final free energy of the system after particle formation G^f.

Equation 23

$$\Delta G = G^f - G^i$$

Note that embryonic clusters are smaller than the critical size, so that ΔG is positive, meaning that the existence of such a cluster at a particular fixed site will not be stable, and the final state cannot be considered an equilibrium state. However, due to the configurational entropy benefits of forming such clusters, there will be an equilibrium concentration of similar clusters throughout the system.

The initial state is represented schematically in Figure 13 A. It comprised solely of the homogenous phase α, and so we label its free energy as follows:

Equation 24

$$G^i = G^{\alpha,i}$$

The final state is more complex, with some parts of the system possessing the thermodynamic properties of the α phase, some parts possessing the thermodynamic properties of the β phase, and an interfacial region within which both of these phases may be significantly perturbed by their interactions with the other. For very small particles, we may assume that the entire β particle volume lies within the interfacial region. A crude diagram of this situation is shown in

Figure 13 B. In this figure, the dashed line designates a semi-arbitrary interfacial region, and outside of this region the system has the properties of the bulk α phase (although with a very slightly different composition than in the initial state).

The configuration inside the interfacial region may be complex and is not straightforward to describe, but the contents of this region can be represented thermodynamically using a variation of the Gibbs interface construction. We introduce a closed Gibbs dividing surface that is centered around the particle and lies inside the interfacial region. We suppose that the all of the volume outside of this dividing surface is homogenous and has the same average thermodynamic properties that the final bulk α phase has far away from the particle. We suppose that the volume inside the dividing surface is homogenous and has the average thermodynamic properties and stoichiometric composition of the ideal bulk β phase. This construction is shown in Figure 13 C. The total composition and thermodynamic content of the constructed reference system (Figure 13 C) and the actual system (Figure 13 B) must be the same. In order to make these systems thermodynamically equivalent, we introduce the *excess interfacial quantities*, which are designated with the superscript σ. The energy, entropy, free energy, and composition of the system can now be written as:

Equation 25

$$E^f = E^{\alpha,f} + E^{\beta,f} + E^\sigma$$

$$S^f = S^{\alpha,f} + S^{\beta,f} + S^\sigma$$

$$G^f = G^{\alpha,f} + G^{\beta,f} + G^\sigma$$

$$N_k^\sigma = N_k^f - \left(N_k^{\alpha,f} + N_k^{\beta,f} \right)$$

These equations serve as definitions for the excess interfacial quantities, and the excess interfacial quantities are assumed to be localized upon the Gibbs dividing surface, although they are actually distributed throughout the interfacial region.
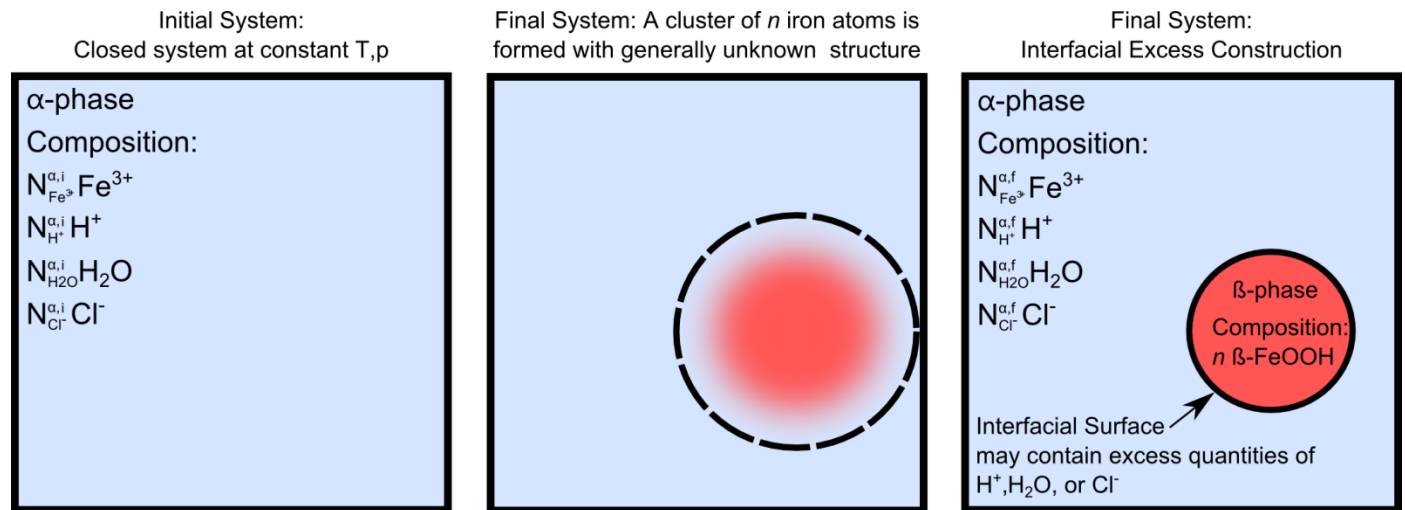

Figure 13: Schematic diagram of physical systems for determining the thermodynamics of a cluster

Returning to our original goal, we can now develop an expression for the change in free energy of the system upon creation of a particle. The free energy of the final system is $G^f = G^{\alpha,f} + G^{\beta,f} + G^{\sigma,f}$, and the free energy of the initial system is $G^i = G^{\alpha,i}$. Thus

Equation 26

$$\Delta G = G^{\alpha,f} + G^{\beta,f} + G^{\sigma,f} - G^{\alpha,i}$$

We now seek to find expressions for the Gibbs free energy of each system in terms of composition and chemical potentials, using the following definition for the Gibbs free energy of the system:

Equation 27

$$G = E - TS + pV$$

In terms of its natural variables (T, p, and $\{N_k\}$), the differential in Gibbs free energy of the α phase is thus

Equation 28

$$dG^{\alpha} = -S^{\alpha}dT + V^{\alpha}dp + \sum \mu_k^{\alpha} \, dN_k^{\alpha}$$

At constant temperature and pressure, this yields

Equation 29

$$dG^{\alpha} = \sum \mu_k^{\alpha} \, dN_k^{\alpha}$$

This can be integrated to yield the following expression for Gibbs free energy.

Equation 30

$$G^{\alpha} = \sum \mu_k^{\alpha} N_k^{\alpha}$$

Identical equations hold for the β phase, but the corresponding equations for the interface are slightly different. The free energy here must also include a term to reflect work that occurs due to changes in the interfacial area. The interfacial tension, γ, is defined as

Equation 31

$$\gamma = \left(\frac{\partial E}{\partial \mathcal{A}}\right)_{S,V,n_i} = \left(\frac{\partial G}{\partial \mathcal{A}}\right)_{p,T,n_i}$$

Here, $\mathcal{A}$ represents the interfacial area of the particle. Thus, we write an expression for the excess Gibbs free energy of the interface in the differential form as:

Equation 32

$$dG^{\sigma} = -S^{\sigma}dT + V^{\sigma}dp + \sum \mu_k^{\sigma} \, dN_k^{\sigma} + \gamma d\mathcal{A}$$

101

This expression can be simplified by assuming constant temperature and pressure:

Equation 33

$$dG^\sigma = \sum \mu_k^\sigma \, dN_k^\sigma + \gamma d\mathcal{A}$$

Or, alternatively:

Equation 34

$$G^\sigma = \sum \mu_k^\sigma \, N_k^\sigma + \gamma\mathcal{A}$$

The expression for $\Delta G = G^{\alpha,f} + G^{\beta,f} + G^{\sigma,f} - G^{\alpha,i}$ can now be expanded in terms of chemical potentials as follows:
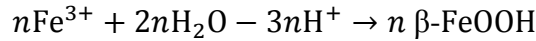
Equation 35

$$G^{\alpha,f} = \sum \mu_k^{\alpha,f} \, N_k^{\alpha,f}, \quad G^{\beta,f} = \sum \mu_k^{\beta,f} \, N_k^{\beta,f}, \, G^{\alpha,i} = \sum \mu_k^{\alpha,i} \quad , G^{\sigma,f} = \sum \mu_k^{\sigma,f} \, N_k^{\sigma,f} + \mathcal{A}\gamma$$

$$\Delta G = \sum \mu_k^{\alpha,f} \, N_k^{\alpha,f} + \sum \mu_k^{\beta,f} \, N_k^{\beta,f} + \sum \mu_k^{\sigma,f} \, N_k^{\sigma,f} - \sum \mu_k^{\alpha,i} \, N_k^{\alpha,i} + \mathcal{A}\gamma$$

We are now in a good position to consider the specific case of precipitating of an FeOOH cluster of size n, according to the following reaction

Equation 36

$$n\text{Fe}^{3+} + 2n\text{H}_2\text{O} - 3n\text{H}^+ \rightarrow n \, \beta\text{-FeOOH}$$

This occurs from an aqueous solution of H_2O, and containing the dissolved species H^+, Fe^{3+}, and Cl^-. (In fact, this suspension may include other species, such as OH^- or $FeOH^{2+}$ but these need not be considered, since they can be formed from the four primary components, and since they are assumed to be in thermodynamic equilibrium with the other four components, their concentrations cannot be varied independently). Upon precipitating a cluster with n Fe atoms, the ideal cluster stoichiometry will be as follows:

Equation 37

$$N_{Fe^{3+}}^{\beta,f} = n$$

$$N_{H_2O}^{\beta,f} = 2n$$

$$N_{H^+}^{\beta,f} = -3n$$

Because the total system is closed, for any chemical species, the following constraints apply:

Equation 38

$$N_k^f = N_k^{\alpha,f} + N_k^{\beta,f} + N_k^{\sigma,f} \quad = \quad N_k^i = N_k^{\alpha,i}$$

Following a standard Gibbs construction approach, the volume of the β-phase particle is defined such that there is no excess interfacial quantity of Fe, i.e. $N_{Fe^{3+}}^{\sigma,f} = 0$. This is done by defining the Gibbs dividing surface as the boundary of a spherical volume, with radius of $(3nV_m/4\pi N_a)^{1/3}$. This approach is necessary, because the true size the particle and its thermodynamic properties are generally unknown. However, this approach does have a limitation, in that the placement of the interface may not correspond precisely to the "surface of tension", and as a consequence the interfacial energy may depend upon radius of curvature. For a cluster containing n Fe atoms, the following set of expressions now holds for the composition of the interface and the final α phase:

Equation 39

$$N_{Fe^{3+}}^{\alpha,f} - N_{Fe^{3+}}^{\alpha,i} = n$$

$$N_{H_2O}^{\alpha,f} + N_{H_2O}^{\sigma} - N_{H_2O}^{\alpha,i} = 2n$$

$$N_{H^+}^{\alpha,f} + N_{H^+}^{\sigma} - N_{H^+}^{\alpha,i} = 3n$$

$$N_{Cl^-}^{\alpha,f} + N_{Cl^-}^{\sigma} - N_{Cl^-}^{\alpha,i} = 0$$

There are also constraints on the chemical potentials for each phase. In this study, the solution phase is assumed to be so large relative to the (first) particles formed, that formation of a particle only produces infinitesimally small changes in the solution's bulk composition, so that chemical potential can be assumed to remain constant. Thus $\mu_k^{\alpha,f} = \mu_k^{\alpha,i} = \mu_k^{\alpha}$. Furthermore, because the solution phase and the interface can freely exchange chemical species, it is also true that $\mu_k^{\sigma,f} = \mu_k^{\alpha,f} = \mu_k^{\alpha}$. This is not true for the reference β phase, which is defined to have a fixed composition of n FeOOH. This imaginary constraint means that the β phase need not be in chemical equilibrium with that of the surrounding solution, and its chemical potential is assumed to be identical with that of bulk β-FeOOH, which has chemical potentials μ_k^{β}. Any deviations of the real particle from this ideal stoichiometry are accounted for as surface adsorption phenomena. Accounting for the constraints on chemical potentials, the general expression for the reaction can now be written as:

Equation 40

$$\Delta G = \sum \mu_k^{\alpha} (N_k^{\alpha,f} + N_k^{\sigma,f} - N_k^{\alpha,i}) + \sum \mu_k^{\beta} N_k^{\beta,f} + \mathcal{A}\gamma$$

For the specific case of FeOOH precipitation, for a particle of size n, this becomes:

Equation 41

$$\Delta G_n = n(-\mu_{Fe^{3+}}^{\alpha} - 2\mu_{H_2O}^{\alpha} + 3\mu_{H^+}^{\alpha} + 0\mu_{Cl^-}^{\alpha}) + \left(\mu_{Fe^{3+}}^{\beta} + 2\mu_{H_2O}^{\beta} - 3\mu_{H^+}^{\beta} \right) + \mathcal{A}\gamma$$

The chemical potential for the α phase can alternatively be written in terms of activity as:

Equation 42

$$\mu_k^{\alpha} = \mu_k^{0,\alpha} + k_b T \ln(\{k\})$$

103

In the specific case of an FeOOH particle, the free energy of particle formation can this be written in terms of the standard chemical potentials of the components, and their chemical activities.

Equation 43

$$\Delta G_n = n\left(\mu_{Fe^{3+}}^{\beta} - \mu_{Fe^{3+}}^{0,\alpha} + 2\mu_{H_2O}^{\beta} - 2\mu_{H_2O}^{0,\alpha} - 3\mu_{H^+}^{\beta} + 3\mu_{H^+}^{0,\alpha} \right) + k_b T \ln\left(\frac{\{H^+\}^3}{\{Fe^{3+}\}\{H_2O\}^2} \right) + \mathcal{A}\gamma$$

This expression can be written more simply, by introducing the solubility product for the dissolution reaction, defined here as $K_s = \exp\left(\mu_{Fe^{3+}}^{\beta} - \mu_{Fe^{3+}}^{0,\alpha} + 2\mu_{H_2O}^{\beta} - 2\mu_{H_2O}^{0,\alpha} - 3\mu_{H^+}^{\beta} + 3\mu_{H^+}^{0,\alpha} \right)$, by recognizing that $\{H_2O\} \cong 1$.

Equation 44

$$\Delta G_n = -nk_b T \ln\left(\frac{\{Fe^{3+}\}}{\{H^+\}^3 K_s} \right) + \mathcal{A}\gamma$$

After applying the definition for the saturation parameter, $\sigma = \ln\left(\frac{\{Fe^{3+}\}}{\{H^+\}^3 K_s} \right)$, and the basic form of Equation 4 is regained.

$$\Delta G_n = -nk_b T \sigma + \mathcal{A}\gamma$$

This analysis confirms that the interfacial tension is the appropriate thermodynamic parameter for determining the free energy of formation for an embryo, even when the cluster can be non-stoichiometric (i.e., interfacial adsorption can occur). The name "interfacial tension" is the historically accepted name for the thermodynamic parameter, $\gamma = \left(\frac{\partial G}{\partial \mathcal{A}} \right)_{p,T,n_i}$. This name may not seem fully appropriate here, since tension implies a mechanical force, while this derivation is based solely upon chemical thermodynamics and the tension with respect to perturbations in the cluster geometry have not been considered. Thus, it may seem preferable to refer to γ as an excess interfacial energy, but this should be avoided. The excess interfacial free energy, written in this paper as G^σ, is also a well-defined thermodynamic property with historical usage in surface science. As shown in Equation 34 (which is a form of the Gibbs adsorption equation), the excess interfacial free energy is not identical to γ, in fact they must differ whenever interfacial adsorption occurs.

5.7.9 Considering radius dependent interfacial tensions

The derivation above is not entirely general, in that we have merely defined the interfacial tension as follows:

Equation 45

$$\gamma = \left(\frac{\partial E}{\partial \mathcal{A}} \right)_{S,V,n_i} = \left(\frac{\partial G}{\partial \mathcal{A}} \right)_{p,T,n_i}$$

This definition is somewhat insufficient, because the interfacial tension in general is also dependent upon the particle size (interfacial curvature). In many cases, it is possible to assume

that γ is independent of curvature, but this is only strictly valid when the placement of the interface is coincident with the so called "surface of tension." In all of the work shown here, the location of the interface has been selected to produce zero excess Fe in the cluster, and there is no guarantee that this coincides with the surface of tension. Thus, we must consider the possibility that γ depends upon interfacial curvature. One option for doing this, is to propose a more complete definition to γ as follows:

Equation 46

$$\gamma = \left(\frac{\partial E}{\partial \mathcal{A}}\right)_{S,V,n_i,\kappa} = \left(\frac{\partial G}{\partial \mathcal{A}}\right)_{p,T,n_i,\kappa}$$

In this definition for γ, the derivative is taken at constant curvature, κ. This definition is somewhat troublesome, since it is impossible (using a single particle) to adjust that particle's interfacial area without also changing the particle curvature. This definition of interfacial tension can only be reasonably applied to ensembles of particles. Using this definition, most of the previous results are still valid, including Equation 34, which relates γ to the excess interfacial free energy. However, this equation can be rewritten, to show explicitly that γ is now a function of the particle's radius of curvature:

Equation 47

$$G^\sigma = \sum \mu_k^\sigma N_k^\sigma + \gamma(r)\mathcal{A}$$

Despite these changes, Equation 4 is still a valid expression for the free energy of cluster formation. Again, this equation can be rewritten to more explicitly show the dependance of the interfacial tension on particle radius.

Equation 48

$$\Delta G_n = -\frac{4\pi\, r_n{}^3}{3}\frac{RT\sigma}{V_m} + 4\pi r_n{}^2\,\gamma(r)$$

Certain other conclusions of classical nucleation theory, such as Equation 6, must be reevaluated when the interfacial tension is not a constant. The expressions in Equation 6 (which contained expressions for the critical nucleus radius and critical cluster size), can be derived from Equation 4 (or Equation 48), by identifying the point where $\frac{d\Delta G_n}{dr} = 0$. When the interfacial tension is independent of curvature, this is true when $\frac{RT\sigma}{V_m} = \frac{2\gamma}{r}$. However, when the interfacial tension also depends upon radius dependent interfacial tension, the critical point occurs when:

Equation 49

$$\frac{RT\sigma}{V_m} = \frac{2\gamma}{r} + \frac{\partial\gamma}{\partial r}$$

Thus, we can solve for the critical radius as:

Equation 50

$$r_c = \frac{V_m}{RT\sigma}\left(\frac{2\gamma}{r} + \frac{\partial\gamma}{\partial r}\right)$$

It is possible to assume a simple functional form for γ, and then consider how this functional form would modify the basic equations of classical nucleation theory. One such functional form would be the Tolman expression, $(r) = \gamma_\infty(1 - \frac{2\delta}{r})$, where δ is the Tolman length. Other functional forms have also been identified for nanoparticle surface energies, on the basis of high-pressure studies. However, the precise functional form for γ is unknown, and this for the purposes of this study it is unnecessary.

The experimental results show a very close agreement between the interfacial energy of monomeric species (based on tabulated thermodynamic data), and the interfacial energy of the critical nucleus, within a few percent. The disagreement between these two measurements can be taken as an indicator for the magnitude of $\partial\gamma/\partial r$. The small disagreement suggests that $\partial\gamma/\partial r$ is significantly less than $2\gamma/r$, and the classical nucleation theory can be applied without correction.

5.6 Acknowledgements

5.9 Works Cited

1. Melia, T.P. Crystal Nucleation from Aqueous Solution. *Journal of Applied Chemistry* **1965**, *15*, 345-357.
2. Christian, J.W. *The Theory of Transformations in Metals and Alloys, 3rd Edition*; Pergamon: New York, 2002; pp 422-461.
3. Sugimoto, T. Underlying Mechanisms in Size Control of Uniform Nanoparticles. *J. Colloid Interface Sci.* **2007**, *309*, 106–118.
4. Mersmann, A. Crystallization and Precipitation. *Chem. Eng. Process.* **1999,** *38*, 345-353.
5. Nielsen, A.E.; Söhnel, O. Interfacial Tensions Electrolyte Crystal-Aqueous Solution, From Nucleation Data. *J. Cryst. Growth*, **1971**, *11*, 233-242.
6. Mersmann, A. Calculation of Interfacial Tensions. *J. Cryst. Growth* **1990**, *102*, 841-847.
7. Baes, C.G., Mesmer, R.E., *The Hydrolysis of Cations*; John Wiley & Sons: New York, 1976.
8. Cornell, R.M; Schwertmann, U. *The Iron Oxides: Structure, Properties, Reactions, Occurrences and Uses, 2nd Edition*; Wiley-VCH: Weinheim, 2003.
9. Navrotsky, A. *et al.* Size-Driven Structural and Thermodynamic Complexity in Iron Oxides. *Science* **2008**, *319*, 1635-1638.
10. Baumgartner, J.; Dey, A.; Bomans, P.H.H.; Coadou, C.L.; Fratzl, P.; Sommerdijk, N.A.J.M/.; Faivre, D. Nucleation and Growth of Magnetite from Solution. *Nat. Mater.* **2013**,*12*, 310-314.
11. Li, D.; Nielsen, M.H.; Lee, J.R.I.; Frandsen, C.; Banfield, J.F.; De Yoreo, J.J. Direction-Specific Interactions Control Crystal Growth by Oriented Attachment. *Science* **2012**, *25*, 1014-1018.
12. Jolivet, J.P., *Metal Oxide Chemistry and Synthesis*. John Wiley & Sons: West Sussex, 2000; pp. 25-137; Translated by E. Bescher.
13. Mazeina, L.; Deore, S.; Navrotsky, A. Energetics of Bulk and Nano-Akaganeite, β-FeOOH: Enthalpy of Formation, Surface Enthalpy, and Enthalpy of Water Adsorption. *Chem. Mater.* **2006**, *18*, 1830-1838.
14. Fang, X.; Li, Y.; Chen, C.; Kuang, Q.; Gao, X.; Xie, Z.; Xie, S.; Huang, R.; Zheng, L.; pH-Induced Simultaneous Synthesis and Self-Assembly of 3D Layered β-FeOOH Nanorods. *Langmuir* **2010**, *26*, 2745–2750.
15. Sugimoto, T.; Muramatsu, A. Formation Mechanism of Monodispersed a-Fe_2O_3 Particles in Dilute $FeCl_3$ Solutions. *J. Colloid Interface Sci.* **1996**, *184*, 626-638.
16. Almeida, T.P.; Fay, M.W.; Zhu, Y.; Brown, P. D. Hydrothermal Growth Mechanism of α-Fe_2O_3 Nanorods Derived by Near In Situ Analysis. *Nanoscale* **2010**, *2*, 2390-2399.
17. Ceus, J. W. E.; Tacobus, J. M. *Chem. Abstr.* **1973**, *78*, 32167.
18. Holm, N.G.; Dowler, M.J.; Wadsten, T.; Arrhenius, G., β-FeOOH·Cl_n (Akaganeite) and $Fe_{1-x}O$ (Wustite) in Hot Brine from the Atlantis II Deep (Red Sea) and the Uptake of Amino Acids by Synthetic β-FeOOH·Cl_n. *Geochim. Cosmochim. Acta* **1983**, *47*, 1465-1470.
19. Atkinson, R.J.; Posner, A.M.; Quirk, J.P. Crystal Nucleation and Growth in Hydrolyzing Iron(III) Chloride Solutions. *Clays Clay Miner.* **1977**, *25*, 49-56.
20. Yue, J., Jiang, X., Yu, A., Experimental and Theoretical Study on the β–FeOOH Nanorods: Growth and Conversion. *J. Nanopart. Res.* **2011**, *13*, 3961-3974.

21. Porod, G. In *Small Angle X-Ray Scattering*; Glatter, O., Kratky, O., Eds.; Academic Press: London, 1982; pp. 18-59.
22. Feigin, L.A.; Svergun, D.I.; Taylor, G.W., *Structure Analysis by Small-Angle X-Ray and Neutron Scattering*; Plenum Press: New York and London, 1987; pp. 65-72.
23. Jiang, J. Q.; Graham, N. J. D. Observations of the Comparative Hydrolysis/Precipitation Behaviour of Polyferric Sulphate and Ferric Sulphate. *Water Res.* **1998**, *32*, 930-935.
24. Ilavsky, J.; Jemian, P. R. Irena: Tool Suite for Modeling and Analysis of Small-Angle Scattering. *J. Appl. Crystallogr.* **2009**, *42*, 347-353.
25. Fouilloux, S.; *et al*. SAXS Exploration of the Synthesis of Ultra Monodisperse Silica Nanoparticles and Quantitative Nucleation Growth Modeling. *Journal of Colloid and Interface Science* **2010**, *346*, 79–86.
26. Green, D.L. *et al.* Size, Volume Fraction, and Nucleation of Stober Silica Nanoparticles. *J. Colloid Interface Sci.* **2003**, *266*, 346–358.
27. Abecassis, B.; Testard, F.; Spalla, O.; Barboux, P. Probing in situ the Nucleation and Growth of Gold Nanoparticles by Small-Angle X-ray Scattering **2007**, *7*, 1723-1727.
28. Polte, J., *et al*. Nucleation and Growth of Gold Nanoparticles Studied via in situ Small Angle X-ray Scattering at Millisecond Time Resolution, *ACS Nano*, **2010**, *4*, 1076-1082.
29. Viswanatha, R.; *et al*. Growth of Semiconducting Nanocrystals of CdS and ZnS, *Journal of Nanoscience and Nanotechnology*, **2007**, *7*, 1726-1729.
30. Ford, I.J. Nucleation Theorems, the Statistical Mechanics of Molecular Clusters, and a Revision of Classical Nucleation Theory. *Physical Review E,* **1997**, *56*, 5615-5629.
31. Liu, X.; Millero, F.J. The Solubility of Iron Hydroxide in Sodium Chloride Solutions. *Geochimica et Cosmochimica Acta*, **1999**, *63*, 3487–3497.
32. Martell, A. E.; Smith, R. M.; Motekaitis., R. J. NIST critically selected stability constants of metal complexes database. *NIST standard reference database 46.6.0.* 2001.
33. Schwertmann, U. Solubility and Dissolution of Iron Oxides Plant and Soil, **1991**, *130*, 1-25.
34. Stumm, W.; Morgan, J.J., *Aquatic Chemistry Chemical Equilibrium and Rates in Natural Waters 3rd Edition*; John Wiley and Sons: New York, 1996.
35. Grosse, A.A.V., The Relationship Between Surface Tension and Energy of Liquid Metals and Their Heat of Vaporization at the Melting Point. *Journal of Inorganic and Nuclear Chemistry* **1964**, *26*, 1349-1361.
36. Casey, W.H.; Swaddle, T.W. Why Small? The Use of Small Inorganic Clusters to Understand Mineral Surface and Dissolution Reactions in Geochemistry. *Reviews of Geophysics*, **2003**, *41*, 1008.
37. Casey, W.H.; Rustad, J.R., Reaction Dynamics, Molecular Clusters, and Aqueous Geochemistry. *Annual Review of Earth and Planetary Sciences*, **2007**, *35*, 21–46.
38. Turnbull, D.; Fisher, J.C. Rate of Nucleation in Condensed Systems. *Journal of Chemical Physics* **1949**, *17*, 71.
39. Vekilov, P.G. Nucleation, *Cryst Growth Des.* 10 (2010), 5007–5019.
40. Zhu, M.; Legg, B.A.; Zhang, H.; Gilbert, B.; Ren, T.; Banfield, J.F.; Waychunas, G.A. Early Stage Formation of Iron Oxyhydroxides During Neutralization of Simulated Acid Mine Drainage Solutions. *Environmental Science and Technology.* **2012**, *46*, 8140-8147.